University of Reading

Department of Meteorology

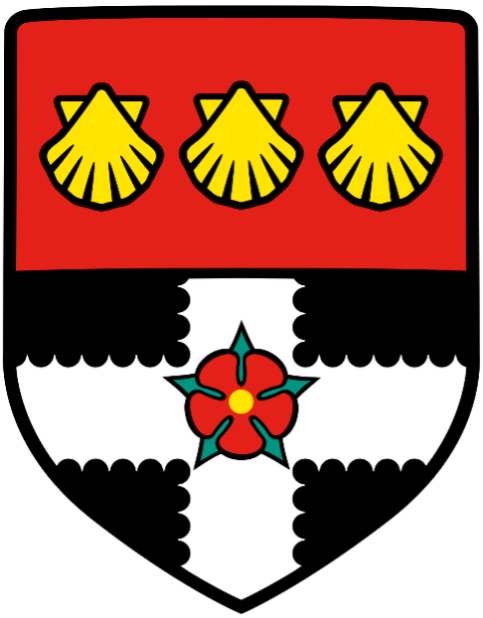

Evaluating Memory Effects in Convective Parameterization Schemes

Arundhati Kalyan

Supervisors: Prof. Robert Plant, Dr. Todd Jones, and Dr. Chimene Daleu

A dissertation submitted in partial fulfilment of the requirement for the degree of Master of Science (MSc) in Atmosphere, Ocean and Climate

August 2021

Acknowledgements

I would like to sincerely thank my supervisors Professor Robert Plant, Dr. Todd Jones and Dr. Chimene Daleu for their constant encouragement, support, and guidance during the three months of my dissertation project. I would also like to thank my academic tutor Dr. Hilary Weller for all the support she gave me throughout the MSc programme. I am also very grateful to the dissertation module convener Dr. David Brayshaw and the MSc programme director Dr. Tom Frame for their patience and consideration over the past few months. None of this would have been possible without the help and understanding of all these people.

Finally, I want to thank my family for encouraging me to keep going especially on all the days I felt like giving up. Thank you for believing in me and for making this happen.

Abstract

Idealized simulations of the diurnal cycle of tropical convection over land are performed with the Met Office Unified Model (UM) using two different parameterization schemes: the newly developed CoMorph scheme and the current 6A convection scheme. Identical simulations are performed using the Met Office NERC Cloud Model (MONC) and serve as a proxy for the "true" convective behavior. Convective and memory properties of the diurnal cycles simulated by each model and scheme are examined and compared. Memory of past convection is quantified using a memory function, which is evaluated on the basis of the conditional probability of finding rain over a given area and at a given time, given the probability of rain occurring over the same area at a previous time—after removing any effects of random chance. MONC simulations show three phases of memory: a positive first phase indicating the persistence of developing convection, a negative second phase indicating the suppression of convection, and a positive third phase corresponding to a secondary enhancement of convection. CoMorph simulations of ten-day duration show considerable day-to-day variability and long-term memory over grey-zone scales (4–10 km), indicating difficulties encountered by the scheme in representing convection at these spatial scales. At a range of spatial scales (4–50 km), CoMorph shows a significant improvement over the 6A scheme in producing a realistic diurnal cycle of precipitation and in capturing memory effects associated with the different phases of convection. The 6A scheme shows negligible memory at all times, while the CoMorph scheme is able to represent the first and second phases of memory associated with the development and suppression of convection respectively. However, CoMorph generates excess memory associated with the first phase, delays the start of the second phase, and extends the duration of both phases relative to MONC. CoMorph was also found unable to accurately simulate the diurnal cycles of mass flux and cloud fraction, and to resolve convectively generated small-scale thermodynamic fluctuations in the lower troposphere. These issues could be partly responsible for the biases in memory properties within CoMorph. Modifying select parameters within CoMorph produced some improvements in the behaviour of the precipitation cycle and reduced biases in the memory, but did not result in significant improvements in simulated convective properties.

Contents

List of Figures

1. Scientific Background

"If you wish to make an apple pie from scratch, you must first invent the universe."
— Carl Sagan

In this first section of the report, we present in detail the scientific ideas essential to our study of memory effects in convective parameterization schemes. Section 1.1 discusses various aspects of convective parameterization adopted in weather and climate models, Section 1.2 introduces the concept of "convective memory" which forms the basis of our study, and Section 1.3 describes the diurnal cycle of convection which we choose as the convective test case for our study. Relevant literature surrounding each of these topics is reviewed and summarized.

1.1 Convective Parameterization

Our study involves assessing the efficacy of convective parameterization schemes in simulating convective and cloud behaviour. To that end, we must first establish the theoretical framework of convective parameterization, and that is what this section endeavours to do. Section 1.1.1 explains the need to parameterize convection, Section 1.1.2 discusses the assumptions and limitations of traditional parameterization schemes, and Section 1.1.3 summarizes recent efforts to improve the accuracy of parameterizations.

1.1.1 Introduction

Convective processes, cloud formation, and precipitation typically occur on spatial scales of 10 m–1 km. However, most global weather (numerical weather prediction or NWP) and climate (global climate model or GCM) models have grid box sizes of much larger scales on the order of 10 km or greater. It would therefore be much more computationally expensive to resolve or evaluate convection explicitly in numerical models of the atmosphere. This issue has given rise to the need for the parameterization of convection in these models. Convective parameterization is the process of representing convection approximately using known model variables (such as temperature and moisture) that are resolved at the grid-scale, and it is carried out by convective parameterization "schemes" employed within weather and climate models. In general, convective parameterization schemes aim to represent the collective average behaviour of convection and clouds in each grid box rather than account for individual cloud evolution (Arakawa, 2004).

One of the first such parameterization schemes was put forward by Arakawa and Schubert (1974). Their theory assumes an ensemble of clouds covering a small fraction of the total grid

cell area, with further sub-ensembles for different cloud types. They divide the atmosphere into the cloud layer, which lies between the cloud base and the cloud top, and the mixed boundary layer beneath the cloud base, from where convective ascent occurs. At each model time step, convective activity and the cloud ensemble behaviour are determined by the large-scale environmental "forcing", which is composed predominantly of surface fluxes and atmospheric radiative cooling. These large-scale processes act to warm the atmosphere from below or cool it from above, thereby generating atmospheric instability and the vertical motions (updrafts) giving rise to convection. Cloudy updrafts increase in size through the process of entrainment which involves the mixing and exchange of surrounding environmental air. Once formed, the cloud ensemble can interact with and modify the large-scale thermodynamic profile of the atmosphere through the process of detrainment, which is the opposite of entrainment and involves the movement of air out of the cloud and into the environment.

In order to represent the processes described above, Arakawa and Schubert (1974) base their scheme on the "mass-flux" formulation of convection. Mass flux refers to the vertical transport of air induced during convective activity and is given by:

$$M = \rho \sigma w \tag{1}$$

where ρ is the density of air, σ is the fractional grid box area covered by ascending air masses, and w is the vertical velocity. M, the mass flux, has units of kg m^{-2} s^{-1} and represents the rate of flow of mass per unit area of the surface (Arakawa and Schubert, 1974, *their* Equation 2). The mass-flux parameterization framework assumes the existence of sub-grid-scale columns of vertical transport or fluxes of heat and moisture which remain largely independent of their surrounding environment, interacting only through the processes of entrainment and detrainment (Plant and Yano, 2016). Hence, their scheme seeks to determine, at each model time step and within each grid cell, the vertical profile and distribution of mass flux within the cloud ensemble as well as the behaviour of large-scale thermodynamic fields both within convective updrafts/downdrafts and in the environment.

The Arakawa-Schubert scheme (1974) has provided a valuable theoretical foundation for subsequent convective parameterizations and cloud modelling studies over the past several decades. Other notable examples of convection schemes which continue to be used are those developed by Gregory and Rowntree (1990), Kain and Fritsch (1990), Emanuel (1991), Donner (1993), and Zhang and McFarlane (1995). While most present-day schemes are based on the mass-flux framework, other types of schemes have also been proposed and found to be reliable (Arakawa, 2004). For instance, Kuo (1974) originated a class of schemes that make use of the principle

of water vapour conservation and diagnose convective activity on the basis of large-scale moisture convergence. Betts (1986) initiated another scheme type which relies on the concept of convective adjustment and forces the large-scale vertical temperature and moisture profiles to approach their observed behaviour in convective regions.

In addition to the physical formulation of convection employed, individual parameterization schemes differ in their choice of variables used to represent convection as well as in the specific constraints or "closure" conditions imposed on the convective system (Plant and Yano, 2016). Despite their differences, however, a few foundational assumptions tend to be shared by most convective parameterization schemes. These will be briefly discussed in Section 1.1.2 below.

1.1.2 Assumptions and Limitations

Out of the several assumptions and/or approximations a parameterization scheme must make, two in particular are shared by most traditional convection schemes and are relevant to our study of memory effects: the quasi-equilibrium assumption and the diagnostic assumption.

The quasi-equilibrium (QE) hypothesis, which was first introduced and implemented by Arakawa and Schubert (1974) in their scheme, assumes that convective processes are in statistical equilibrium with the large-scale forcing at all times. Convection responds instantaneously to changes in the large-scale forcing and exactly balances out the effects of the large-scale dynamic and thermodynamic fields, that is, the atmospheric disturbance generated by the large-scale forcing is stabilized as a result of convective activity. Further, the diagnostic assumption states that the convective response at any instant can be determined solely using grid-scale variables at that instant and that there is no dependence of convection on its own past behaviour.

These idealized assumptions have been traditionally employed as closure conditions to simplify the parameterization process. However, in reality, they do not hold true as convective activity takes a finite adjustment time to respond to variations in the large-scale forcing and also tends to persist for a specific time period (known as the "life cycle" of a convective system, Davies et al., 2009). The large-scale forcing itself may vary on relatively short time scales, making it difficult for the convective response to "keep up" (Jones and Randall, 2011). In such a situation, convection is not always in equilibrium with the environment and is determined or influenced at any instant by its history. The failure of these assumptions becomes especially stark with increasing model resolutions in time and space as convective systems are generated more frequently and the forcing is allowed to vary more rapidly (Jones and Randall, 2011).

The challenges posed by the QE and diagnostic assumptions can only be addressed by attempting to at least partly relax them; that is, by introducing prognostic components into parameterization schemes which are explicitly evaluated at each time step and can therefore render the scheme sensitive to its past behaviour. In other words, convection schemes need to possess some form of "memory" of their convective history so as to more realistically predict their future evolution. Section 1.1.3 elaborates on several broad methods employed to improve parameterizations schemes, including those aimed at endowing schemes with a memory.

1.1.3 Attempts to Improve Parameterizations

In the last few decades, diverse efforts have been directed toward improving the accuracy and realism of convective parameterization schemes. In their recent review, Rio et al. (2019) provide a comprehensive summary of these attempts which aim to improve the representation of a broad range of convective processes and phenomena.

At the foundational level, numerous developments have been aimed at improving the representation of convective cloud ensembles (Rio et al., 2019). Current GCMs use separate parameterization schemes and physical assumptions for the different regimes of convection and cloud formation: dry boundary-layer mixing, shallow moist convection (with cumulus clouds), and deep moist convection (with cumulonimbus clouds). This leads to discontinuities and biases in the simulation of these otherwise gradual, continuous processes within each model grid cell. Attempts have been made since the early 2000s to unify multiple convective regimes within a single parameterization scheme—an approach emphasized by Arakawa (2004)—either by adopting an eddy-diffusivity/mass-flux (EDMF) approach (e.g., Suselj et al., 2019) or by triggering deep convection from shallow convection processes (e.g., Hohenegger and Bretherton, 2011). Other methods to improve the representation of cloud properties has been to adopt stochastic rather than discrete deterministic models of entrainment (e.g., Romps, 2016; Romps and Kuang, 2010) and of the relative area fractions of different cloud types (e.g., Khouider et al., 2010). In particular, Sušelj et al. (2013) combined the EDMF and stochastic entrainment techniques in a parameterization scheme and obtained realistic simulations of moist conserved variable profiles and updraft properties.

On a more complex process-oriented level, recent improvements have been directed toward the incorporation of convective memory and organization in parameterization schemes (Rio et al., 2019). As described in Section 1.1.2, the diagnostic quasi-equilibrium formulation of convection fails to hold true as convection can take a finite time to adjust to variations in the large-scale forcing, resulting in a dependence of convection on its own history (Jones and Randall, 2011).

Convective parameterization schemes have attempted to account for this memory effect through the inclusion of several prognostic variables or through explicit simulation of physical processes responsible for memory such as cold pools and mesoscale convective systems (Rio et al., 2019). The concept of convective memory is central to our study which aims to identify and quantify the properties of memory within convective parameterization schemes. A detailed description of convective memory, its physical mechanisms, and attempts to include memory in parameterization schemes is presented in Section 1.2.3. Besides memory, GCMs also struggle to capture the process of mesoscale convective organization and its effects. Few previous attempts have been made to represent mesoscale circulations through, for instance, the use of water budgets (Donner, 1993) or vertical wind shear (Yano and Moncrieff, 2016). Future studies are required to understand in-depth the different mechanisms contributing to convective organization and the precise relationships between memory and organization.

Finally, convective parameterizations need to better account for the mutual interaction between convective processes and the large-scale dynamics (Rio et al., 2019). Progress in this regard can be achieved through extensive use of observational data (such as profiles of vertical velocity, mass flux, heating rates) to test parameterization schemes, identify model biases, and constrain relevant scheme parameters. Adopting a multiscale modelling approach with the simultaneous use of large-eddy simulations (LESs) and cloud-resolving models (CRMs) alongside GCMs for different regimes of interest will also prove helpful to diagnose systematic model errors and better understand the coupling between the model physics and the dynamics (Arakawa, 2004).

Significant progress has been realised since convective parameterizations were first developed half a century ago. However, extensive efforts must continue to be undertaken in the coming decades to make headway in addressing the challenges outlined in this section. It is essential that observations and model simulations are also used to identify additional physical processes that require parameterization, to understand interactions and/or feedbacks between convective schemes and other model parameterizations (e.g. radiation, microphysics), and to detect model performance at grey-zone resolutions (Rio et al., 2019).

1.2 Convective Memory

"I never wish to be easily defined."
— Franz Kafka

Section 1.1 discussed the characteristics and limitations of convective parameterization schemes, including their inability to take into account the past behaviour or "memory" of convection. Convective memory can be broadly defined as the effect or influence that convection at a previous time has on present convection and its future evolution (Davies et al., 2009; Colin et al., 2019; Daleu et al., 2020). The exact definition of memory, however, has varied from one study to another. A brief review of previous studies on convective memory is provided in Section 1.2.1, while Sections 1.2.2 and 1.2.3 summarize the sources of convective memory and examples of previous attempts to include memory in convective parameterization schemes.

1.2.1 Previous Studies on Convective Memory

Davies et al. (2009) were among the first to directly and explicitly examine the role of memory within a convective system. They introduced a simple mathematical model to study the effects of varying the memory time scale, which was taken to be the adjustment time for the convective system to respond to changes in the large-scale forcing. Davies et al. (2009) correlates memory with significant day-to-day variability in the convective response, where each day responds to the forcing in a different manner due to convective feedbacks from the previous day. Their results are reproduced in Figure 1 below. They found that for very short memory time scales (<6 hours), the convective response adapts quickly to the forcing and hence can be assumed to be in quasi-equilibrium with the environment (Figure 1A). For very long memory time scales (>20 hours), convection is seen to be almost unchanging and independent of the variations in the forcing (Figure 1B). The role of memory becomes significant for intermediate time scales (6–20 hours) over which the convective activity is dependent on the variations in the forcing and takes a finite time to respond to them, giving rise to an internal feedback within the system (Figure 1C–D).

Other previous studies have attempted to explore different aspects of convective memory using CRM simulations. The typical grid-spacing of CRMs is on the order of a hundred metres which allows them to explicitly model individual cloud behaviour and life cycles, unlike GCMs (Guichard and Couvreux, 2017). This explicit treatment enables CRMs to investigate the impacts of past convective history on present deep convection. Different studies use different ways to quantify convective memory, as discussed below.

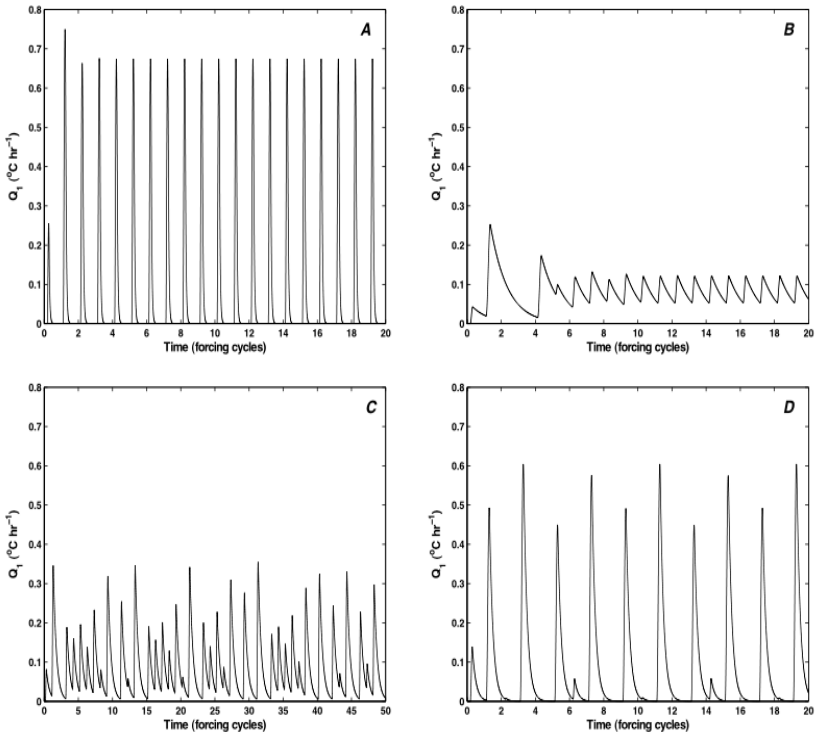

Figure 1: The convective heating rate $Q1$ (variable representing convective activity) produced in response to a large-scale diurnal forcing for different memory or adjustment time scales of (A) 1 hour, (B) 24 hours, (C) 11 hours and (D) 5 hours. Reproduced from Davies et al. (2009) (*their* Figure 1).

Davies et al. (2013) studied the effects of memory in response to varying forcing time scales in CRM simulations. Again, memory is qualitatively identified as the cycle-to-cycle variability present in the induced convective response; variability implies memory communicated from one cycle to the next. The pattern of surface forcing used was sinusoidal and active only during the first half of each cycle, similar to the forcing adopted in our study. Long forcing periods on the order of 24 hours or more produced identical cyclical behaviour in the cloud-base mass flux. Short forcing periods on the order of 1 hour also produced repetitive convective cycles, with minor modulations from the equilibrium response. Consistent with Davies et al. (2009), departures from quasi-equilibrium occurred at intermediate forcing time scales of 3–12 hours, with the convective response varying in an anti-correlated manner from one cycle to the next. Using these results, Davies et al. (2013) also suggested that small-scale spatial thermodynamic variability from previous convection may be a potential source of memory between cycles. Over longer forcing time scales, the thermodynamic fields produced from convective activity become smooth, preventing feedbacks from being communicated to the start of the next cycle.

Colin et al. (2019) attempted to identify the variables contributing to "microstate" or sub-grid-scale convective memory—memory occurring on spatial scales smaller than that of a GCM grid

cell—and examine the link between memory and spatial organization of convection. In their study, microstate fields were perturbed by homogenization across the domain, and memory was quantified using the time taken for convection to return to radiative-convective equilibrium with the environment. They found that memory increases as organization increases and that thermodynamic fields (temperature and water vapor) contribute more to memory on average than winds and hydrometeor variables.

More recently, Daleu et al. (2020) investigated memory properties of the diurnal cycle of scattered, deep convection using high-resolution three-dimensional CRM simulations, and their methodology forms the basis of our study. Convective memory was investigated using surface precipitation fields. To quantify the dependence of convection on its own history, Daleu et al. (2020) defined a memory function over a certain area A as the difference of two probabilities: the probability of finding rain over an area A at both the present time t_0 after the start of convection and at a previous time $t_0 - \Delta t$ minus the probability of finding rain at the two different times t_0 and $t_0 - \Delta t$ if convection had no memory and the two rain events could be treated as independent events that occurred by random chance. The mathematical form of the memory function used was as follows:

$$\mathbf{M}(A, t_0, \Delta t) = P[R(A, t_0) \cap R(A, t_0 - \Delta t)] - P^2[R(A, t_0, \Delta t)] \tag{2}$$

In separating the effects of random chance, the memory represents the influence that previous convection at time $t_0 - \Delta t$ has on the probability of present convection at time t_0. Positive memory or $\mathbf{M} > 0$ indicates that memory from previous convection increases the probability of current convection, while negative memory or $\mathbf{M} < 0$ indicates that memory acts to reduce the probability of present convection relative to a no memory situation.

Equation (2) was used to examine the dependence of memory on time and length scales as well as on forcing strengths. Unlike Davies et al. (2009) and Davies et al. (2013) who studied cycle-to-cycle memory effects, Daleu et al. (2020) focuses on intra-cycle memory which was found to be predominant on timescales of 1–9 hours after the start of convection. Memory was seen to vary in a three-phased manner, with the initial phase (0–1 hr in duration) representing the persistence of existing convection, the second phase (1–3 hr) representing the suppression of convection in areas previously raining, and the third phase (3+ hr) representing a secondary enhancement of convection in areas previously suppressed. Moreover, memory was observed to be strongest at gray-zone scales of 4–10 km and reduced greatly at scales of 25 km and greater. Similar to Colin et al. (2019), Daleu et al. (2020) also attempted to assess the convective memory associated with initial spatial thermodynamic variability by applying homogenization across

the domain prior to the start of each diurnal cycle. The phases of memory were found to occur earlier following homogenization relative to the control, due to the reduced intensity of rainfall events when thermodynamic feedbacks from the previous day are not taken into account.

These studies convey that convective memory can exist on a range of temporal scales, from a few hours to longer than a day. On shorter time scales, memory causes a local strengthening or weakening of convective activity within the diurnal cycle, while on longer time scales, memory influences the amplitude and timing of the diurnal cycle of convection from one day to the next. Most importantly, both forms of memory can coexist within any convective system.

1.2.2 Sources of Convective Memory

As Davies et al. (2009) asserts, convective memory could arise from several different sources and physical mechanisms. As briefly discussed in Section 1.2.1, a strong source of convective memory is the small-scale (<20 km) spatial variability in water vapour and potential temperature fields in the lower troposphere (surface–700 hPa) (Stirling and Petch, 2004; Davies et al., 2013; Colin et al., 2019; Daleu et al., 2020). This thermodynamic or moist static energy variability arises as a remnant of previous convective activity and influences the development of future convection and precipitation (Colin et al., 2019). Cold pools, hot thermals, cloud entrainment/detrainment and evaporation of rain are candidate processes that could bring about this memory through the creation of microstate thermodynamic structures, though the precise mechanisms of cold pool activity as well as other processes remain poorly understood (Colin et al., 2019; Daleu et al., 2020). Wind fields can be an important memory source for wind-shear organized convection, and convective organization itself, while not a memory "source", is an additional factor contributing to convective memory through its effect of lowering convective available potential energy (Colin et al., 2019).

Our study focuses solely on microstate memory which remains unresolved in GCMs. However, as Colin et al. (2019) explains, convective memory can also reside on the grid-scale, known as "macrostate" memory, and on the scale of multiple grid cells, known as "synoptic-state" memory. Macrostate memory on the order of 100 km could arise from grid-scale tropospheric temperature and humidity fields and large-scale stratiform precipitation, while synoptic-state memory on the order of 1000 km could arise from large-scale circulations and synoptic weather features such as storms and fronts (Scinocca and McFarlane, 2004; Colin et al., 2019). Since they occur on spatial scales equal to or larger than the grid-scale, both macrostate and synoptic-state memory processes are resolved by GCMs through their convective parameterization schemes and their simulations of atmospheric motion (Colin et al., 2019).

While recent studies have been able to demonstrate which variables contribute to memory, more investigations on the convective processes that lead to memory and the resulting feedbacks generated are required in the future. The relative importance of different thermodynamic processes also needs to be quantified more robustly in a diverse set of convective conditions (Colin et al., 2019).

1.2.3 Memory in Convective Parameterization Schemes

In order to overcome the deficiencies outlined in Section 1.1.2, numerous studies have attempted to incorporate the effects of sub-grid-scale memory into convective parameterization schemes through the addition of prognostic variables and the relaxation of the quasi-equilibrium and diagnostic assumptions of Arakawa and Schubert (1974). Pan and Randall (1998) introduced a prognostic cumulus kinetic energy (CKE) variable which is explicitly calculated for each cloud type in the model grid using the cloud-base mass flux and the cloud work function, thereby introducing a kind of memory for sub-grid-scale convection. Using a similar but linear relationship between CKE and cloud-base mass flux, Yano and Plant (2012) showed that the convective response under any constant large-scale forcing always follows a nonlinear finite periodic cycle that departs from quasi-equilibrium. Wagner and Graf (2010) also used a prognostic mass flux equation integrated to equilibrium in a cumulus parameterization scheme with a high-resolution entraining plume model. In explicitly determining cloud properties and vertical velocities, they obtained improved simulations of the magnitude and frequency of precipitation events.

Mapes and Neale (2011) introduced a prognostic qualitative "organization" variable to determine entrainment rates and found that accounting for organization within each grid cell leads to a positive feedback on the development of deep convection relative to randomly scattered convection. Piriou et al. (2007) separated grid-scale microphysics and transport terms and allowed for a prognostic treatment of the microphysics in a parameterization scheme which resulted in an improved representation of memory in various convective situations. Gerard et al. (2009) used a very similar approach with prognostic updraft area fraction, vertical velocity, and hydrometeor variables and observed a more realistic representation of precipitation at grey-zone scales. Chen and Bougeault (1993) and Guérémy (2011) both used a prognostic convective vertical velocity and found improvements in simulated convective behaviour and precipitation.

As Rio et al. (2019) explains, more recent attempts of including memory involve the explicit modelling of physical processes responsible for memory. Grandpeix and Lafore (2010) introduced a wake (cold pool) parameterization scheme with two prognostic variables for tempera-

ture and humidity differences between sub-grid wake and non-wake regions. Park (2014) also incorporated plume memory at each time step into a parameterization scheme with prognostic calculations of cold pools and mesoscale organized flow. Similar cold pool parameterizations using prognostic variables were attempted by Qian et al. (1998) and Del Genio et al. (2015).

Despite the attempts outlined above, however, there is a lack of consistency in the various approaches used which complicates efforts toward understanding memory mechanisms and deciding on how best to represent memory in models of the atmosphere.

1.3 The Diurnal Cycle of Convection

In Section 1.2, we introduced the physical basis and significance of convective memory, which can influence convective development on hourly (>1 hour) to diurnal (≥24 hour) timescales. To investigate the role of memory within convective parameterization schemes, our study looks at an idealized diurnal cycle of deep convection over land in the tropics. The diurnal cycle is a fundamental mode of variability in the global climate system, interacting extensively with various atmospheric budgets and processes including solar radiation, surface radiative fluxes, moisture, temperature, convection, and turbulence (e.g., Yang and Slingo, 2001). Due to the central role of the diurnal cycle in interacting with large-scale circulation, accurate and realistic model simulations of the diurnal cycle have been used over the past few decades as one robust test of the reliability of the physical parameterization schemes used in GCMs (e.g., Yang and Slingo, 2001; Bechtold et al., 2004). The following sections 1.3.1 to 1.3.3 will briefly discuss important features of the diurnal cycle of convection, difficulties in its simulation, and examples of previous studies that have focused on the diurnal cycle.

1.3.1 Features of Tropical Diurnal Convection

The Earth's tropics (30°N–30°S) experience a strong diurnal cycle of convection (Yang and Slingo, 2001). Due to the much lower heat capacity of land compared to water, the diurnal cycle is more pronounced over continents than over the oceans (Lin et al., 2000). Yang and Slingo (2001) provide a useful conceptual picture of the diurnal cycle mechanism over land. The diurnal cycle is caused by variations in incoming solar radiation over the course of a day which result in modulations in the surface temperature and surface fluxes of sensible and latent heat exchanged with the atmosphere. As incoming solar radiation increases gradually from sunrise, the land surface warms and exchanges heat with the atmosphere, increasing the temperature of the troposphere from below. This generates a vertically unstable atmospheric profile, resulting in convection, formation of shallow and deep convective clouds, and precipitation. Precipitation peaks in the late afternoon to early evening over land (around 3–4 pm), as evidenced by satellite and surface observations. After sunset, solar radiation is absent and the outgoing longwave radiation causes the surface and the atmosphere to cool and stabilize. Convective activity decreases and precipitation reaches a minimum in the early morning. The peak in precipitation generally occurs a few hours after the peak in surface temperature due to the time needed for shallow convection to transition into mid-level and deep convection (Lin et al., 2000). Additionally, the peaks in cloud height and cloud top minimum temperatures occur a few hours after the precipitation maximum as clouds continue to deepen and expand even after precipitation peaks (Lin et al., 2000).

Throughout the cycle, the surface fluxes, which constitute the large-scale "forcing", are in phase with the solar heating, peaking at noon and reducing to zero after sunset. In reality, the forcing itself interacts with and can be modified by convective activity through memory mechanisms (such as those described in Section 1.2.2) (Yang and Slingo, 2001). However, in our idealized study, we choose to keep the forcing non-interactive in order to study the effects of atmospheric memory alone. The diurnal cycle is also influenced by heterogeneous surface conditions such as orography and land-sea interactions (Yang and Slingo, 2001); however, again for the sake of simplicity, we choose a homogeneous land surface for our study. A complete description of our simulation setup is provided in Section 2.2.4.

1.3.2 Difficulties in Simulation

Given the ubiquity of the diurnal cycle, it is essential that weather and climate models are able to properly simulate the amplitude and phase of the variability in convection and precipitation. Historically, GCMs have struggled to reproduce the correct intensity and timing of precipitation over the tropics, with most GCMs tending to produce an earlier onset and peak of precipitation as well as reduced intensity than what is observed (e.g., Bechtold et al., 2004; Guichard et al., 2004; Lin et al., 2000; Yang and Slingo, 2001). In fact, these biases persist even in many of the most recent models (e.g., Christopoulos and Schneider, 2021). The tendency of GCMs to respond too quickly to the surface forcing has been attributed to limitations in the convective parameterization schemes used, which result in an imperfect representation of several convective processes within the diurnal cycle (e.g., Betts and Jakob, 2002; Bechtold et al., 2004). For instance, as described in Section 1.1.3, most parameterizations separately evaluate the different regimes of convection (dry, shallow, and deep) instead of treating the process as a continuum, and this can lead to a neglect of the shallow cloud growth phase before deep convection sets in (Betts and Jakob, 2002).

In addition to the general shortcomings of parameterization schemes described in Section 1.1.2, the complexity and difficulty of the diurnal problem lies in the fact that different atmospheric processes interact closely on various spatial scales to produce the diurnal cycle, and the erroneously simulated cycle itself feeds back onto different components of the parameterization schemes employed. Over the past several decades, a wide range of efforts have been undertaken with the goals of improved physical understanding and modelling of the diurnal cycle of convection. These are summarized in Section 1.3.3 below.

1.3.3 Previous Studies on the Diurnal Cycle

Previous studies have attempted to simulate the diurnal cycle using a combination of modelling and observational approaches. Studies focused on better understanding features of the diurnal cycle have typically involved CRM or single-column model (SCM) simulations initialized with observations. As explained earlier in Section 1.2.1, a CRM enables explicit modelling of cumulus convection without the need for parameterizations (Sato et al., 2009), while an SCM is a one-dimensional, single-grid version of a GCM containing the same physical parameterization schemes (Guichard et al., 2004). CRM and SCM results have also been used in combination to test and improve GCM parameterizations based on their ability to reproduce a realistic diurnal cycle.

Using CRM simulations of an idealized diurnal cycle, Stirling and Petch (2004) found that deep convection intensifies and occurs earlier when moisture and temperature fluctuations generated from the previous day's convection are included in the initial conditions. As part of the Global Energy and Water Cycle Experiment (GEWEX) Cloud System Study (GCSS) within the Atmospheric Radiation Measurement (ARM) program, Xu et al. (2002) and Xie et al. (2002) performed an intercomparison of several CRM and SCM parameterizations under summertime midlatitude continental conditions. They found that while CRMs agreed well with observations, SCMs could not accurately simulate convective events and surface precipitation due to possible deficiencies in the triggering mechanism. In the EUROpean Cloud Systems (EUROCS) project, Guichard et al. (2004) also simulated an idealized diurnal cycle over land using CRMs and SCMs and found that SCMs predicted an earlier onset of rain compared to the CRMs. Bechtold et al. (2004) and Chaboureau et al. (2004) further investigated the physical reasons behind SCM deficiencies, noting that SCM parameterizations were unable to properly reproduce the cloud growth process from shallow to deep convective regimes.

Several studies have also been directed at diagnosing and rectifying the errors in convective parameterization schemes. Stratton and Stirling (2012) were able to improve the diurnal cycle represented over land in an SCM parameterization by reducing the entrainment rate as the lifting condensation level (LCL) increases. Rio et al. (2009) also obtained a more realistic diurnal cycle through a better representation of boundary-layer thermals and wakes which improve the triggering and continuation of deep convection. Similar attempts were made by Bechtold et al. (2014), who introduced an extended CAPE-dependent closure coupled to the boundary layer forcing, and by Folkins et al. (2014), who allowed the initiation of convection from multiple near-surface layers instead of a single layer.

Another approach that has proved useful in improving simulations of the diurnal cycle is "superparameterization" or the "multiscale modelling framework" (MMF), which involves using a 2D CRM within each grid box of a 3D GCM in place of the parameterization scheme (Grabowski, 2001; Khairoutdinov and Randall, 2001). The CRMs explicitly resolve convection in each grid box and interact with each other through the large-scale circulation simulated by the GCM. Using superparameterized GCMs, Khairoutdinov et al. (2005) and Tao et al. (2009) obtained improved diurnal cycles over land and ocean, with the frequency and timing of precipitation closely agreeing with observations. Zhang et al. (2008) were able to capture the precipitation maximum, land-sea contrasts, and upper tropospheric relative humidity of the diurnal cycle in an MMF. DeMott et al. (2007) found that an MMF version of a GCM was able to properly simulate the evolution of atmospheric thermodynamic variability during the diurnal cycle, unlike the regularly parameterized version.

Despite these promising results, the high resolution of CRMs renders both CRM studies and superparameterization approaches computationally expensive and unsuitable for longer, statistically steady time integrations. It is therefore essential that efforts continue to be devoted to testing and improving convective parameterization schemes in the near future. This can only be achieved with a clearer understanding of sub-grid convective processes and organization in GCMs, which in turn can lead to a better incorporation of memory effects in convective parameterization schemes.

2. Our Study

"If we knew what we were doing, it wouldn't be called research."
— Albert Einstein

The previous section (Section 1) provided the scientific basis of our study. We reviewed the need for and issues with traditional convective parameterizations (Section 1.1), introduced the concept of convective memory (Section 1.2), and discussed the problem of simulating the diurnal convective cycle (Section 1.3). In this section, we elaborate on the specifics of our study, including our aims, methods, and results. Section 2.1 discusses our research motive and the questions we wish to address, Section 2.2 outlines the models and parameterization schemes employed, and Section 2.3 presents our methods and research findings.

2.1 Introduction and Aims

Our study builds directly on that of Daleu et al. (2020), which was described in Section 1.2.1. We aim to compare the memory properties of different convective parameterization schemes in GCMs with those found in CRM simulations (which for the purpose of our study are taken to represent the "true" convective behavior). We use the Met Office NERC Cloud model (MONC) and the Unified Model (UM) with two different parameterization schemes: CoMorph and the 6a convection scheme. The 6a convection scheme is the current parameterization scheme used in the Unified Model and is largely based on Gregory and Rowntree (1990). CoMorph is a new scheme being developed by the Met Office under the Parameterization of Convection (ParaCon) programme with the aim of improved physical representation of convective processes, model accuracy, and performance (Whitall, 2019). More specifically, our study aims to identify whether CoMorph shows an improvement over the 6a scheme, and if so, how memory properties of CoMorph can be further enhanced by modifying various settings within the parameterization scheme.

We define memory on the basis of 2D surface precipitation fields over the domain, using conditional probabilities of rain events occurring at a given time and area relative to previous convection (as expressed mathematically in Equation (2)). For each model type and parameterization scheme, we study the dependence of memory on different temporal and spatial scales. The convective test case used in our study is that of an idealized diurnal cycle of tropical convection as done by Daleu et al. (2020). In addition to memory, we also analyze and compare other convective properties of significance including surface precipitation, mass-flux, and cloud fraction within the different diurnal cycles. Detailed descriptions of the models, convection schemes, and model settings are given in Section 2.2 below.

2.2 Model and Scheme Descriptions

"Essentially, all models are wrong, but some are useful."
— George E. P. Box

In the following sections 2.2.1 to 2.2.3, we provide descriptions of the Met Office NERC Cloud Model (MONC), the Unified Model (UM), and the two convective parameterization schemes (6a and CoMorph) employed within the UM. Finally, we outline our simulation setup in Section 2.2.4.

2.2.1 Met Office NERC Cloud Model (MONC)

The Met Office NERC Cloud Model (MONC) is a re-write of the Large Eddy Model (LEM) used in the Met Office for explicit cloud simulations (Brown et al., 2020). Since the 1980s, the LEM has been used to study atmospheric phenomena and to test the Unified Model's physical parameterization schemes (e.g., Marsham et al., 2006; Hill et al., 2014). MONC continues to serve the same purpose with improved scalability, performance, and compatibility with the latest high-performance computing technology (Brown et al., 2020).

MONC uses a newly developed bulk cloud microphysics scheme known as the Cloud AeroSol Interactions Microphysics (CASIM) model (Grosvenor et al., 2017). Designed to be more sophisticated than the old microphysics package used in the LEM, CASIM consists of prognostic variables for different hydrometeor species such as vapour, liquid water, snow, ice and graupel, and performs computationally expensive calculations of the interactions between these variables in the atmosphere (Grosvenor et al., 2017).

2.2.2 Met Office Unified Model (UM)

The Unified Model (UM) is a numerical model that has been used in the Met Office since the 1990s for weather and climate modelling on a wide range of spatial and temporal scales (Cullen, 1993). It is a fully compressible and deep non-hydrostatic model of the atmosphere, and can be coupled to land, ocean and sea ice components as required. The model integration occurs using a semi-implicit semi-Lagrangian (SISL) numerical scheme over a regular latitudinal and longitudinal coordinate grid or an idealised Cartesian grid (as in this study). Horizontal and vertical resolutions are variable, with horizontal grid sizes in the range of 1–50 km and the vertical grid typically consisting of about 70 levels. The UM is extremely versatile and flexible, allowing for different possible configurations depending on the exact needs of the user.

Parameterization schemes are used for different sub-grid processes including convection, radiation, boundary layer turbulence, and cloud microphysics. The radiation scheme, which represents the interaction of shortwave and longwave radiation with the surface and the atmosphere, is based on Edwards and Slingo (1996). The current boundary layer mixing and turbulence scheme is based on Lock et al. (2000). Gravity wave drag due to orographic and non-orographic sources are parameterized using schemes proposed by Lott and Miller (1997) and Scaife et al. (2002) respectively. The microphysics scheme which evaluates large-scale precipitation is that of Wilson and Ballard (1999). Details of the current convection schemes in use are outlined in Section 2.2.3 below.

2.2.3 CoMorph and the 6A Convection Scheme

As briefly mentioned in Section 2.1, the current convective parameterization scheme being used in the UM is known as the "6A convection scheme" and has been in operation for the last three decades (Gregory and Rowntree, 1990). A new scheme called "CoMorph" is currently being developed and tested as a potential improved operational scheme that could replace the 6A scheme. CoMorph was initiated in Phase 1 (2016–2019) of the ParaCon programme organized jointly by the Met Office and NERC. Its capabilities are now being rigorously tested under different scenarios in Phase 2 of the programme (2019–present).

CoMorph and the 6A scheme are fundamentally similar in the following respects (e.g., Walters et al., 2019; Saffin et al., 2021):

1. Both schemes are diagnostic and based on the traditional mass-flux framework described in Section 1.1.1.

2. Convection is coupled to and diagnosed by testing for buoyant ascent from within the boundary layer.

3. Convection in each grid box is represented as a single "bulk" plume which represents the statistical average of convective clouds over the whole grid cell.

In an attempt to improve the efficacy of the parameterization, several assumptions used within the 6A scheme are relaxed within CoMorph to allow for a more flexible and generalized approach (Whitall, 2019). This results in some key differences between the two schemes, which are as follows (Saffin et al., 2021):

1. The 6A scheme uses three different schemes to simulate shallow, mid-level and deep convection respectively, while CoMorph adopts a unified adaptive scheme for all convective regimes.

2. In the 6A scheme, the vertical structure of convection is prescribed with a predetermined cloud base height. In contrast, convection can be initiated at any height within CoMorph where vertical instability is present (see Figure 2).

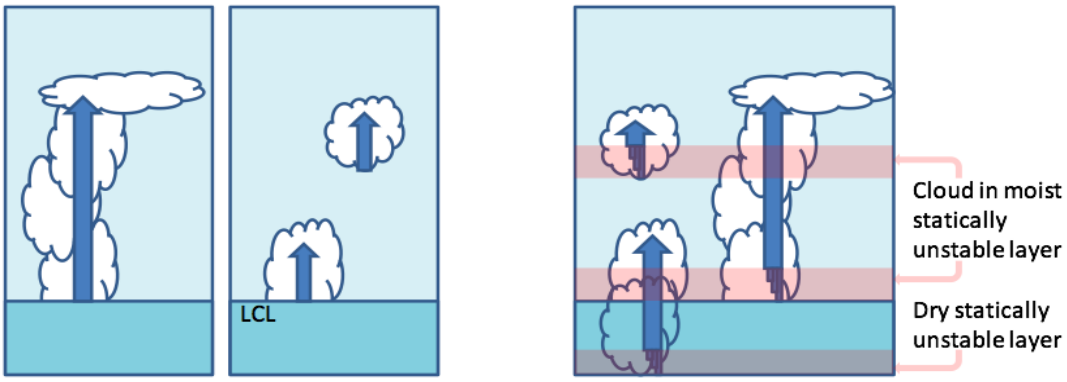

Figure 2: Some schematic differences in convection between the 6a scheme (left) and CoMorph (right). Cloud-base height is predetermined and separate schemes exist for different convective regimes in 6a. Parcels can ascend from any arbitrary height in CoMorph and a unified scheme is adopted regardless of regime. Reproduced from Whitall (2019).

3. The 6A scheme employs cloud-base mass-flux as a closure variable which is rescaled to conserve CAPE and vertical velocity budgets, whereas CoMorph allows mass-flux to be determined locally from the static stability of the environment.

4. In the 6A scheme, the microphysics is very simple and uses a fixed freezing threshold of 0°C, while the microphysics scheme within CoMorph allows air parcels to hold mixed-phase cloud and to become supersaturated.

5. The 6A scheme uses an empirically determined entrainment function which can be modified based on precipitation and convection from the previous time step. CoMorph uses a model of spherical buoyant air masses to evaluate the entrainment profile on the basis of changing parcel radius, mass, and density with height.

6. Detrainment in the 6A scheme occurs through environmental mixing and buoyancy sorting, while CoMorph determines detrainment through buoyancy sorting alone. Moreover, detrainment in CoMorph assumes a probability distribution function of cloud buoyancy values, while the 6A scheme uses a single value of buoyancy in each cloud.

7. In the 6A scheme, a downdraught scheme models the process of precipitation starting from the cloud parcel to the surface, including any evaporation or melting along the way. In CoMorph, surface precipitation is handled by the large-scale precipitation scheme after each height level absorbs precipitation into its prognostic fields.

8. The 6A scheme is explicit in nature as it accounts for changes in convective profiles at the start of each time step instead of at the end. This often results in overstabilization of the profile, leading to intermittent behaviour in the scheme. CoMorph involves an implicit numerical scheme and yields smooth behaviour by accounting for convective properties at the end of each time step.

Based on pre-operational trials and sensitivity tests (A. Lock, UKMO, 2021, personal communication), CoMorph has been shown to produce improved simulations of several tropical atmospheric components including high cloud, cloud forcing, surface fluxes, tropospheric humidity (see Figure 3), tropical cyclones, and the Madden-Julian Oscillation. However, the quality of the simulated diurnal cycle of convection does not show significant improvement (see Figure 4).

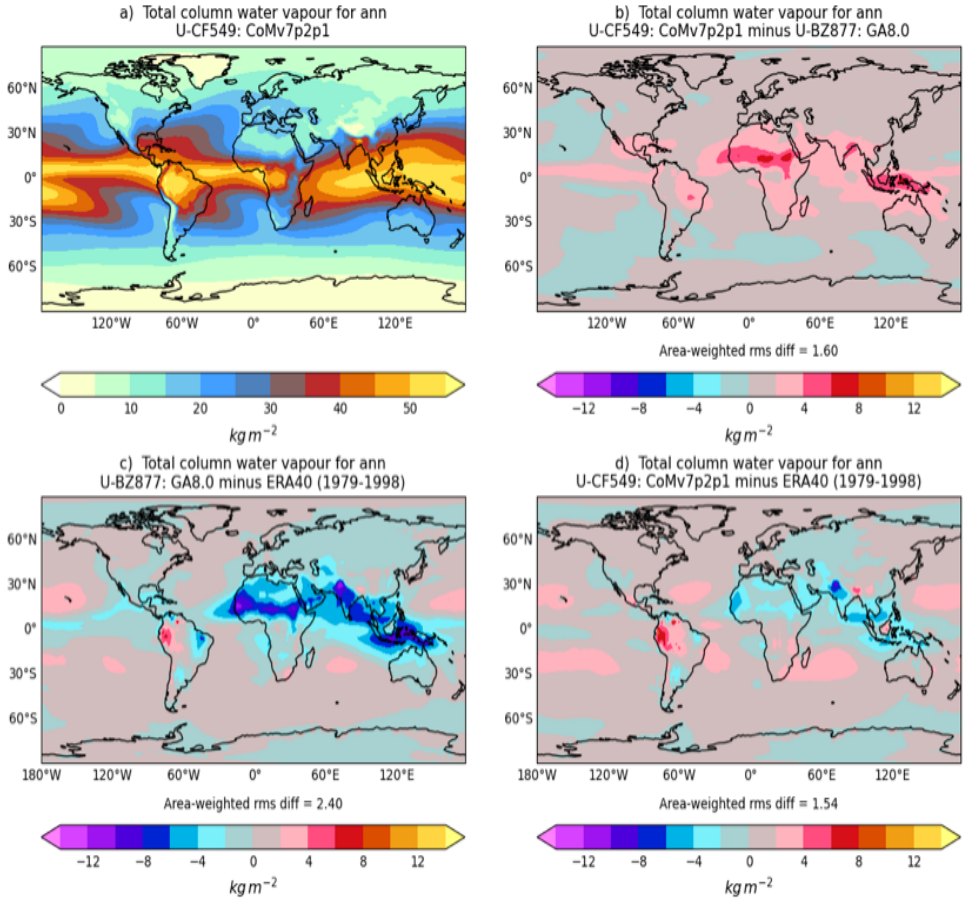

Figure 3: Plots showing total atmospheric column water vapour from current UM (global atmosphere and land configuration) simulations with a) CoMorph, b) CoMorph minus those with 6A convection scheme, c) 6A scheme minus ECMWF reanalysis (ERA-40) data of total column water vapour, d) CoMorph minus ERA-40 data. Comparing c) and d), it is evident that CoMorph is able to reduce the dry (negative humidity) bias over tropical land present in the 6A run. Reproduced from A. Lock, UKMO, 2021, personal communication.

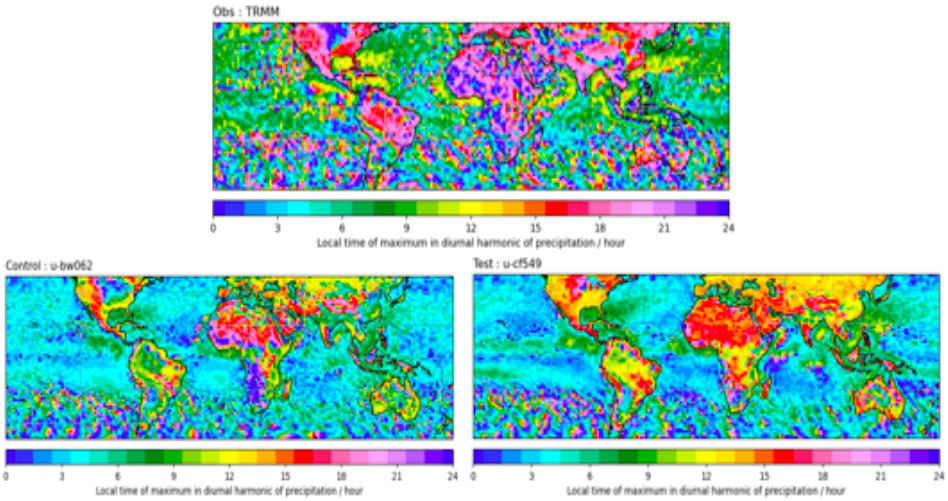

Figure 4: The local time of peak precipitation in the diurnal cycle over land as shown by Tropical Rainfall Measuring Mission (TRMM) observations (top) and as simulated by current UM (global atmosphere and land configuration) simulations with the 6A convection scheme (bottom left) and with CoMorph (bottom right). On average, CoMorph shows reduced accuracy in simulating the diurnal cycle compared to the 6A scheme. Reproduced from A. Lock, UKMO, 2021, personal communication.

2.2.4 Model Settings

For our study, we use the same simulation settings as adopted in Daleu et al. (2020). In MONC, our horizontal resolution is 200 m and the domain size is 102 x 102 km^2. There are 512 grid points in each horizontal direction and 99 grid points in the vertical direction. Our domain is assumed to lie at the equator with the Coriolis parameter equal to zero. Periodic boundary conditions are imposed on horizontal boundaries for all model variables. We use a non-interactive land surface so that we are able to evaluate memory arising solely from the atmosphere.

Each of the surface forcings, that is, the surface sensible and latent heat fluxes, is positive and sinusoidal during the day (0–12 hours after sunrise) when incoming solar radiation is positive, and set to zero at night (12–24 hours) (see Figure 5). To achieve statistically significant results, our simulation is run for 10 successive diurnal cycles starting from 6 AM in the morning on the first cycle. The peak values of surface fluxes are reached at noon when the sun is directly overhead, and each 24-hour day comprises a single forcing "cycle". The control forcing has peaks of sensible and latent heat fluxes equal to 130 and 400 W m^{-2} respectively. In order to balance the surface forcing, the atmosphere is subject to an idealized radiative cooling profile which represents the net effects of shortwave and longwave radiation (see Figure 6). The cooling rate is -1.75 K day^{-1} in the lowest 12 km of the atmosphere and decreases linearly to 0 K day^{-1} from 12 km to 15 km. The radiative profile at night involves an additional cooling of -3.1 K day^{-1} at the surface decreasing to 0 K day^{-1} at 1 km height. This ensures that convection does

not occur until after the start of the next diurnal cycle.

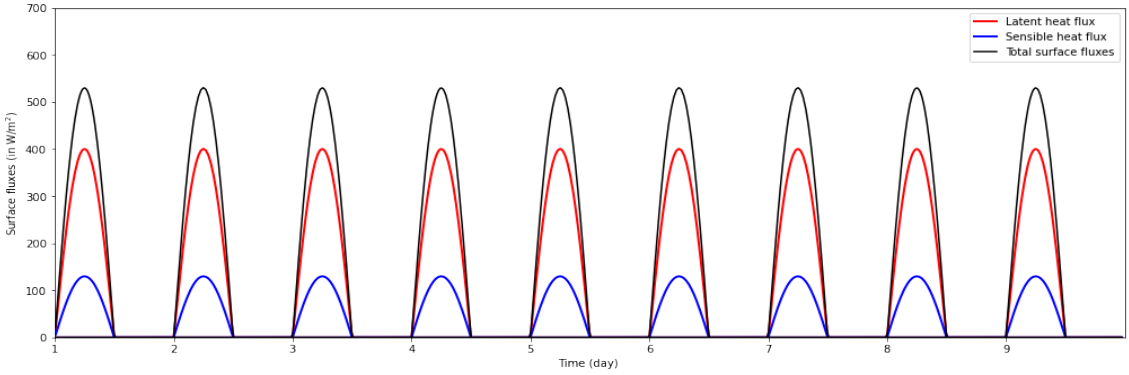

Figure 5: The time evolution of the surface fluxes comprising latent and sensible heat fluxes over the last nine days of our simulation. Latent heat fluxes are shown in red, sensible heat fluxes are shown in blue, and total surface fluxes are shown in black.

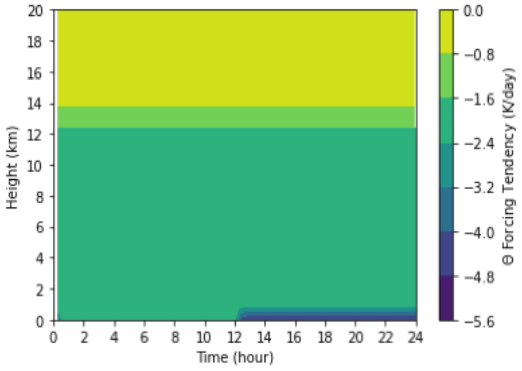

Figure 6: The radiative cooling profile (in K day^{-1}) applied to the atmosphere during each 24-hour diurnal cycle.

In the UM, we use the same settings as in MONC. However, we use different horizontal resolutions of 4, 10, and 50 km with the CoMorph parameterization scheme, in order to test the dependence of memory on horizontal spatial resolution. For the 6A scheme, we adopt a single horizontal resolution of 10 km. We also use a different domain size in the UM equal to 800 x 800 km^2, which remains constant for all UM simulations.

2.3 Methods and Results

"The first principle is that you must not fool yourself and you are the easiest person to fool."
— Richard Feynman

Sections 2.1 and 2.2 discussed the objectives of our study and the different models employed. In this section, we describe the scientific methods adopted and present the results obtained. In Section 2.3.1, we take a preliminary, qualitative look at the diurnal cycles of precipitation simulated by MONC and the UM using CoMorph and the 6A parameterization schemes. Next, we analyze and compare the behaviour of ensemble mean precipitation and convective properties in Sections 2.3.2 to 2.3.4. In Section 2.3.5, we evaluate and compare memory effects within the diurnal cycles produced by each simulation. We then study the magnitude of spatial thermodynamic variability arising from convection in the different simulations in Section 2.3.6. Finally, in Section 2.3.7, we investigate the changes in the memory properties of the CoMorph scheme in response to retuning various scheme parameters.

2.3.1 Preliminary Analysis

We begin by considering the behaviour of the domain-average surface precipitation for nine successive diurnal cycles, from the second to the tenth cycle of our simulation. We leave out the very first cycle when performing our analysis as our simulation is initialized with homogeneous thermodynamic conditions which are not realistic for the diurnal cycle, as Stirling and Petch (2004) showed. The subsequent nine cycles are influenced by convectively generated thermodynamic variability of the preceding day. Figure 7 shows the cycle-to-cycle convective response of surface precipitation for the MONC (CRM) and UM (GCM) simulations with the 6A and CoMorph parameterization schemes.

MONC simulations produce a steady convective response from one diurnal cycle to the next, without significant changes in amplitude and phase. Minor fluctuations between one cycle and the next can be attributed to the slightly different initial conditions affecting each convective cycle. Based on these characteristics, the convective regime produced by MONC can be said to correspond to the quasi-equilibrium regime of very short memory proposed by Davies et al. (2009) (as shown in Figure 1A). Convection responds quickly to the forcing, and each cycle carries little to no memory of the previous cycle.

UM simulations with CoMorph at 4 and 10 km horizontal resolutions show significant cycle-to-cycle variability within the nine days. The magnitude of peak precipitation decreases gradually from the start of the simulation, becoming approximately uniform after the 5th day of the simu-

lation. While not in exact correspondence with any of the memory regimes proposed by Davies et al. (2009), this behaviour does indicate the presence of longer term memory (on the scale of 24 hours and above) generated by the convective parameterization scheme. In the CoMorph simulations, the precipitation magnitude appears to equilibrate after about 5 days, suggesting that the memory effects set in at the start of the simulation and last for a few days. In the 6A simulation at 10 km resolution, the behaviour is even more unpredictable—the peak precipitation amplitude decreases over time and abruptly increases towards the end of the simulation. The shape of the precipitation curve also changes significantly from one day to the next. This suggests that memory effects might persist for longer than just a few days, perhaps for the entirety of the simulation with the 6A scheme. UM simulations with the CoMorph scheme at 50 km horizontal resolution are less variable in magnitude than the 4 and 10 km simulations, but do show some fluctuations in the shape of the diurnal cycle in the first few cycles.

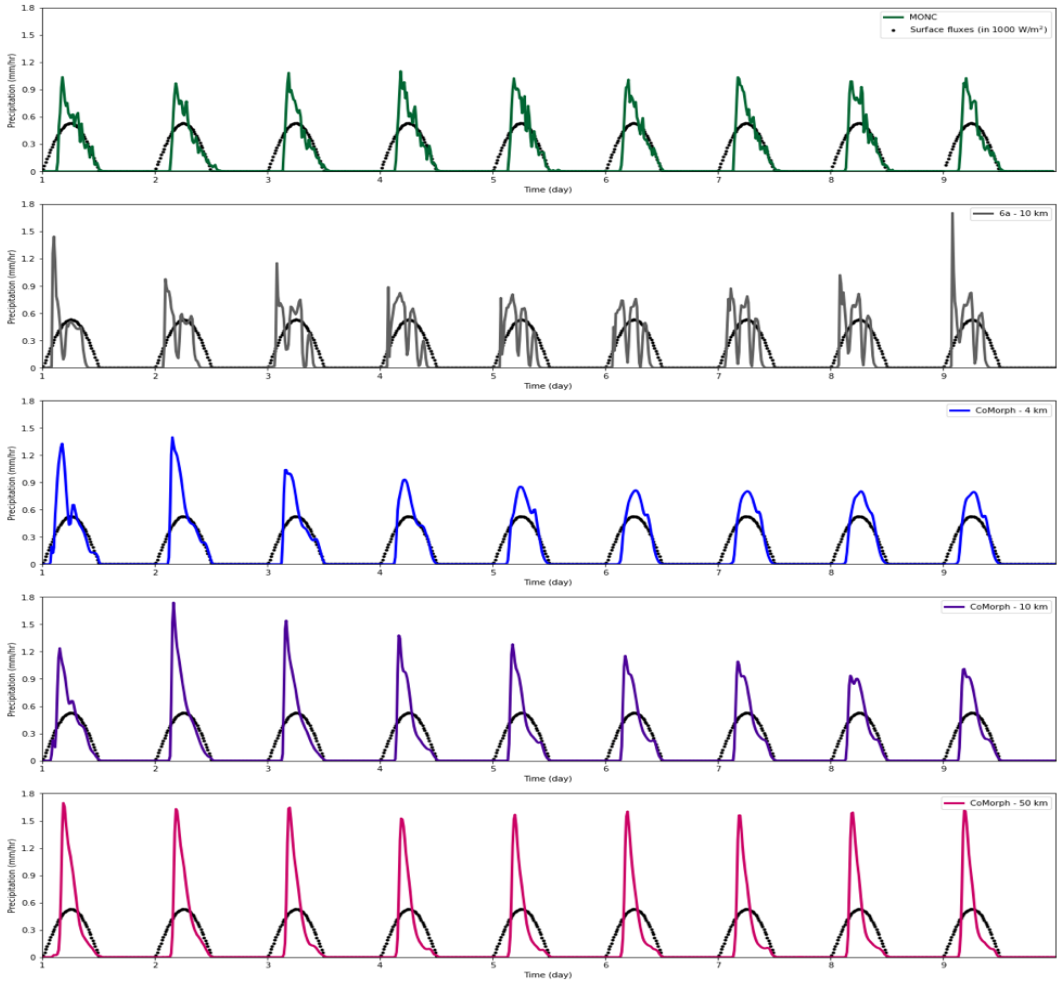

Figure 7: Surface precipitation (in mm hr^{-1}) is shown for the last nine successive diurnal cycles of each simulation, including MONC, UM 6A, and UM CoMorph (4, 10, 50 km) simulations. The total surface fluxes, that is, the sum of the latent and sensible heat fluxes, are also shown (in W m^{-2}, scaled by factor of 1000).

The day-to-day variability in the convective response produced by the two parameterization schemes is rather unexpected, given the unchanging precipitation series produced by MONC. The cause of the long-term memory is also unclear. However, one possible source of the memory could be the initial homogeneous thermodynamic conditions used at the start of the simulation, which may bias the initial response of the convection scheme until sufficient thermodynamic variability builds up and enables the scheme to reach an equilibrium with model variables and other model parameterizations. The initial conditions might also be linked to the fact that the first few cycles (days 1–3 in Figure 7) in the CoMorph 4 and 10 km simulations appear to trigger the onset of rain slightly earlier than subsequent cycles. Longer simulations of varying durations (20–50 days) must be run using both schemes to identify if this memory is simply a response to the initial conditions, or if it is a persistent feature of the convective parameterization scheme itself. In the case of the latter, scheme parameters will have to be tested and retuned in order to detect and possibly remove the source of unrealistic memory. In the case of the former, the simulation could potentially be initialized with naturally generated initial conditions to remove the unwanted long term memory. We attempt to investigate the cause of this memory by considering the day-to-day behaviour of convectively generated thermodynamic variability in Section 2.3.6.

For our analysis, which is focused on evaluating memory *within* each diurnal cycle, we need to neglect the effects of cycle-to-cycle memory which may bias our results. To work around this issue, we consider only the consecutively consistent cycles within each simulation. For the MONC simulations, all nine cycles are taken into consideration when evaluating ensemble mean convective and memory properties. For the CoMorph 4, 10, and 50 km simulations, we consider only the average of the last 4 cycles (days 6–9) and neglect the first five days during which cycle-to-cycle memory effects are assumed to be present. For the 6A simulation, cycles 5–8 are chosen for the analysis since they provide the most similar sequence. Figure 8 below shows the chosen set of cycles for each UM simulation, and the surface precipitation cycles simulated by MONC are also shown for comparison.

Hereafter, for simplicity, we refer to the diurnal cycle or day number in the UM simulations on the basis of Figure 8. For instance, the "second diurnal cycle" referred to in our analysis will imply the seventh diurnal cycle in the original CoMorph simulation (or the sixth diurnal cycle in the case of the 6A simulation). Original simulation day numbers (cycles 2–10) will be used when referring to the MONC simulation.

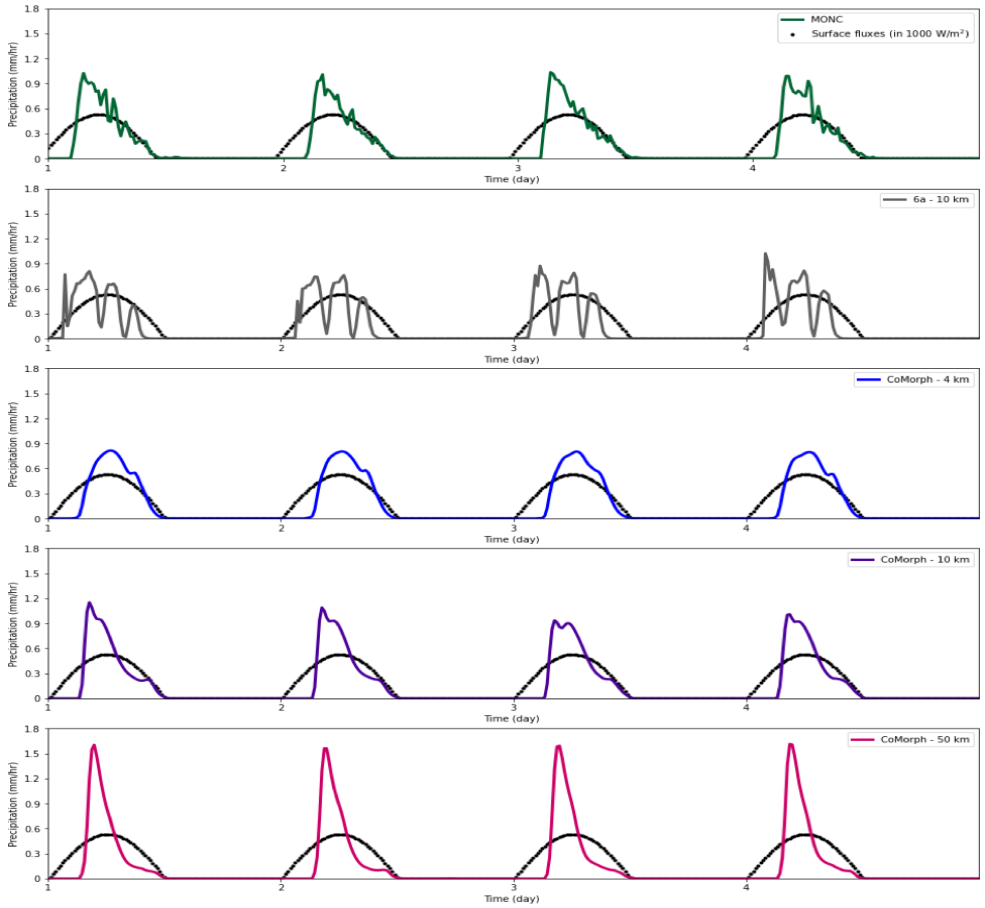

Figure 8: Surface precipitation (in mm hr^{-1}) is shown for four successive, steady diurnal cycles of each simulation. The total surface fluxes, that is, the sum of the latent and sensible heat fluxes, are also shown (in W m^{-2}, scaled by factor of 1000).

2.3.2 The Diurnal Cycle of Precipitation

Using our successive diurnal cycles, we evaluate the ensemble mean time series of precipitation for each simulation. The composite time series of surface precipitation simulated by MONC, CoMorph (4, 10, and 50 km), and the 6A scheme (10 km) are shown in Figure 9. The "triggering" time of the convective response is defined as the time at which convective activity begins and is typically diagnosed using the time of ascent or nonzero mass flux. Here, we assume that triggering occurs 15–30 minutes before the onset of precipitation in the diurnal cycle.

Daleu et al. (2020) describe in detail the convective response produced by MONC. Convection shows a triggering time of ∼2.75 hours after the start of day. Precipitation increases steeply right after triggering, reaching its peak value of 1.0 mm hr^{-1} at 4.5 hours (1.75 hours after triggering) and declining more gradually until the surface fluxes drop to zero. This general behaviour is shared by the CoMorph 10 and 50 km precipitation time series, with the magnitude

of the peak precipitation increasing for larger grid box sizes. The maximum precipitation values for the 10 and 50 km simulations are 1.0 and 1.6 mm hr^{-1}, respectively, and occur at 4.25 and 4.75 hours, respectively. The CoMorph simulation at 4 km shows a maximum precipitation of 0.8 mm hr^{-1} at 6.5 hours, but fails to produce the characteristic sharp diurnal peak. The domain mean daily mean values for all the CoMorph simulations are approximately 0.17 mm hr^{-1}, slightly below the MONC average of 0.2 mm hr^{-1}.

The precipitation time series produced by the 6A scheme differs greatly from those of MONC and CoMorph as it shows multiple peaks during the day and underestimates the precipitation rates throughout. 6A precipitation also shows a smaller domain mean daily mean value of 0.15 mm hr^{-1}, and a significantly earlier onset of precipitation compared to the MONC and CoMorph simulations. CoMorph simulations all appear to have triggering times at around 2.75–3 hours after the start of day like in MONC, while the 6A simulation is triggered at 1.25 hours. Overall, CoMorph simulates a much more realistic diurnal cycle than the 6A scheme, with the 10 km simulation most closely resembling the diurnal cycle produced by MONC.

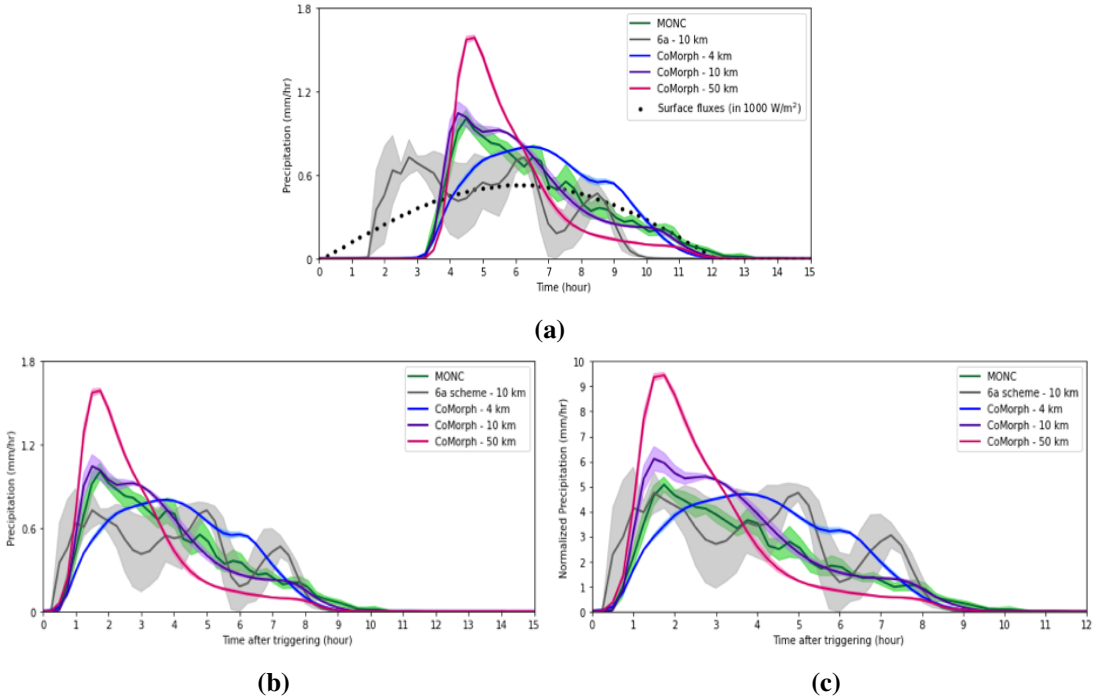

Figure 9: a. Composite time series of precipitation for the MONC (in green), CoMorph 4 km (in blue), CoMorph 10 km (in purple), CoMorph 50 km (in pink), and 6A (in grey) simulations. Ensemble mean and standard deviation values are shown by thick lines and shaded areas respectively. The surface forcing time series (sum of sensible and latent heat fluxes) is also shown, scaled by a factor of 10^3. b. Same as in a. but the time axis is shifted such that time equals zero corresponds to the time of convective triggering in all simulations. c. Same as in b. but the normalized precipitation time series (instantaneous precipitation divided by the domain mean daily mean precipitation) is shown instead.

2.3.3 Convective Properties over a Single Forcing Cycle

To be able to better understand and improve the characteristics of the convective response produced by CoMorph, we further investigate properties of mass flux and cloud fraction simulated by MONC and CoMorph. We evaluate the domain-mean mass flux ($M_{\text{domain}} = \rho w$, from Equation (1)) and domain-mean cloud fraction for each of our simulations. As in Daleu et al. (2020), we evaluate these properties for two conditionally sampled diagnostics: all cloudy updrafts ("ACu") and buoyant cloudy updrafts ("BCu"). All cloudy updrafts are represented by grid points with cloud liquid (q_l) or ice (q_i) mass mixing ratio greater than 10^{-5} kg kg^{-1} and with positive vertical velocity ($w > 0$). In addition to the above two criteria, buoyant cloudy updrafts also possess a positive virtual potential temperature anomaly with respect to the domain mean virtual potential temperature ($\theta_v' > 0$ K). The mass flux of ACu and BCu at each grid point satisfying the condition is calculated using the product of the air density ρ and the vertical velocity w. At each vertical model level, the domain-mean cloud fraction for ACu and BCu is defined as the number of grid points satisfying the criteria for ACu and BCu respectively, divided by the total number of grid points in the horizontal domain.

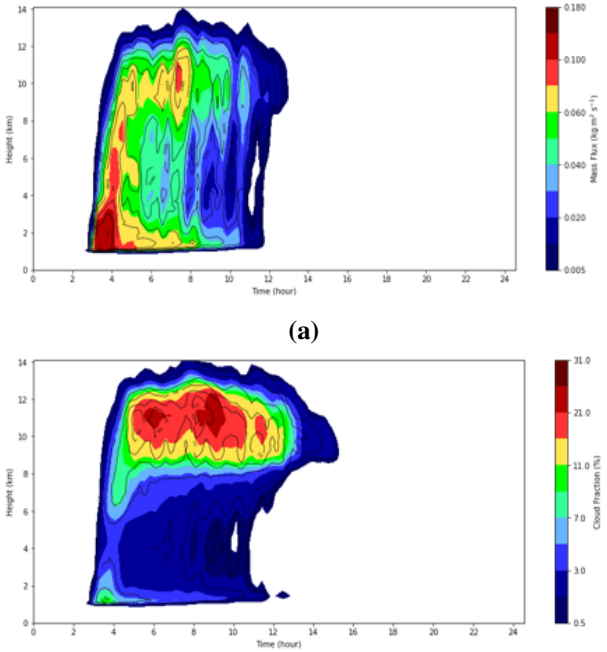

Figure 10: The time height-cross sections of a. mass flux per unit area (in kg m^{-2} s^{-1}) and b. cloud fraction (in %) for all cloudy updrafts ("ACu", in colours) and buoyant cloudy updrafts ("BCu", in contour lines) for the second day of the MONC simulation.

Figure 10 shows the time-height cross sections of the domain average mass flux and cloud fraction for the MONC simulation. The triggering of convection occurs when the mass flux first turns positive, which occurs at 2.75 hours. The convective response starts out shallow, leading

to a first peak in cloud fraction at the top of the boundary layer (∼1.5 km height) at 3 hours. Ascent of cloudy updrafts immediately continues higher into the troposphere, forming mid-level and high-level clouds which comprise a second peak in cloud fraction between 5–9 hours. The highest cloud tops occur at 14 km. In the upper troposphere, mass flux peaks at 7.75 hours after which convective activity decreases, ceasing completely between 15–24 hours. In the lower and middle troposphere, mass flux peaks at around 4 hours, after which cloud formation decreases and stops completely at 12 hours. As expected, the cycle in cloud fraction is delayed relative to the cycle in mass flux, given the time taken for clouds to develop and expand higher into the atmosphere.

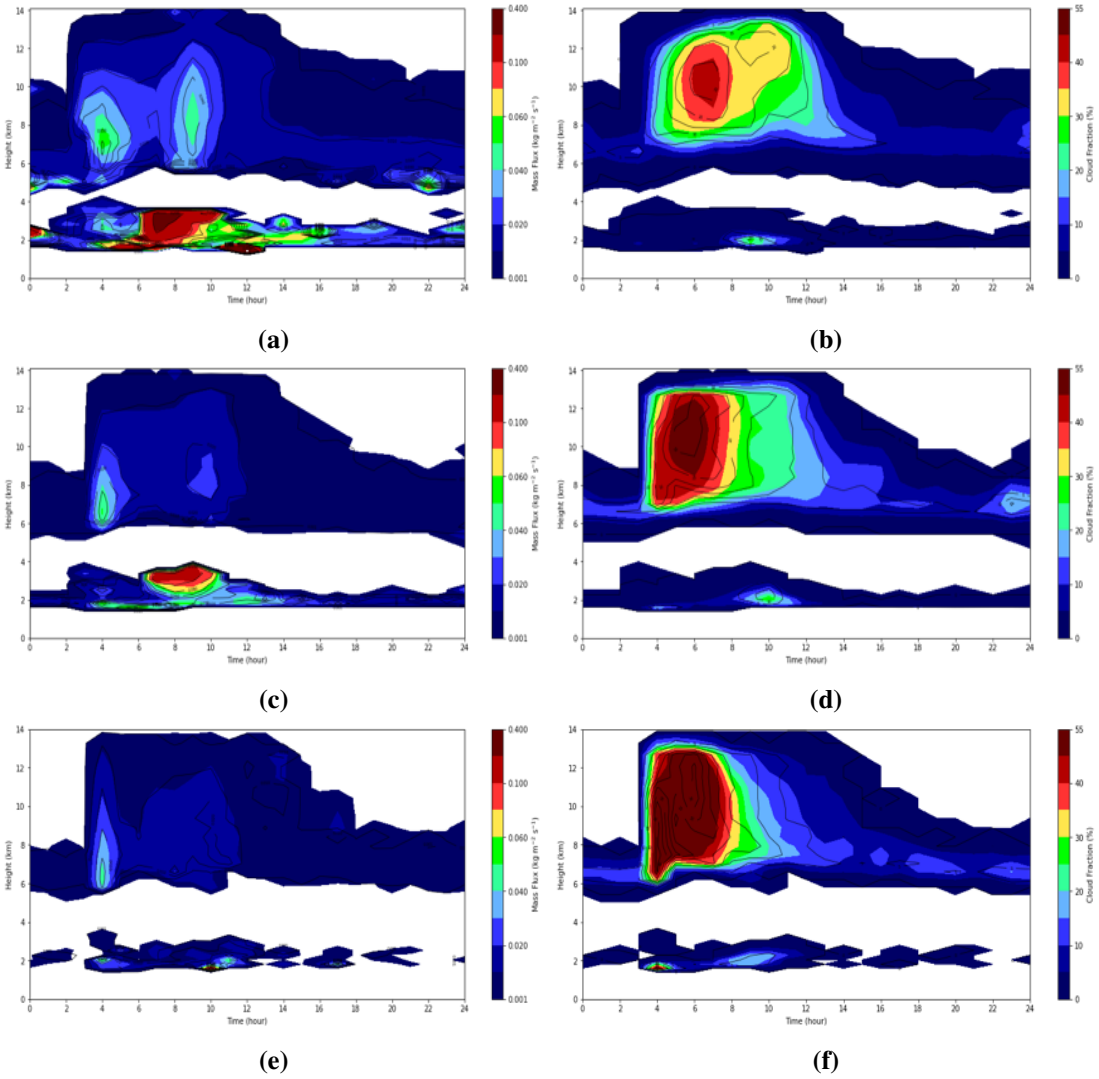

Figure 11: The time height-cross sections of a. mass flux per unit area (in kg m^{-2} s^{-1}) and b. cloud fraction (in %) for all cloudy updrafts ("ACu", in colours) and buoyant cloudy updrafts ("BCu", in contour lines) for the second (or eighth, as in Figure 7) day of the CoMorph 4 km simulation. c.-d. and e.-f. show mass flux and cloud fraction for the CoMorph 10 km and 50 km simulations respectively. Note that the contour values/intervals used are different from those used for MONC in Figure 10.

Figure 11 shows the time-height cross-sections of mass flux and cloud fraction from UM simulations with CoMorph at 4, 10, and 50 km resolutions. The convective response from the convective parameterization scheme shows significant differences from the resolved convective response. Mass flux and cloud fractions show a discontinuity between shallow (1.5–4 km) and deep convective (5–14 km) regimes. This is expected given that convective parameterizations generally use separate triggering conditions for boundary-layer, shallow and deep convection, as was described in Section 1.1.3. Mass flux decreases on average as horizontal resolution decreases, while cloud fraction increases marginally for larger grid sizes. Both mass flux and cloud fraction tend to be overestimated in the parameterized simulations compared to the resolved simulations. The peak in shallow convective mass flux occurs at around 7 hours in the 4 and 10 km simulations, which is a few hours later than in the MONC simulation. The peak in mid-level and deep convective mass flux occurs 2–3 hours earlier than in MONC and is underestimated in magnitude by a factor of almost $\sim$2. This fits within the commonly observed pattern of GCMs tending to produce an early onset and reduced amplitude of precipitation in the diurnal cycle.

Like in MONC, cloud fractions in CoMorph show a vertically bimodal distribution, with the two peaks corresponding to shallow and deep convective clouds. However, the peak in shallow cloud fraction is delayed by a few hours and slightly overestimated (consistent with the shallow mass flux). The deep convective cloud fraction is more well-behaved, with a peak occurring after 5 hours as in MONC. The cloud fraction peak in the upper troposphere is also larger than in MONC by a factor of $\sim$2. Overall, performance by the CoMorph scheme in terms of reproducing the correct convective behaviour worsens as model resolution decreases, that is, the 4 km simulation performs the closest to the "truth" out of all three simulations. The 4 km simulation gives us the least bias in magnitudes of deep convective mass flux and cloud fraction.

2.3.4 Ensemble Mean Convective Properties

In Section 2.3.3, we considered convective properties over a single forcing cycle for MONC and CoMorph. We now evaluate ensemble mean cloud-base mass flux and cloud-base cloud fraction over several forcing cycles for MONC and CoMorph and compare the simulated behaviour.

The composite time series of cloud-base mass flux for MONC and CoMorph simulations are shown in Figure 12. Cloud base is taken to be the lowest height at which the cloud liquid mixing ratio exceeds 10^{-5} kg kg^{-1} and is approximately at 1.5 km in both MONC and CoMorph simulations. Compared to MONC, CoMorph simulations at 4 and 10 km tend to overestimate the magnitude of mass flux throughout the diurnal cycle, and produce convective activity until later

in the day (at hours 14–16 instead of hour 12). CoMorph simulations at 50 km underestimate cloud-base mass flux throughout the day. Overall, CoMorph simulations fail to produce a realistic evolution of convective mass flux within the diurnal cycle when compared with MONC. The composite time series of cloud-base cloud fraction is also shown in Figure 12. It is clear that larger grid box sizes ($\geq$ 10 km) tend to produce heavier than normal cloud fractions throughout the diurnal cycle. The evolution of cloud fraction in the 4 km simulations with CoMorph most closely matches the cloud fraction in MONC, but has an earlier onset and decay. The deficiencies in mass flux and cloud fraction behaviour are most likely due to various limitations in the design of the CoMorph parameterization scheme. Section 2.3.5 will attempt to investigate whether improvements in the features of the simulated diurnal cycle are possible by retuning select parameters within the scheme.

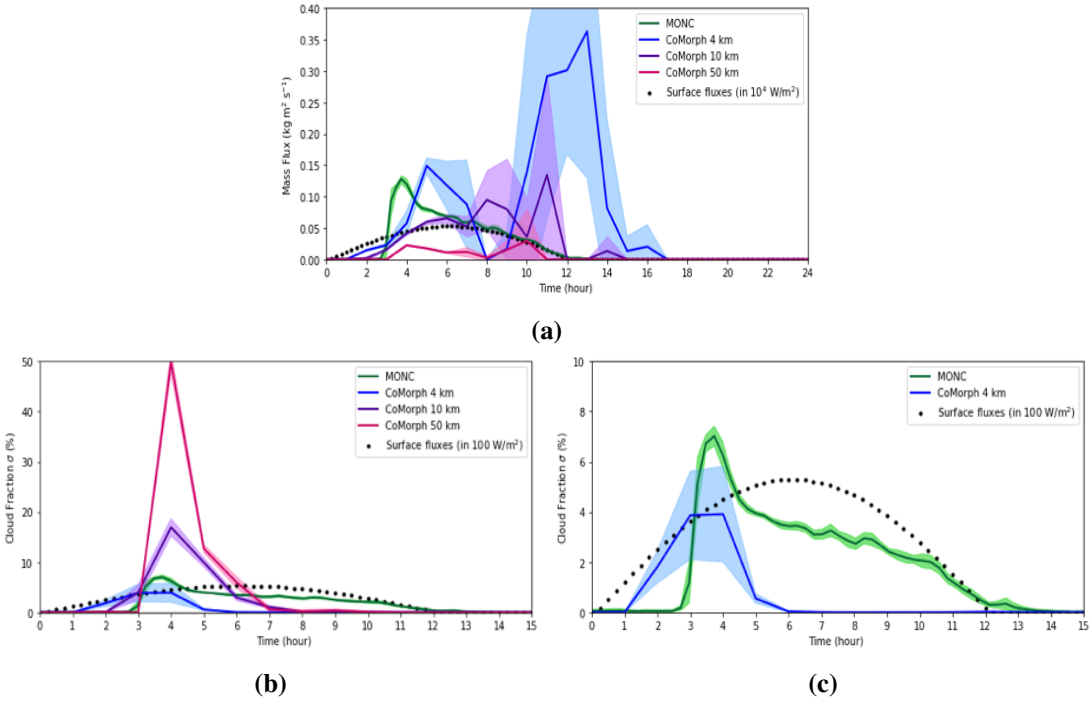

Figure 12: a. The ensemble mean time series of "ACu" cloud-base mass flux (in kg m^{-2} s^{-1}) is shown for MONC and CoMorph (4, 10, 50 km) simulations. Ensemble mean and standard deviation values are shown by thick lines and shaded areas respectively. Scaled values of the surface fluxes are also shown. b. The ensemble mean time series of "ACu" cloud-base cloud fraction (in %) is shown for MONC and CoMorph simulations. c. A zoomed in version of b. to show the evolution of cloud fraction in MONC and CoMorph (4 km).

2.3.5 Memory Properties

Following Daleu et al. (2020), we use Equation (2) to define and quantify memory on the basis of the conditional probability of occurrence of present convection given the probability of occurrence of past convection, with a functional dependence on the time t_0 after triggering, the

time lag Δt between present and past convection, and the spatial area A under consideration. Equation (2) is reproduced below for reference.

$$\mathbf{M}(A, t_0, \Delta t) = P[R(A, t_0) \cap R(A, t_0 - \Delta t)] - P^2[R(A, t_0, \Delta t)]$$

Here, $\mathbf{M}$ represents the magnitude of convective memory from within the diurnal cycle which influences a given area at a given time. The variable representing convective activity and memory is chosen to be the two-dimensional surface precipitation field, as in Daleu et al. (2020). $\mathbf{M}$ is given by the difference of two probability terms, where the first term represents the probability of rainfall occurring simultaneously over an area A at both the present time t_0 and a previous time $t_0 - \Delta t$, and the second term is the probability of simultaneous rain at the two times if they were completely random, independent events.

To satisfy the probability condition, rain is said to occur over an area if the mean precipitation over the area is greater than 0.1 mm hr^{-1} (though we also test other rain threshold values in the course of our analysis). To test the spatial dependence of memory, the ensemble mean probabilities of rain and the memory functions are evaluated using the instantaneous surface precipitation fields averaged onto various coarse grids of areas A equal to or larger than the grid-scale. The dependence of memory on time scale is examined using different values of time t_0 after the triggering. We evaluate memory functions over different areas and at different times for MONC simulations and UM simulations with both CoMorph and the 6A convection schemes.

For statistically significant results, the probability and memory functions are calculated for each forcing cycle and the ensemble mean is taken. Also, since the different simulations show precipitation time series which are out of phase with each other (as seen in Figure 9), the various UM precipitation cycles are phase-shifted so that their triggering time is aligned with that of the MONC simulation; this ensures that memory from equivalent phases in the different convective cycles are being compared.

Figure 13 shows probability and memory functions for MONC simulations. The probability of rain follows a similar distribution in time as the domain-mean precipitation (shown in Figure 9), with the probability of rain occurrence increasing sharply after triggering and decreasing gradually to zero when precipitation stops at 12 hours. The maximum probability occurs earlier and lasts longer for increasing spatial area, due to the presence of more numerous and frequent rain events over a larger domain.

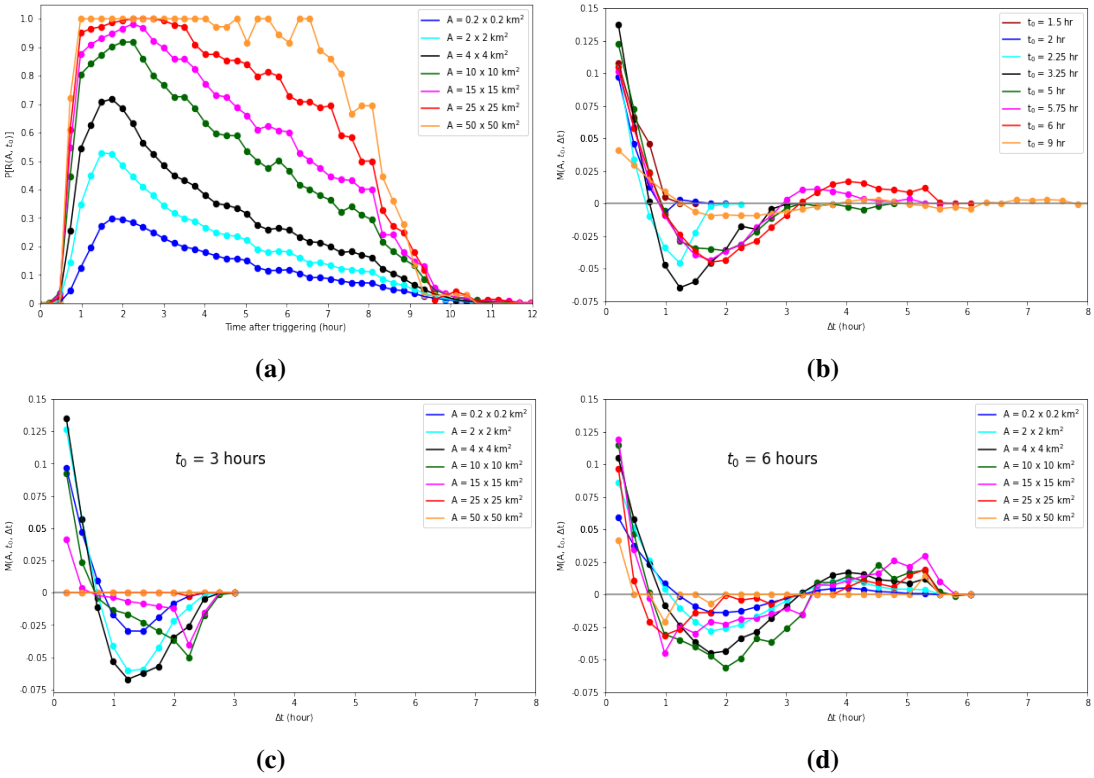

Figure 13: a. Probabilities of finding rain (P[R(A, t_0)]) for different areas in the MONC control simulations. The time axis is shifted such that time equals zero corresponds to the time of triggering. b. Memory functions (**M**(A, t_0, Δt)) for A = 4x4 km^2 for different times t_0 = 1.5, 2, 2.25, 3.25, 5, 6, and 9 hours after triggering. Memory functions for different areas are shown for (c.) t_0 = 3 hours and (d.) 6 hours after triggering.

As explained by Daleu et al. (2020), memory functions for MONC convection exhibit three-phased behaviour. The first phase shows positive memory decreasing to zero over time and lasts for about an hour. It indicates the persistence of current convection, which increases the probability of convection occurring within an hour after first developing (relative to no memory). The second phase, which lasts from 1–3 hours, shows negative memory decreasing to a minimum value and increasing to zero again. It indicates a relative suppression of convection in areas that were previously raining for the first one hour. The third and final phase lasts from 3–5 hours and shows memory increasing from zero, reaching a small positive value and plateauing to zero again at the end. It indicates a secondary enhancement of convection in areas that were less likely to rain between 1–3 hours. As described in Section 1.2.1, memory in MONC is strongest at scales of 4–10 km and is negligible for areas of 25 x 25 km^2 and greater. This is seen in the changing magnitudes of the maxima and minima in each memory phase as a different spatial area is considered (Figure 13c.-d.).

Memory was also evaluated for different conditional thresholds of precipitation to examine

the sensitivity to the threshold value (see Figure 14). Everywhere, memory was found to be larger for greater thresholds, implying reduced suppression and greater enhancement of precipitation when the mean precipitation is higher. The enhancement phase began earlier for stronger precipitation thresholds, and the suppression phase was absent for large enough thresholds.

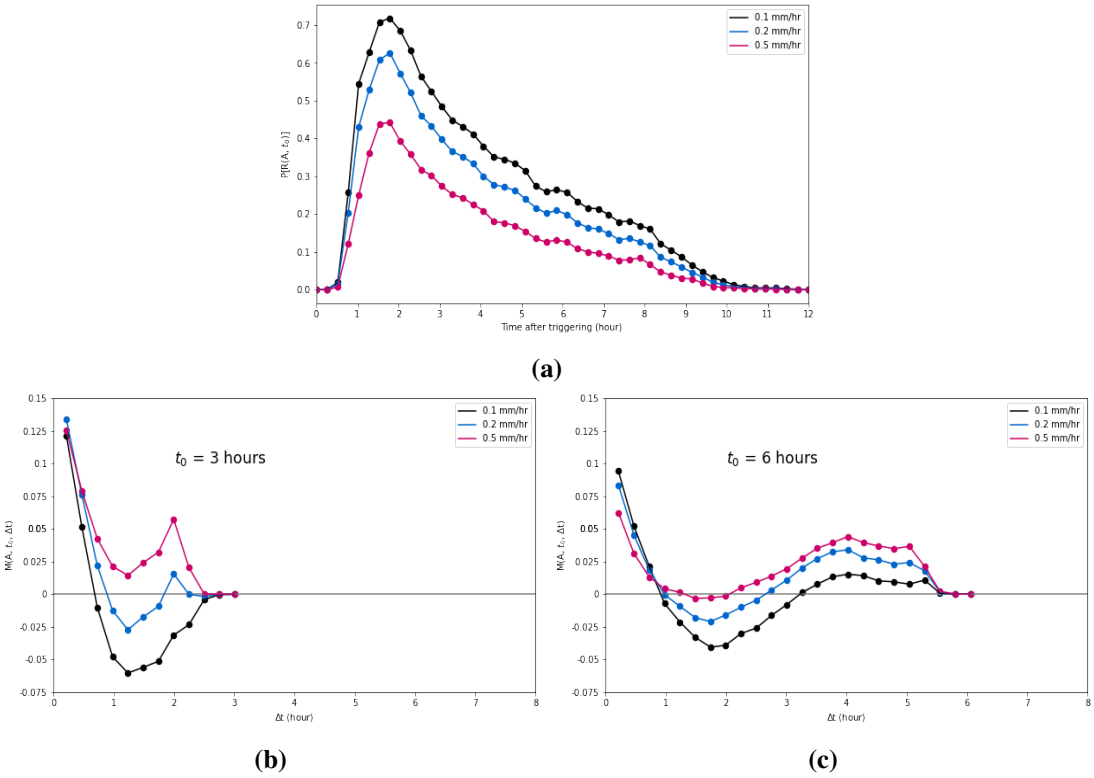

Figure 14: Top: Probabilities of finding rain (P[R(A, t_0)]) for A = 4x4 km^2 for different rain thresholds of 0.1, 0.2 and 0.5 mm hr^{-1} in the MONC control simulations. The time axis is shifted such that time equals zero corresponds to the time of triggering. Bottom: Memory functions (**M**(A, t_0, Δt)) for A = 4x4 km^2 for different rain thresholds for for t_0 = 3 (left) and 6 (right) hours after triggering.

Memory properties were then examined for CoMorph simulations performed with three different horizontal resolutions—4 km, 10 km, and 50 km—while keeping the domain area constant at 800 x 800 km^2. Probability functions for CoMorph and the 6A scheme are shown in Figure 15 below. The probability cycles for CoMorph and 6A are phase-shifted to match the triggering times shown by the corresponding MONC probability curves. Due to their triggering times already being similar, most CoMorph probabilities did not have to be adjusted; however, the 6A probability cycle was shifted to a few hours later in the day to match the MONC triggering time. As in MONC, the probability curves largely follow the behaviour of their corresponding domain mean precipitation curves (shown in Figure 9). The peak value of precipitation in CoMorph increases as the grid box size increases, and the peak occurs later in the day as horizontal resolution increases.

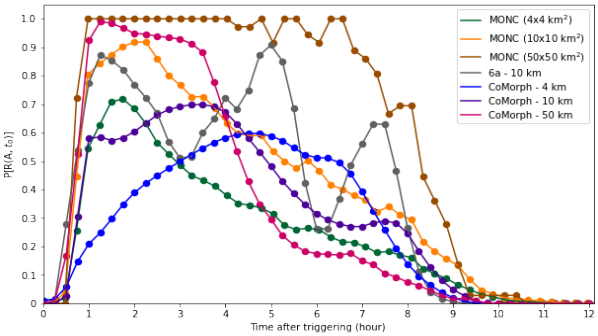

Figure 15: Probabilities of finding rain (P[R(A, t_0)]) over grid-scale area in CoMorph (4, 10, 50 km) and 6A (10 km). The time axis is shifted such that time equals zero corresponds to the time of triggering. MONC probability functions for corresponding spatial areas are shown for comparison.

Memory functions for CoMorph (4, 10, 50 km) simulations are shown in Figure 16. For CoMorph simulations with 4 km resolution, only the first phase of memory is present for convection up to t_0 = 6 hours, and it lasts for 1–6 hours after the start of convection (compared to a maximum of 1 hour duration for the MONC simulations). This first phase also has larger magnitudes of memory that those found in MONC simulations, indicating excess and prolonged memory associated with the initial persistence of convection. The second phase of suppression only sets in for convection produced from t_0 = 7 hours after triggering (compared to t_0 = 2.25 hours for MONC). From t_0 = 7 hours, the first phase is shortened to 1–2 hours in duration and the second phase lasts at least 6 hours, suppressing rain in regions which were raining in the first 1–2 hours. The third phase is absent altogether, and all memory becomes negligible after t_0 = 9 hours after triggering. With coarse-grained averaging beyond 4 x 4 km^2, the memory function does not exhibit significant changes in magnitude or in phase (Figure 31 in the Appendix). Compared to MONC memory at the 4 km scale, CoMorph has a first phase of memory that plays a longer, more dominant role in the convective cycle and delays the onset of the second phase of memory (Figure 32 in the Appendix). The duration of the second phase in CoMorph is also approximately double that in MONC simulations, with slightly larger negative memory associated with it.

For CoMorph simulations with 10 km resolution, we again observe a stronger and prolonged first phase which lasts for 1–5 hours after the start of convection (compared to 1–2 hours in the MONC simulations) and is the only phase of memory present up to t_0 = 5 hours. The second phase is present for convection starting from t_0 = 5.75 hours after triggering (compared to 3.25 hours for MONC)). At all the times when the second phase is present, the first phase lasts for 1–3 hours in duration and the second phase lasts for 2-7 hours, suppressing rain in regions raining for the first few hours. Again, the third phase is absent for convection at all times and memory effects disappear after t_0 = 9 hours. With coarse-grained averaging beyond 10 x 10 km^2, the

magnitude of memory in the first phase decreases significantly as spatial area increases (Figure 33 in the Appendix). The second phase of memory disappears for areas 20 x 20 km^2 and larger, leaving only the first phase of persistence of convection. Compared to MONC memory at the 10 km scale, the first phase in CoMorph 10 km lasts longer and delays the second phase. The duration of the second phase is also on average longer than in the MONC simulations (Figure 34 in the Appendix).

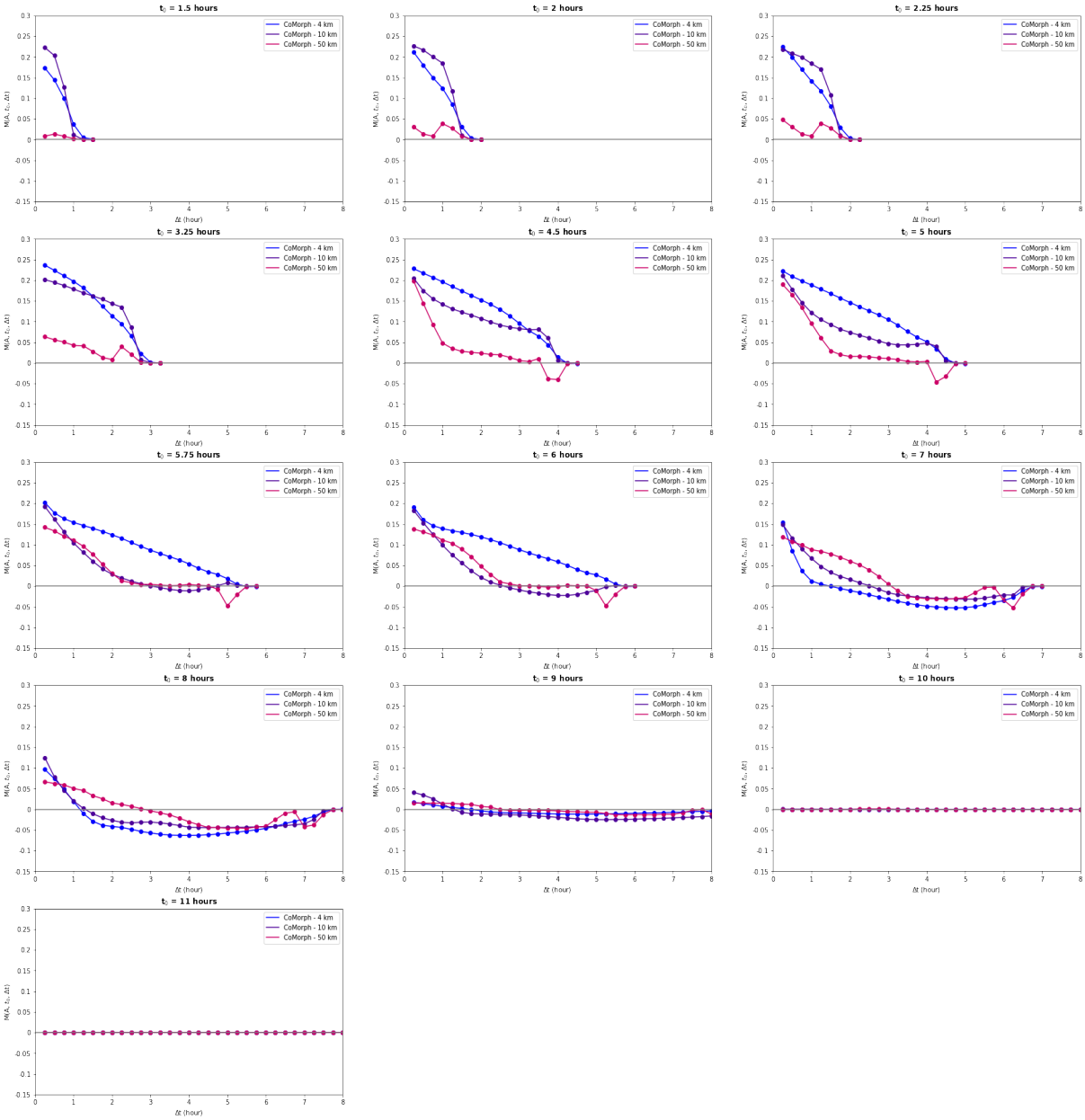

Figure 16: Memory functions (**M**(A, t_0, Δt)) for the UM CoMorph simulations for spatial areas of A = 4x4 km^2 (in blue), 10x10 km^2 (in purple), and 50x50 km^2 (in pink) for different times t_0 = 1.2, 2, 2.25, 3.25, 4.5, 5, 5.75, 6, 7, 8, 9, 10 and 11 hours after triggering.

For CoMorph simulations with 50 km resolution, the first phase of memory is weaker compared to the 4 km and 10 km resolution for convection produced in the initial hours after triggering. Persistence memory becomes considerable from t_0 = 4.5 hours and decreases again for convection produced at t_0 = 9 hours. The second phase sets in for convection produced from t_0 = 7 hours, and lasts about 3–4 hours in duration. As before, the third phase is absent. The MONC simulations show virtually zero memory for all times at scales of 50 km. Hence, CoMorph shows excess first phase (positive) and second phase (negative) memory at the 50 km scale (Figure 36 in the Appendix).

For all CoMorph simulations, memory disappears after t_0 = 9 hours as in the MONC simulations. The sensitivity of CoMorph memory to precipitation thresholds was also examined and was observed to be negligible for all three resolutions (see Figure 31, Figure 33, and Figure 35 in the Appendix).

Figure 17 shows the difference in memory between CoMorph and MONC simulations for each of the three resolutions at different times t_0 after triggering. It is clear that excess positive first phase memory persists well after the start of convection, and excess negative memory prevails in the later hours due to a delayed suppression phase in place of a secondary enhancement phase. On average, the 4 km simulations appears to have greater magnitudes of memory than the 10 and 50 km simulations, especially in the first phase.

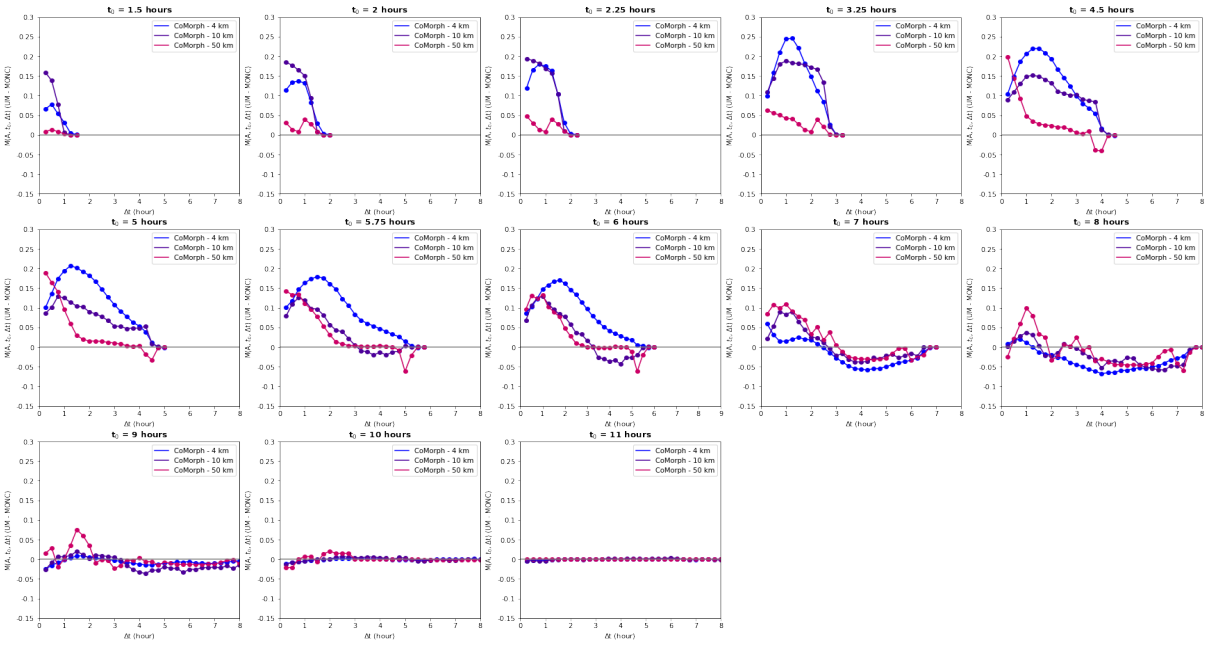

Figure 17: Differences in the memory functions (**M**(A, t_0, Δt)) of UM CoMorph and MONC simulations for spatial areas of A = 4x4 km^2 (in blue), 10x10 km^2 (in purple), and 50x50 km^2 (in pink) for different times t_0 = 1.2, 2, 2.25, 3.25, 4.5, 5, 5.75, 6, 7, 8, 9, 10 and 11 hours after triggering.

Finally, memory properties were examined for UM simulations using the 6A convection scheme with a single horizontal resolution of 10 km. The 6A scheme exhibits almost zero memory throughout the diurnal convective cycle, as shown in Figure 18. Memory also remains negligible regardless of the precipitation threshold and spatial area (Figure 37 in the Appendix).

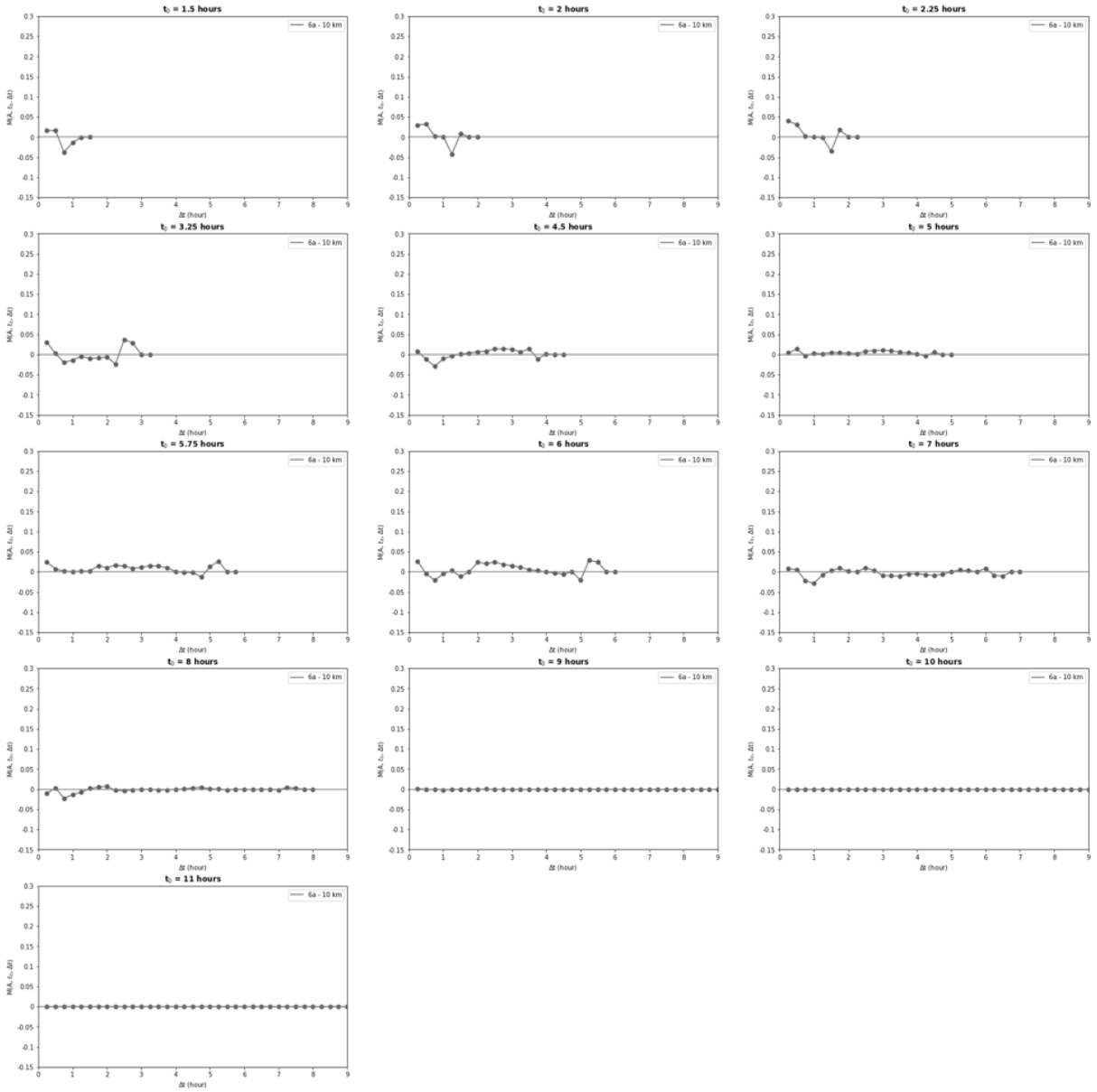

Figure 18: Memory functions (**M**(A, t_0, Δt)) for the UM 6A simulation for spatial area A = 10x10 km^2 (in grey) for different times t_0 = 1.2, 2, 2.25, 3.25, 4.5, 5, 5.75, 6, 7, 8, 9, 10 and 11 hours after triggering.

Hence, the CoMorph parameterization scheme shows a strong improvement over the 6A scheme not only in terms of simulating the diurnal cycle of precipitation (as we saw in Section 2.3.2), but also in accounting for the effects of convective memory within the diurnal cycle. However, the CoMorph scheme is far from perfect, as it captures the incorrect magnitude and timing of memory at all three horizontal resolutions adopted. The very first step in diagnosing how to

improve the memory properties produced by CoMorph might be to try to improve the accuracy and behaviour of the simulated diurnal cycle. That is what we attempt to do in Section 2.3.7. Before that, in the next section, we examine and compare the behaviour of spatial thermodynamic variability arising from convection in each of our simulations.

2.3.6 Spatial Thermodynamic Variability

Section 1.2.2 emphasized the significant role of low-level spatial thermodynamic variability in generating convective memory in the atmosphere and influencing future convection. Bearing this in mind, one possible physical explanation for the considerable differences in memory properties in our different simulations could be discrepancies in the magnitude and/or behaviour of small-scale thermodynamic variability generated by the corresponding diurnal cycles. In order to better understand memory mechanisms in our models, we evaluate the magnitudes and spatial distribution of variability in potential temperature (θ) and moisture (q_v) in the MONC and CoMorph simulations. Thermodynamic variability refers to deviations or anomalies in the potential temperature and specific humidity values at each grid point with respect to the domain mean values. A positive (negative) θ anomaly implies warmer (colder) than average air temperature, and a positive (negative) q_v anomaly implies moister (drier) than average humidity content in the air. We investigate the spatial pattern of variability in both the horizontal and vertical directions in our 3D simulations. Figure 19 shows the thermodynamic fields generated in MONC by the end of the third diurnal cycle, therefore comprising the initial conditions for the fourth diurnal cycle.

As Daleu et al. (2020) assert, thermodynamic and moisture anomalies tend to be negatively correlated with each other in the lower troposphere. Anomalously warm air possesses a relatively lower humidity content than average, while anomalously cool air possesses a higher humidity content than average. This is expected given that the saturated vapour pressure of water vapour increases as temperature increases, favouring the process of evaporation and increasing the saturation capacity of air. It is evident from Figure 19 that moisture fluctuations are more prominent at a height of 1 km than at 3 km, and reduce greatly above 4 km. Potential temperature fluctuations, on the other hand, do not show a significant change in magnitude with height within the troposphere.

In order to examine thermodynamic variability on scales of $\sim$5–20 km in our CoMorph simulations, we consider the potential temperature and water vapour anomalies within a 100 x 100 km^2 subset in the interior of our 800 x 800 km^2 UM domain. This enables us to compare spatial distributions on equivalent domains in the MONC and CoMorph simulations. Thermodynamic

variability is also examined on the large-scale for the entire UM domain and the cross sections for each CoMorph case (4, 10, 50 km) are shown in the appendix (Figures 38 to 40).

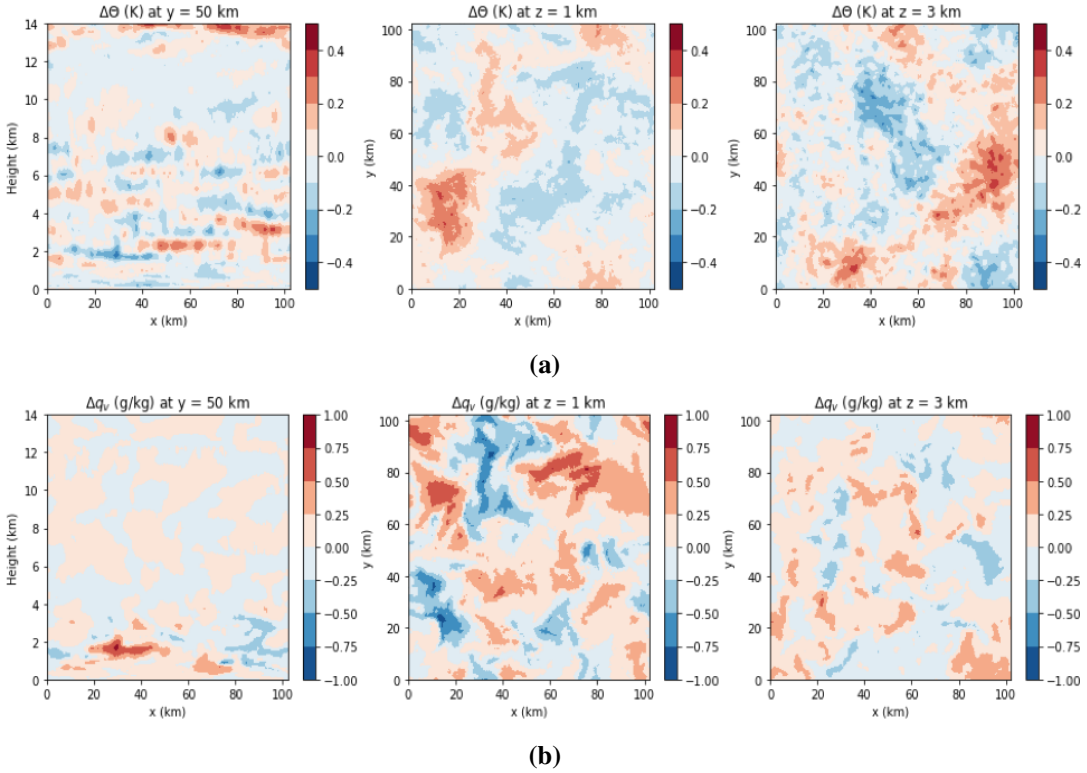

Figure 19: a. Vertical cross section at $y = 50$ km (left) and horizontal cross sections at heights of $z = 1$ km (centre) and $z = 3$ km (right) of potential temperature anomalies with respect to the domain mean at the end of the third diurnal cycle in the MONC simulation. b. Vertical cross section at $y = 50$ km (left) and horizontal cross sections at heights of $z = 1$ km (centre) and $z = 3$ km (right) of water vapour anomalies with respect to the domain mean at the end of the third diurnal cycle in the MONC simulation.

Figure 20 shows the thermodynamic fluctuations at the start of the second forcing cycle in the CoMorph 4 km simulation. CoMorph does not capture the small-scale variability to the same detail as MONC does, and produces larger (>10 km), more homogeneous patterns of anomalies. The anti-correlation between moisture and temperature in the lower troposphere is not as discernible and sharply defined as in MONC's thermodynamic fields. Figure 21 and Figure 22 show the thermodynamic fluctuations for CoMorph 10 and 50 km simulations respectively. In general, as resolution decreases, the size and homogeneity of the anomalous regions increase and the average magnitudes of the thermodynamic perturbations decrease. There is virtually no evidence of any anti-correlation between moisture and temperature at 10 km and 50 km resolutions. Overall, convection simulated by the CoMorph scheme fails to generate sufficient thermodynamic variability to influence future convection in the manner predicted by MONC. The reasons for this behaviour most likely lie in the assumptions used by the parameterization scheme in its large-scale treatment of cloud ensembles.

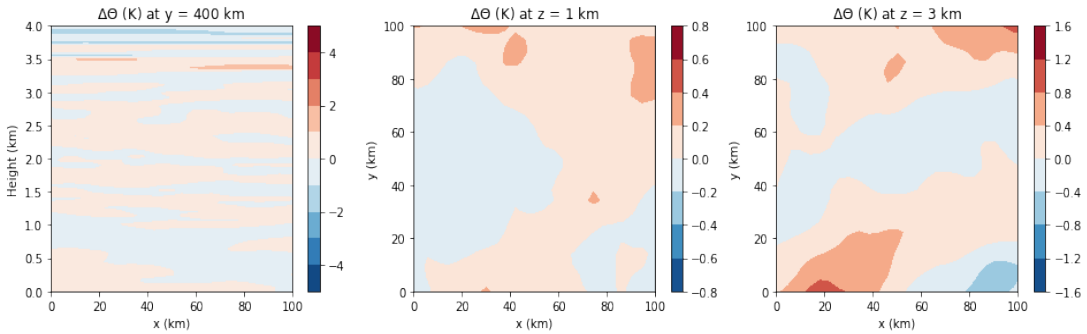

(a)

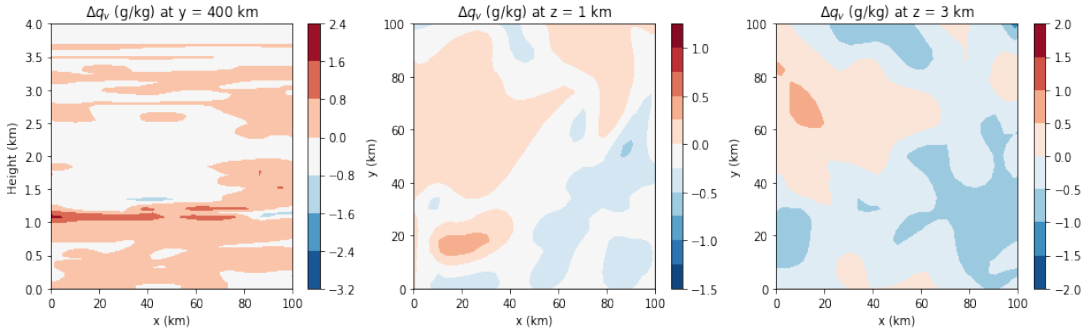

(b)

Figure 20: a. Vertical cross section at $y = 50$ km (left) and horizontal cross sections at heights of $z = 1$ km (centre) and $z = 3$ km (right) of potential temperature anomalies with respect to the domain mean at the end of the first (or sixth, as in Figure 7) diurnal cycle in the CoMorph 4 km simulation. b. Vertical cross section at $y = 50$ km (left) and horizontal cross sections at heights of $z = 1$ km (centre) and $z = 3$ km (right) of water vapour anomalies with respect to the domain mean at the end of the first diurnal cycle in the CoMorph 4 km simulation. Note that the contour intervals differ from those in Figure 19 for MONC, but remain consistent across all UM simulations.

In Section 2.3.1, we surmised that the CoMorph and 6A schemes might be generating a long-term convective memory which may be responsible for the differences in behaviour between successive diurnal cycles. In order to gain insight into the possible reason for this memory, we examined convectively generated thermodynamic variability from the initial few days (days 1–5) for all CoMorph simulations and compared our results with days 6–9 in the second half of each simulation. No significant differences were observed in the magnitudes and patterns of spatial variability from one day to another (not shown). As a result, the source of the long-term memory in the parameterization scheme remains unclear. Performing considerably longer simulations with CoMorph and analyzing the thermodynamic fluctuations from different days within the simulation might throw light on whether this memory continues to persist indefinitely, or if not, on how long it lasts and how it might affect the generation of short-term convective memory in the atmosphere. Modifying scheme parameters and studying the resulting convective response would also throw insight on any other possible reasons, whether physical or unphysical, for the unexpected cycle-to-cycle variability in CoMorph and 6A simulations.

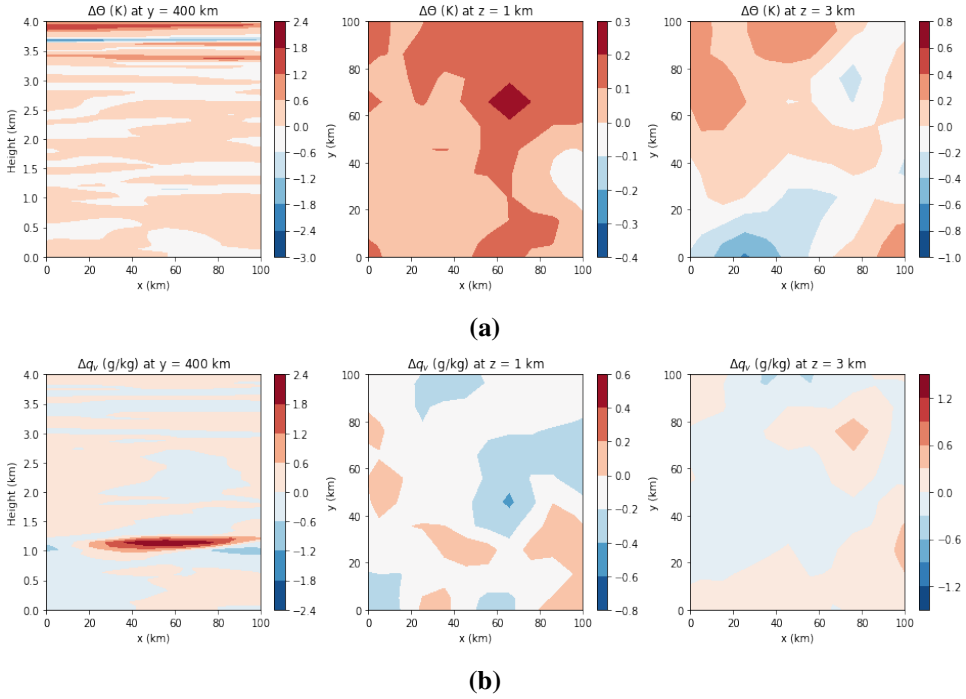

Figure 21: Same as in Figure 20 but for the CoMorph 10 km simulation.

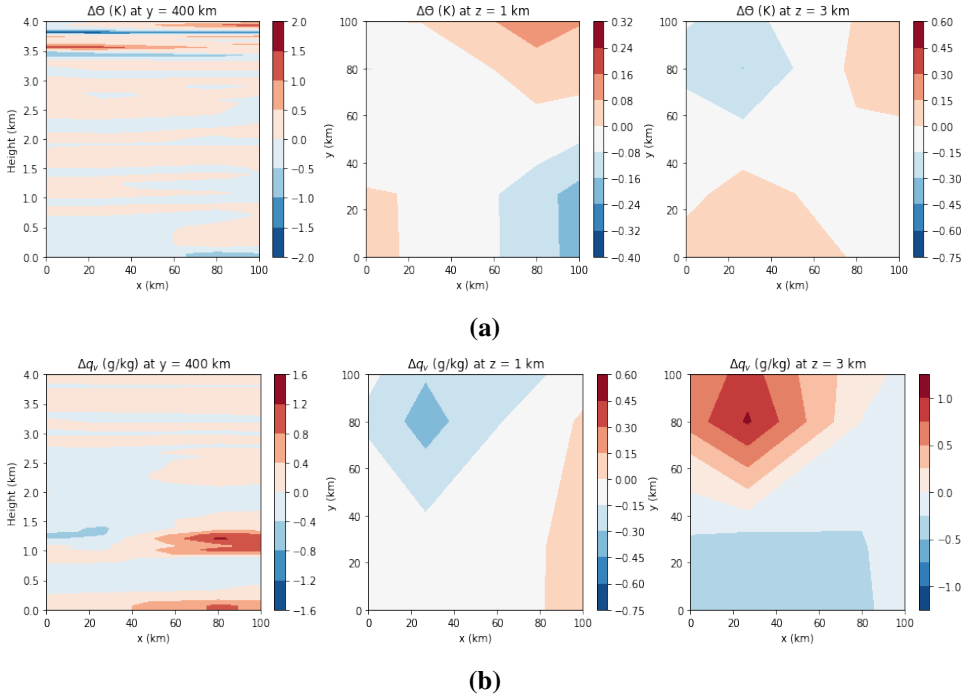

Figure 22: Same as in Figure 20 and Figure 21 but for the CoMorph 50 km simulation.

2.3.7 Improvement of CoMorph Memory

As we saw in Section 1.2.2, the control settings of CoMorph do not perfectly simulate the diurnal cycle. While CoMorph is a significant improvement over the 6A scheme, biases persist in the magnitudes of the daily mean and peak precipitations, as well as in the qualitative shape of the simulated precipitation cycle itself.

At 4 km resolution, the peak in precipitation is not sharply defined and precipitation declines more gradually compared to the MONC simulation. The behaviour of memory in CoMorph also shows discrepancies in magnitude and phase compared to the memory in MONC. As part of development testing, several CoMorph parameters were varied in an attempt to improve the memory properties of the diurnal cycle with respect to the control run at 4 km. From these, we consider two additional simulation cases with modified settings at 4 km resolution, referred to as Case 2 and Case 3.

Case 2 includes corrections to avoid a spurious increase in parcel moisture perturbation at low relative humidity and the double-counting of turbulence-based parcel perturbations within liquid-cloud. Additionally, the magnitude of turbulence-based parcel perturbations is reduced from 66.7% to 33.3% and convection is not allowed to trigger from overshooting of forced cumuli. Case 3 involves an amplification factor that has been applied only to parcels triggering liquid-cloud. Case 2 and Case 3 are chosen for analysis because they were seen to produce better results in simulating the diurnal cycle.

Figure 23 shows the last nine successive diurnal cycles simulated by CoMorph Case 2 and Case 3 runs. MONC and CoMorph 4 km control cycles are also shown for comparison. As in the other CoMorph simulations, we observe significantly earlier onset and day-to-day fluctuations in the amplitude of precipitation in the first five days of the simulation. In order to evaluate statistically steady convective and memory properties, we consider only the consistent, steady cycles (days 6–9) of the Case 2 and Case 3 simulations in our analysis. The four successive diurnal cycles considered are shown in Figure 24.

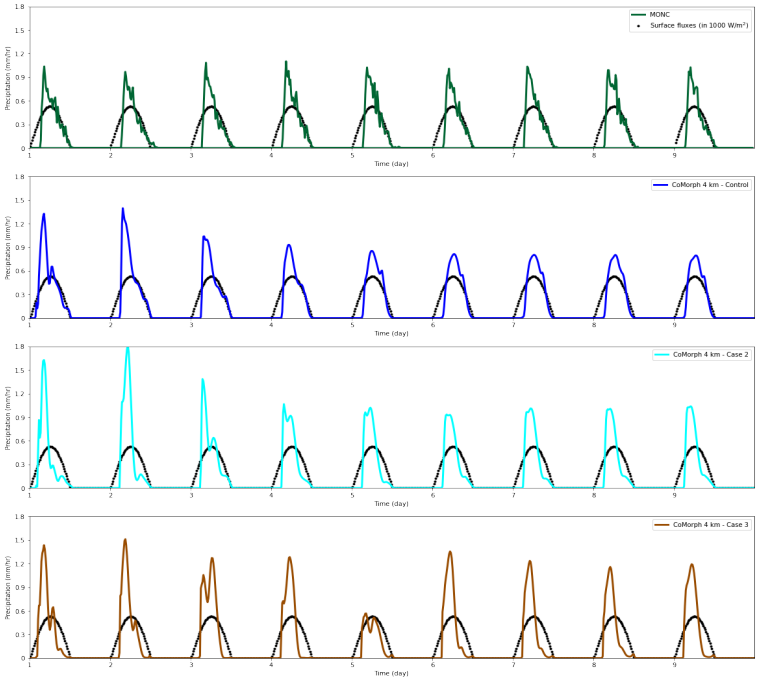

Figure 23: Surface precipitation (in mm hr^{-1}) is shown for the last nine successive diurnal cycles of the CoMorph 4 km Control (second panel, in blue), Case 2 (third panel, in cyan), and Case 3 (fourth panel, in brown) simulations. MONC precipitation cycles are shown in the top panel (in green) for comparison. The total surface fluxes, that is, the sum of the latent and sensible heat fluxes, are also shown (in W m^{-2}, scaled by factor of 1000).

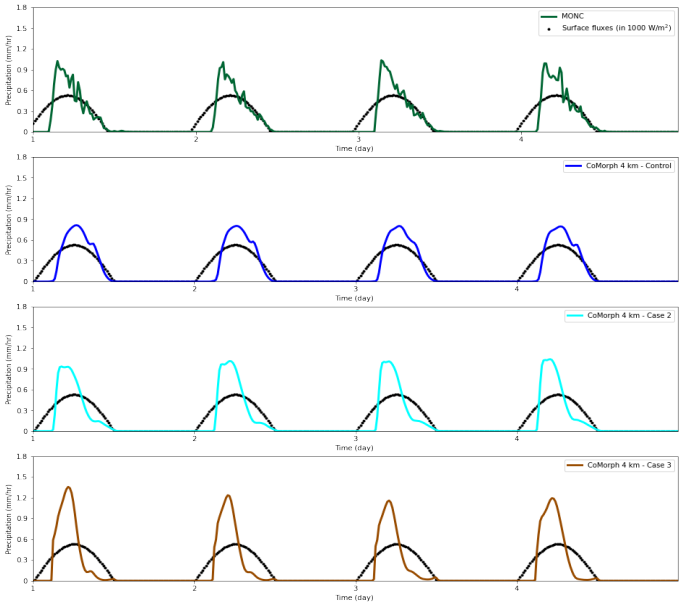

Figure 24: Surface precipitation (in mm hr^{-1}) is shown for four successive, steady diurnal cycles of the CoMorph 4 km Control (second panel, in blue), Case 2 (third panel, in cyan), and Case 3 (fourth panel, in brown) simulations. MONC precipitation cycles are shown in the top panel (in green) for comparison. The total surface fluxes, that is, the sum of the latent and sensible heat fluxes, are also shown (in W m^{-2}, scaled by factor of 1000).

The composite time series of precipitation for CoMorph 4 km Control, Case 2 and Case 3 simulations are shown in Figure 25. While the control simulation has a triggering time very similar to MONC at ∼2.75 hours, Cases 2 and 3 show an earlier onset of convection at 2–2.25 hours. However, Cases 2 and 3 show a noticeable improvement over the control run in the shape of their precipitation cycle—the steep increase and peak in precipitation become more well-defined. Despite this improvement, both cases underestimate the domain mean daily mean precipitation rate compared to that of MONC by about 10–15%. This is likely due to the sharper and earlier decline in precipitation relative to what is seen in MONC.

Probability functions for Case 2 and Case 3 are shown in Figure 26 below. It is clear that both cases are able to reproduce the sharp increase in precipitation right after triggering. However, the distribution of rain remains inaccurate; too much rain occurs in the first six hours of the day and too little rain occurs after noon.

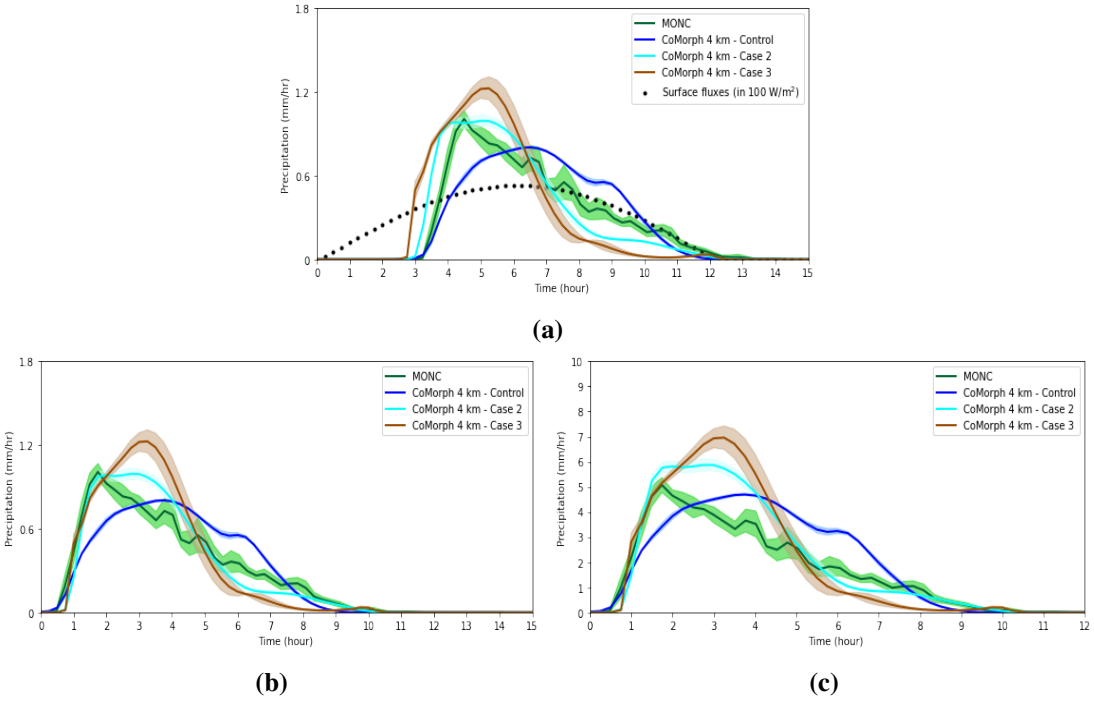

Figure 25: a. Composite time series of precipitation for MONC (in green), CoMorph 4 km Control (in blue), CoMorph 4 km Case 2 (in cyan), CoMorph 4 km Case 3 (in brown) simulations. Ensemble mean and standard deviation values are shown by thick lines and shaded areas respectively. The surface forcing time series (sum of sensible and latent heat fluxes) is also shown in W m^{-2}, scaled by a factor of 10^3. b. Same as in a. but the time axis is shifted such that time equals zero corresponds to the time of triggering in all simulations. c. Same as in b. but the normalized precipitation time series (instantaneous precipitation divided by the domain mean daily mean precipitation) is shown instead.

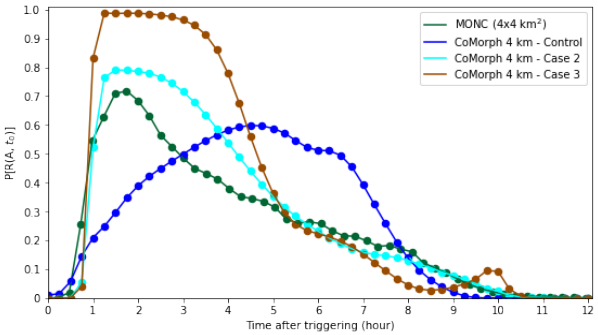

Figure 26: Probabilities of finding rain (P[R(A, t_0)]), using a minimum rain threshold of 0.1 mm hr^{-1}, over A=4x4 km^2 in CoMorph 4 km Control (in blue), Case 2 (in cyan), and Case 3 (in brown) simulations. The time axis is shifted such that time equals zero corresponds to the time of triggering. The MONC probability function for A=4x4 km^2 is shown (in green) for comparison.

Memory functions for the Control, Case 2, and Case 3 simulations are shown in Figure 27. Case 2 captures only the first phase of memory until t_0 = 6 hours after triggering, and the first phase lasts for 1–6 hours like in the control case. The second phase of memory is present for convection starting from t_0 = 7 hours, again as in the control. When the second phase is present, the first phase lasts for ∼1–1.5 hours and the second phase lasts for 4–6 hours. The third phase is absent as it was in all CoMorph simulations so far. Case 2 shows some improvement over the control in reducing the magnitude of excess positive memory associated with developing convection in the first phase and in reducing the excess negative memory associated with suppression of rain in the second phase. Case 2 also slightly reduces the (excess) duration of the second phase which was present in the control.

Case 3 possesses negligible memory in the first phase until t_0 = 4.5 hours and the first phase is the only active phase of memory for convection until t_0 = 5 hours. The second phase sets in for convection starting at t_0 = 5.75 hours, a little more than an hour earlier than in Case 2 and the control. When the second phase is present, the first phase lasts for 1–2 hours and the second phase lasts for 2–3 hours. The third phase is absent and all memory effects disappear after t_0 = 9 hours. Case 3 performs worse than Case 2 and the control when it comes to reproducing the first phase of memory in the initial hours of convection, but shows an improvement by reducing the delay in the onset of the second phase of memory. The magnitude and duration of the second phase in Case 3 also resemble that of MONC more than the control and Case 2.

As we did in Section 2.3.6, we examine spatial thermodynamic variability in Case 2 and Case 3, which are shown in Figure 28 and Figure 29 respectively. The potential temperature and water vapour anomalies show no significant differences in magnitude and in distribution relative to those in the control simulation (Figure 20). As before, small-scale thermodynamic structures

are unresolved by the CoMorph scheme at 4 km horizontal resolution even after the modification in parameters, and this could contribute to the bias in memory effects relative to the MONC simulation.

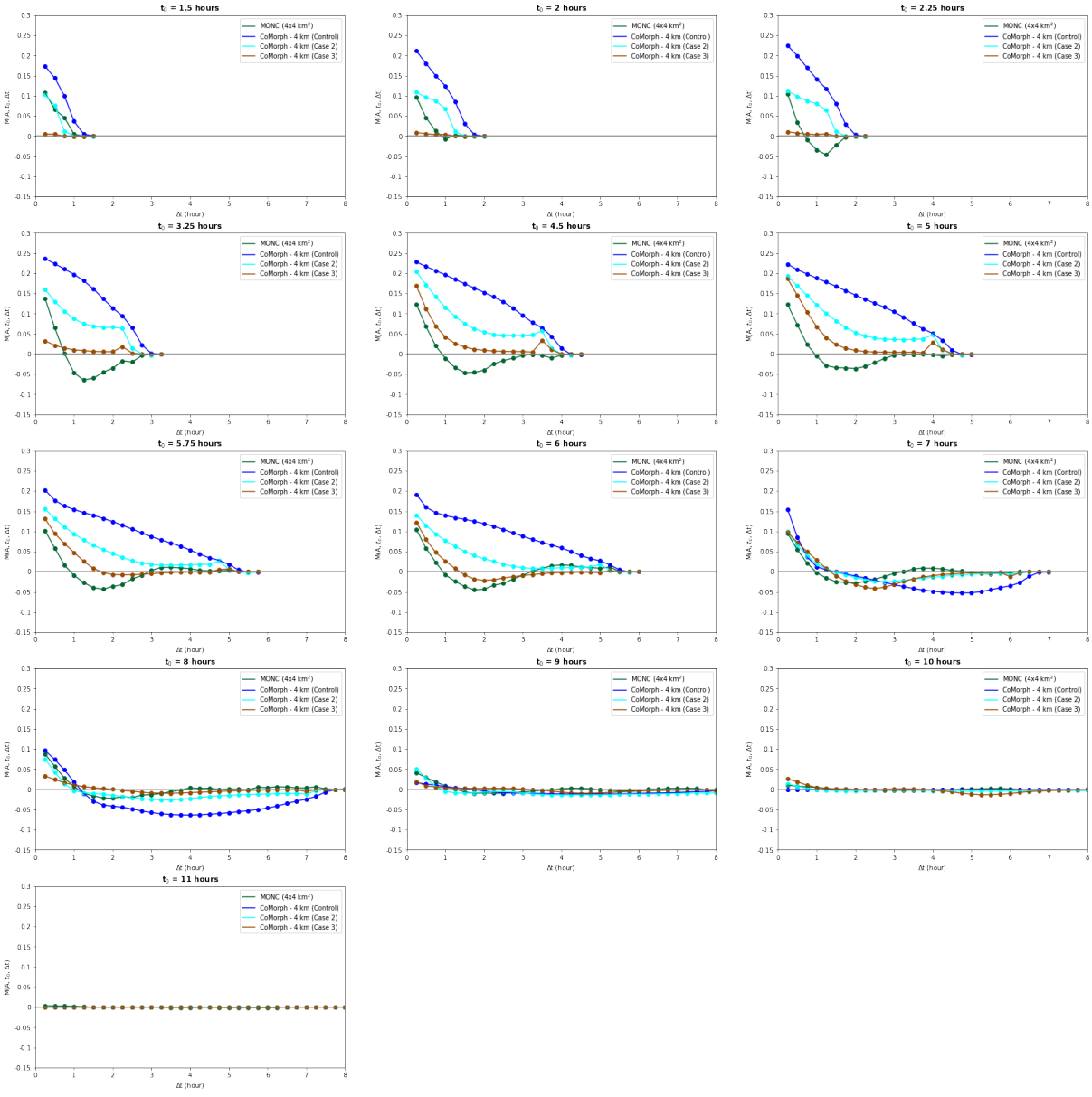

Figure 27: Memory functions (**M**(A, t_0, Δt)) for A = 4x4 km^2 for CoMorph 4 km Control (in blue), Case 2 (in cyan), and Case 3 (in brown) simulations for different times t_0 = 1.2, 2, 2.25, 3.25, 4.5, 5, 5.75, 6, 7, 8, 9, 10 and 11 hours after triggering. MONC memory functions for A = 4x4 km^2 are also shown (in green) for comparison.

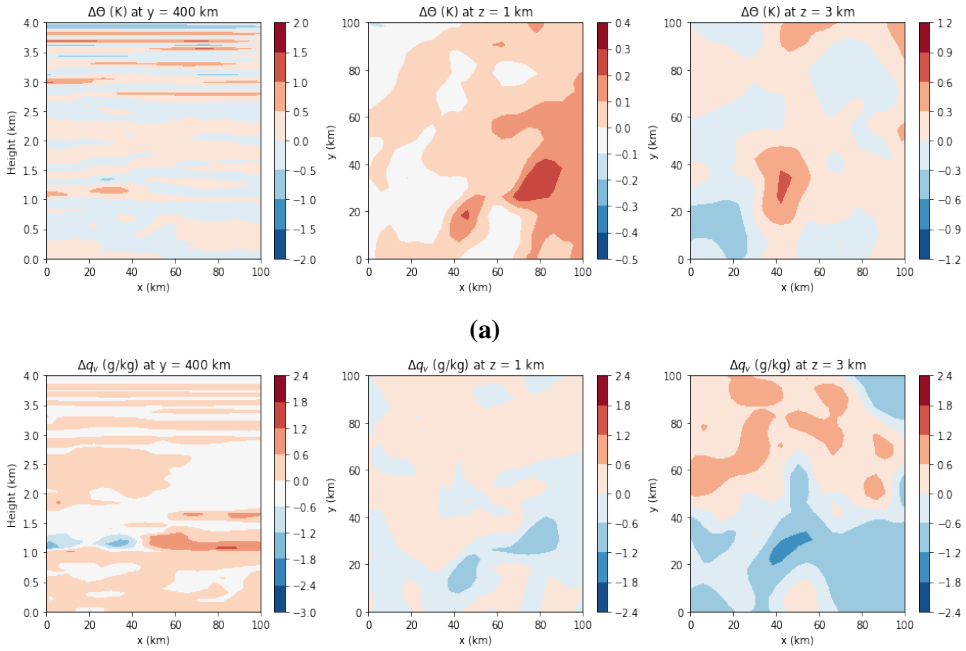

Figure 28: a. Vertical cross section at $y = 50$ km (left) and horizontal cross sections at heights of $z = 1$ km (centre) and $z = 3$ km (right) of potential temperature anomalies with respect to the domain mean at the end of the first (or sixth, as in Figure 7) diurnal cycle in the CoMorph 4 km Case 2 simulation. b. Vertical cross section at $y = 50$ km (left) and horizontal cross sections at heights of $z = 1$ km (centre) and $z = 3$ km (right) of water vapour anomalies with respect to the domain mean at the end of the first diurnal cycle in the CoMorph 4 km Case 2 simulation.

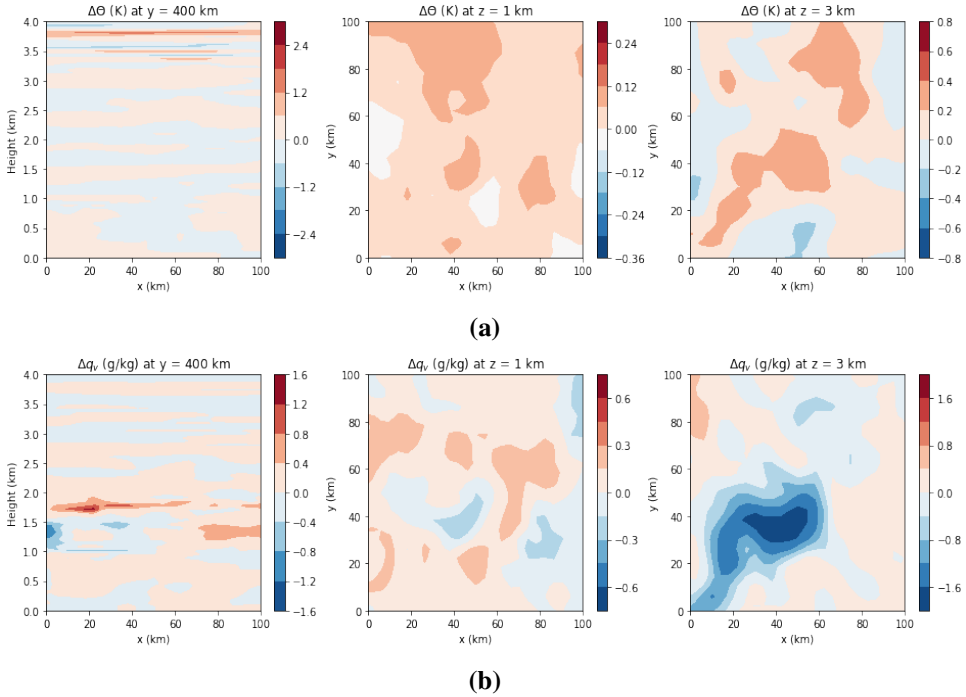

Figure 29: Same as in Figure 28 but for the CoMorph 4 km Case 3 simulation.

We also evaluate the domain-mean mass flux and cloud fraction at cloud-base for Case 2 and Case 3 over multiple forcing cycles, like we did in Section 2.3.4. Figure 30 shows the ensemble mean cloud-base mass flux and cloud fraction for Case 2 and Case 3 simulations. The behaviour of ensemble mean mass flux shows a significant improvement in Case 3 compared to the control, though there is not much improvement in Case 2. Cloud fraction, on the other hand, behaves worse in Case 2 and Case 3 compared to the control.

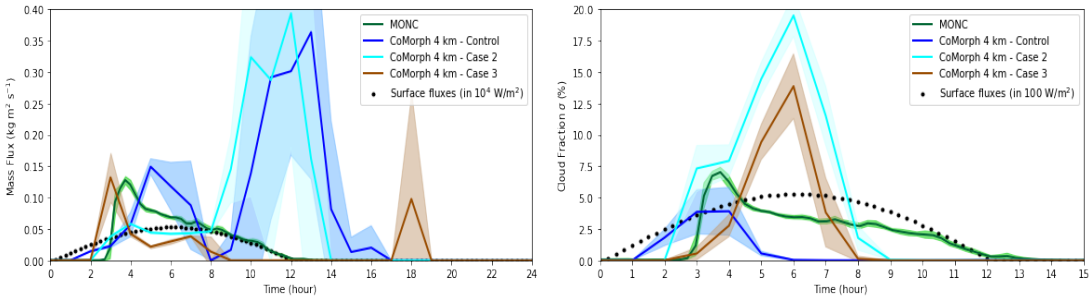

(a) **(b)**

Figure 30: a. The ensemble mean time series of "ACu" cloud-base mass flux (in kg m^{-2} s^{-1}) is shown for CoMorph 4 km Control (in blue), Case 2 (in cyan), and Case 3 (in brown) simulations. MONC mass flux (in green) is also shown for comparison. Ensemble mean and standard deviation values are shown by thick lines and shaded areas respectively. b. The ensemble mean time series of "ACu" cloud-base cloud fraction (in %) is shown for MONC and CoMorph 4 km simulations.

Our results show that modifying certain parameters within the CoMorph scheme proves beneficial in improving the behaviour of the precipitation cycle, as well as in reducing some of the excess and prolonged memory associated with the first and second phases of persistence and suppression of convection respectively. However, no all-around improvements are obtained in the simulation of thermodynamic variability on the small-scale and in the simulation of convective properties of mass flux and cloud fraction.

3. Conclusion

3.1 Summary and Discussion

We examined and compared idealized diurnal cycles of precipitation simulated by the Unified Model (UM) using two convective parameterization schemes: CoMorph and the 6A scheme. Our evaluations were based on the results of similar diurnal cycle simulations performed by MONC, a high-resolution cloud-resolving model. We made use of three different horizontal resolutions with the CoMorph scheme (4, 10, and 50 km) and one horizontal resolution (10 km) with the 6A scheme.

We found that the CoMorph scheme demonstrates a significant improvement over the 6A scheme in reproducing realistic amplitudes and more importantly, the realistic timing and shape of the domain-mean precipitation in the diurnal cycle. CoMorph eliminates the issue of multiple precipitation peaks produced by 6A and reduces the negative bias in precipitation magnitudes. Specifically, CoMorph performed best in this regard when a horizontal model resolution of 10 km was employed.

We also compared memory effects within the diurnal cycles simulated by each parameterization scheme. Here too, CoMorph shows a notable improvement over the 6A scheme. While the 6A scheme shows a complete absence of any memory effects at all time scales after the start of convection, the CoMorph scheme is able to capture memory effects at all three grid scales considered. Diurnal cycles in CoMorph show the presence of the first phase of memory associated with the persistence of developing convection and the second phase associated with the suppression of convection. However, the third phase of secondary enhancement of precipitation is completely absent at all three horizontal resolutions. Moreover, the amplitudes and timing of the first and second phases in CoMorph possess biases relative to their reference values in the MONC simulation. On average, CoMorph generates excess positive memory in the first phase of convection and prolongs the duration of the first phase. CoMorph also delays the onset of the second phase and prolongs its duration at all spatial scales.

Given CoMorph's improved memory properties relative to 6A, we investigated convective properties of domain-mean mass flux and cloud fraction arising from the CoMorph parameterization scheme. Like in MONC, CoMorph produces two peaks in mass flux and cloud fraction associated with shallow and deep convection respectively. However, CoMorph tends to delay the peak in shallow convective mass flux and overestimate its magnitude. The opposite occurs with deep convective mass flux; the peak occurs earlier and is underestimated in magnitude relative to MONC. Shallow convective cloud fraction also peaks late, and the magnitudes of shallow and

deep convective cloud fractions are both overestimated. We next considered the spatial thermodynamic fluctuations generated by the end of each diurnal cycle in the CoMorph scheme. We found that CoMorph struggles to capture small-scale anomalies in temperature and moisture and to produce a clear anticorrelation between temperature and moisture anomalies in the lower troposphere.

Finally, we attempted to retune certain parameters within CoMorph with the aim of obtaining an improved diurnal cycle and memory properties. At 4 km resolution, our modifications improve the simulation of the steep increase in precipitation after triggering and produce a sharper diurnal peak. Memory properties also show an improvement over the control in that the excess first phase memory is reduced and the delayed second phase sets in earlier.

In all simulations, both parameterization schemes produced considerable day-to-day variability in their initial convective response, indicating the existence of a long-term memory possibly arising either from the parameterization scheme or from the homogeneous initial conditions used for the simulations. Our investigation of thermodynamic variability did not reveal qualitative or quantitative differences between the initial days and the later days in each simulation. Hence, the exact cause of this long-term memory effect remains unclear and can only be diagnosed with longer simulations of 20–50 days and by modifying a range of scheme parameters.

The cycle-to-cycle fluctuations are significant at resolutions of 4 and 10 km with both schemes, and are negligible with CoMorph at a resolution of 50 km. This could suggest a possible connection of this long-term memory with grey-zone scales. Unexpected memory effects could arise at these scales due to discontinuities between parameterized and resolved convective flows, or due to the nondeterministic nature of convection given a very small cloud sample size. Further model runs need to be performed at a range of different resolutions within the grey-zone to identify the scales at which the inter-cycle memory arises and fades away. This would provide an indication of the scales over which the assumptions and/or parameters of the parameterization scheme would have to be modified to introduce stochastic elements and scale-aware behaviour that can distinguish between convective systems of different sizes and prevent double counting in the representation of convection.

3.2 Future Work

"Science never solves a problem without creating ten more."
— George Bernard Shaw

The previous section 3.1 provided a few recommendations on the way forward based on our results, and this section will expand on some specific ways in which the questions asked in this study can be extended and built upon. Several outstanding issues remain to be addressed. How can convective, thermodynamic, and memory properties simulated by CoMorph be improved? Specifically, what causes the excess memory in the first phase and how can it be reduced? How can the second phase of memory be made to start earlier, and how might a third phase of memory be incorporated into the diurnal cycle? The key to answering some of these questions lies in performing extensive simulations of different convective test cases with different initial and forcing conditions using the CoMorph scheme.

Evaluating memory properties within a convective parameterization scheme simply cannot be done in isolation—it would have to be done in conjunction with investigations of different convective properties (e.g. mass flux, cloud fraction, precipitation), as well as thermodynamic properties (e.g. potential temperature, water vapour) and dynamic properties (e.g. winds, convective available potential energy). Only then can possible physical links be established between the scheme parameters and the memory mechanisms influencing the simulated convective response. Understanding these physical causes will in turn provide deeper insight into the source of potential biases in the model output and into the modifications that need to be conducted within the scheme to achieve the desired convective behaviour. Diagnosis of the memory source could also be achieved using a brute force method wherein a wide range of relevant scheme parameters (far more than the two cases we considered in this study) are modified individually or in combination and the resulting changes in the memory effects are examined. Performing such an experiment may point us to any physical or artificial sources of memory arising from components within the parameterization scheme.

The performance of CoMorph in different convective situations and time scales (e.g. the diurnal cycle, monsoons, MJO/ENSO, midlatitude cyclones) can be compared to identify specific attributes and/or phenomena that the scheme struggles to realistically represent (e.g. thermodynamic fluctuations such as cold pools). Focused efforts could be directed toward the representation of those physical processes within the scheme, through prognostic variables or modified closure conditions. This is equivalent to what was done in the studies summarized in Section 1.2.3, where attempts were made to incorporate sources of convective memory within parameterizations.

Lastly, simulations of the diurnal cycle could be gradually rendered more realistic and changes in the memory properties could be studied. For instance, initial thermodynamic conditions could be set to match observed values instead of being homogeneous, and the surface radiative forcing could be allowed to interact with the atmosphere. A heterogeneous surface representing the land-sea interface could also be used. Comparing memory effects in realistic versus idealized conditions might throw light on where an excess or deficit of memory arises from and how it can be rectified.

"If I have seen further, it is by standing on the shoulders of giants."
— Isaac Newton

References

Arakawa, A., 2004: The cumulus parameterization problem: Past, present, and future. *J. Climate*, **17**, 2493–2525, doi:10.1175/1520-0442(2004)017<2493:RATCPP>2.0.CO;2.

Arakawa, A., and W. H. Schubert, 1974: Interaction of a cumulus cloud ensemble with the large-scale environment, Part I. *J. Atmos. Sci.*, **31**, 674–701, doi:10.1175/1520-0469(1974)031<0674:IOACCE>2.0.CO;2.

Bechtold, P., J.-P. Chaboureau, A. Beljaars, A. K. Betts, M. Köhler, M. Miller, and J.-L. Redelsperger, 2004: The simulation of the diurnal cycle of convective precipitation over land in a global model. *Q. J. R. Meteorol. Soc.*, **130**, 3119–3137, doi:10.1256/qj.03.103.

Bechtold, P., N. Semane, P. Lopez, J.-P. Chaboureau, A. Beljaars, and N. Bormann, 2014: Representing equilibrium and nonequilibrium convection in large-scale models. *J. Atmos. Sci.*, **71**, 734–753, doi:10.1175/JAS-D-13-0163.1.

Betts, A. K., 1986: A new convective adjustment scheme. Part I: Observational and theoretical basis. *Q. J. Roy. Meteorol. Soc.*, **112**, 677–691, doi:10.1002/qj.49711247307.

Betts, A. K., and C. Jakob, 2002: Evaluation of the diurnal cycle of precipitation, surface thermodynamics, and surface fluxes in the ECMWF model using LBA data. *J. Geophys. Res. Atmos.*, **107**, LBA 12–1–LBA 12–8, doi:10.1029/2001JD000427.

Brown, N., M. Weiland, A. Hill, B. Shipway, C. Maynard, T. Allen, and M. Rezny, 2020: A highly scalable Met Office NERC Cloud model, https://arxiv.org/abs/2009.12849.

Chaboureau, J.-P., F. Guichard, J.-L. Redelsperger, and J.-P. Lafore, 2004: The role of stability and moisture in the diurnal cycle of convection over land. *Q. J. R. Meteorol. Soc.*, **130**, 3105–3117, doi:10.1256/qj.03.132.

Chen, D., and P. Bougeault, 1993: A simple prognostic closure assumption to deep convective parameterization: I. *Acta Meteor. Sin.*, **1**, 1–18.

Christopoulos, C., and T. Schneider, 2021: Assessing Biases and Climate Implications of the Diurnal Precipitation Cycle in Climate Models. *Geophys. Res. Lett.*, **48**, 1–9, doi:10.1029/2021GL093017.

Colin, M., S. Sherwood, O. Geoffroy, S. Bony, and D. Fuchs, 2019: Identifying the sources of convective memory in cloud-resolving simulations. *J. Atmos. Sci.*, **76**, 947–962, doi:10.1175/JAS-D-18-0036.1.

Cullen, M. J. P., 1993: The Unified Forecast/Climate Model. *Meteor. Mag.*, **122**, 81–94.

Daleu, C. L., R. S. Plant, S. J. Woolnough, A. J. Stirling, and N. J. Harvey, 2020: Memory Properties in Cloud-Resolving Simulations of the Diurnal Cycle of Deep Convection. *J. Adv. Model. Earth Syst.*, **12**, doi:10.1029/2019MS001897.

Davies, L., R. Plant, and S. Derbyshire, 2013: Departures from convective equilibrium with a rapidly varying surface forcing. *Q. J. Roy. Meteorol. Soc.*, **139**, 1731–1746.

Davies, L., R. S. Plant, and S. H. Derbyshire, 2009: A simple model of convection with memory. *J. Geophys. Res. Atmos.*, **114**, 2–7, doi:10.1029/2008JD011653.

Del Genio, A. D., J. Wu, A. B. Wolf, Y. Chen, M.-S. Yao, and D. Kim, 2015: Constraints on cumulus parameterization from simulations of observed MJO events. *J. Climate*, **28**, 6419–6442, doi:10.1175/JCLI-D-14-00832.1.

DeMott, C. A., D. A. Randall, and M. Khairoutdinov, 2007: Convective precipitation variability as a tool for general circulation model analysis. *J. Climate*, **20**, 91–112, doi:10.1175/JCLI3991.1.

Donner, L. J., 1993: A cumulus parameterization including mass fluxes, vertical momentum dynamics, and mesoscale effects. *J. Atmos. Sci.*, **50**, 889–906, doi:10.1175/1520-0469(1993)050<0889:ACPIMF>2.0.CO;2.

Edwards, J. M., and A. Slingo, 1996: Studies with a flexible new radiation code. I: Choosing a configuration for a large-scale model. *Q. J. Roy. Meteorol. Soc.*, **122**, 689–719, doi:10.1002/qj.49712253107.

Emanuel, K. A., 1991: A scheme for representing cumulus convection in large-scale models. *J. Atmos. Sci.*, **48**, 2313–2329, doi:10.1175/1520-0469(1991)048<2313:ASFRCC>2.0.CO;2.

Folkins, I., T. Mitovski, and J. R. Pierce, 2014: A simple way to improve the diurnal cycle in convective rainfall over land in climate models. *J. Geophys. Res.*, **119**, 2113–2130, doi:10.1002/2013JD020149.

Gerard, L., J.-M. Piriou, R. Brožková, J.-F. Geleyn, and D. Banciu, 2009: Cloud and precipitation parameterization in a meso-gamma-scale operational weather prediction model. *Mon. Wea. Rev.*, **137**, 3960–3977, doi:10.1175/2009MWR2750.1.

Grabowski, W. W., 2001: Coupling cloud processes with the large-scale dynamics using the cloud-resolving convection parameterization (CRCP). *J. Atmos. Sci.*, **58**, 978–997, doi:10.1175/1520-0469(2001)058<0978:CCPWTL>2.0.CO;2.

Grandpeix, J.-Y., and J.-P. Lafore, 2010: A density current parameterization coupled with Emanuel's convection scheme. Part I: The models. *J. Atmos. Sci.*, **67**, 881–897, doi:10.1175/2009JAS3044.1.

Gregory, D., and P. R. Rowntree, 1990: A mass flux convection scheme with representation of cloud ensemble characteristics and stability-dependent closure. *Mon. Wea. Rev.*, **118**, 1483–1506, doi:10.1175/1520-0493(1990)118<1483:AMFCSW>2.0.CO;2.

Grosvenor, D. P., P. R. Field, A. A. Hill, and B. J. Shipway, 2017: The relative importance of macrophysical and cloud albedo changes for aerosol-induced radiative effects in closed-cell stratocumulus: Insight from the modelling of a case study. *Atmos. Chem. Phys.*, **17**, 5155–5183, doi:10.5194/acp-17-5155-2017.

Guichard, F., and F. Couvreux, 2017: A short review of numerical cloud-resolving models. *Tellus A: Dynamic Meteorology and Oceanography*, **69**, 1–36, doi:10.1080/16000870.2017.1373578.

Guichard, F., and Coauthors, 2004: Modelling the diurnal cycle of deep precipitating convection over land with cloud-resolving models and single-column models. *Q. J. R. Meteorol. Soc.*, **130**, 3139–3172, doi:10.1256/qj.03.145.

Guérémy, J., 2011: A continuous buoyancy based convection scheme: One- and three-dimensional validation. *Tellus, Ser. A Dyn. Meteorol. Oceanogr.*, **63**, 687–706, doi:10.1111/j.1600-0870.2011.00521.x.

Hill, A. A., P. R. Field, K. Furtado, A. Korolev, and B. J. Shipway, 2014: Mixed-phase clouds in a turbulent environment. Part 1: Large-eddy simulation experiments. *Q. J. Roy. Meteorol. Soc.*, **140**, 855–869, doi:10.1002/qj.2177.

Hohenegger, C., and C. S. Bretherton, 2011: Simulating deep convection with a shallow convection scheme. *Atmos. Chem. Phys.*, **11**, 10 389–10 406, doi:10.5194/acp-11-10389-2011.

Jones, T. R., and D. A. Randall, 2011: Quantifying the limits of convective parameterizations. *J. Geophys. Res. Atmos.*, **116**, 1–19, doi:10.1029/2010JD014913.

Kain, J. S., and J. M. Fritsch, 1990: A one-dimensional entraining/detraining plume model and its application in convective parameterization. *J. Atmos. Sci.*, **47**, 2784–2802, doi:10.1175/1520-0469(1990)047<2784:AODEPM>2.0.CO;2.

Khairoutdinov, M., D. Randall, and C. DeMott, 2005: Simulations of the atmospheric general circulation using a cloud-resolving model as a superparameterization of physical processes. *J. Atmos. Sci.*, **62**, 2136–2154, doi:10.1175/JAS3453.1.

Khairoutdinov, M. F., and D. A. Randall, 2001: A cloud resolving model as a cloud parameterization in the NCAR community climate system model: Preliminary results. *Geophys. Res. Lett.*, **28**, 3617–3620, doi:10.1029/2001GL013552.

Khouider, B., J. Biello, and A. J. Majda, 2010: A stochastic multicloud model for tropical convection. *Commun. Math. Sci.*, **8**, 187–216, doi:10.4310/cms.2010.v8.n1.a10.

Kuo, H. L., 1974: Further studies of the parameterization of the influence of cumulus convection on large-scale flow. *J. Atmos. Sci.*, **31**, 1232–1240, doi:10.1175/1520-0469(1974)031<1232:FSOTPO>2.0.CO;2.

Lin, X., D. A. Randall, and L. D. Fowler, 2000: Diurnal variability of the hydrologic cycle and radiative fluxes: Comparisons between observations and a GCM. *J. Climate*, **13**, 4159–4179, doi:10.1175/1520-0442(2000)013<4159:DVOTHC>2.0.CO;2.

Lock, A. P., A. R. Brown, M. R. Bush, G. M. Martin, and R. N. B. Smith, 2000: A new boundary layer mixing scheme. Part I: Scheme description and single-column model tests. *Mon. Wea. Rev.*, **128**, 3187–3199, doi:10.1175/1520-0493(2000)128<3187:ANBLMS>2.0.CO;2.

Lott, F., and M. J. Miller, 1997: A new subgrid-scale orographic drag parametrization: Its formulation and testing. *Q. J. Roy. Meteorol. Soc.*, **123**, 101–127, doi:10.1002/qj.49712353704.

Mapes, B., and R. Neale, 2011: Parameterizing convective organization to escape the entrainment dilemma. *J. Adv. Model. Earth Syst.*, **3**, 1–20, doi:10.1029/2011MS000042.

Marsham, J. H., S. Dobbie, and R. J. Hogan, 2006: Evaluation of a large-eddy model simulation of a mixed-phase altocumulus cloud using microwave radiometer, lidar and Doppler radar data. *Q. J. Roy. Meteorol. Soc.*, **132**, 1693–1715, doi:10.1256/qj.05.145.

Pan, D.-M., and D. D. A. Randall, 1998: A cumulus parameterization with a prognostic closure. *Q. J. Roy. Meteorol. Soc.*, **124**, 949–981, doi:10.1002/qj.49712454714.

Park, S., 2014: A unified convection scheme (UNICON). Part I: Formulation. *J. Atmos. Sci.*, **71**, 3902–3930, doi:10.1175/JAS-D-13-0233.1.

Piriou, J.-M., J.-L. Redelsperger, J.-F. Geleyn, J.-P. Lafore, and F. Guichard, 2007: An approach for convective parameterization with memory: Separating microphysics and transport in grid-scale equations. *J. Atmos. Sci.*, **64**, 4127–4139, doi:10.1175/2007JAS2144.1.

Plant, R. S., and J.-I. Yano, 2016: *Parameterization of Atmospheric Convection*, Series on the Science of Climate Change, Vol. 1. 1st ed., ICP, Imperial College Press.

Qian, L., G. S. Young, and W. M. Frank, 1998: A convective wake parameterization scheme for use in general circulation models. *Mon. Wea. Rev.*, **126**, 456–469, doi:10.1175/1520-0493(1998)126<0456:ACWPSF>2.0.CO;2.

Rio, C., A. D. Del Genio, and F. Hourdin, 2019: Ongoing Breakthroughs in Convective Parameterization. *Curr. Clim. Change Rep.*, **5**, 95–111, doi:10.1007/s40641-019-00127-w.

Rio, C., F. Hourdin, J.-Y. Grandpeix, and J.-P. Lafore, 2009: Shifting the diurnal cycle of parameterized deep convection over land. *Geophys. Res. Lett.*, **36**, 1–5, doi:10.1029/2008GL036779.

Romps, D. M., 2016: The stochastic parcel model: A deterministic parameterization of stochastically entraining convection. *J. Adv. Model. Earth Syst.*, **8**, 319–344, doi:10.1002/2015MS000537.

Romps, D. M., and Z. Kuang, 2010: Nature versus nurture in shallow convection. *J. Atmos. Sci.*, **67**, 1655–1666, doi:10.1175/2009JAS3307.1.

Saffin, L., L. Denby, S. Böing, A. Blyth, M. Whitall, L. Tomassini, A. Lock, and A. Stirling, 2021: Driving a Convection Parametrization with EUREC4A Observations. Presentation at: EGU General Assembly 2021, 19–30 April, https://meetingorganizer.copernicus.org/egu21/egu21-14886.html?pdf.

Sato, T., H. Miura, M. Satoh, Y. N. Takayabu, and Y. Wang, 2009: Diurnal cycle of precipitation in the tropics simulated in a global cloud-resolving model. *J. Climate*, **22**, 4809–4826, doi:10.1175/2009JCLI2890.1.

Scaife, A. A., N. Butchart, C. D. Warner, and R. Swinbank, 2002: Impact of a spectral gravity wave parameterization on the stratosphere in the Met Office Unified Model. *J. Atmos. Sci.*, **59**, 1473–1489, doi:10.1175/1520-0469(2002)059<1473:IOASGW>2.0.CO;2.

Scinocca, J. F., and N. A. McFarlane, 2004: The variability of modeled tropical precipitation. *J. Atmos. Sci.*, **61**, 1993–2015, doi:10.1175/1520-0469(2004)061<1993:TVOMTP>2.0.CO;2.

Stirling, A. J., and J. C. Petch, 2004: The impacts of spatial variability on the development of convection. *Q. J. Roy. Meteorol. Soc.*, **130**, 3189–3206, doi:10.1256/qj.03.137.

Stratton, R. A., and A. J. Stirling, 2012: Improving the diurnal cycle of convection in GCMs. *Q. J. R. Meteorol. Soc.*, **138**, 1121–1134, doi:10.1002/qj.991.

Suselj, K., M. J. Kurowski, and J. Teixeira, 2019: A unified eddy-diffusivity/mass-flux approach for modeling atmospheric convection. *J. Atmos. Sci.*, **76**, 2505–2537, doi:10.1175/JAS-D-18-0239.1.

Sušelj, K., J. Teixeira, and D. Chung, 2013: A unified model for moist convective boundary layers based on a stochastic eddy-diffusivity/mass-flux parameterization. *J. Atmos. Sci.*, **70**, 1929–1953, doi:10.1175/JAS-D-12-0106.1.

Tao, W.-K., and Coauthors, 2009: A multiscale modeling system: Developments, applications, and critical issues. *Bull. Amer. Meteor. Soc.*, **90**, 515–534, doi:10.1175/2008BAMS2542.1.

Wagner, T. M., and H.-F. Graf, 2010: An ensemble cumulus convection parameterization with explicit cloud treatment. *J. Atmos. Sci.*, **67**, 3854–3869, doi:10.1175/2010JAS3485.1.

Walters, D., and Coauthors, 2019: The met office unified model global atmosphere 7.0/7.1 and jules global land 7.0 configurations. *Geosci. Model Dev*, **12**, 1909–1963, doi:10.5194/gmd-12-1909-2019.

Whitall, M., 2019: A New Generalised Mass-flux Convection Scheme for the Met Office Unified Model. Presentation at: Met Office Convection Parameterisation: Progress and Challenges (CPPC) Workshop 2019, 15–19 July, http://sites.exeter.ac.uk/convection-workshop/files/2019/10/whitall_comorph_cppc2019.pptx.

Wilson, D. R., and S. P. Ballard, 1999: A microphysically based precipitation scheme for the UK Meteorological Office Unified Model. *Q. J. Roy. Meteorol. Soc.*, **125**, 1607–1636, doi:10.1002/qj.49712555707.

Xie, S., and Coauthors, 2002: Intercomparison and evaluation of cumulus parametrizations under summertime midlatitude continental conditions. *Q. J. R. Meteorol. Soc.*, **128**, 1095–1135, doi:10.1256/003590002320373229.

Xu, K.-M., and Coauthors, 2002: An intercomparison of cloud-resolving models with the Atmospheric Radiation Measurement summer 1997 intensive observation period data. *Q. J. R. Meteorol. Soc.*, **128**, 593–624, doi:10.1256/003590002321042117.

Yang, G.-Y., and J. Slingo, 2001: The diurnal cycle in the tropics. *Mon. Wea. Rev.*, **129**, 784–801, doi:10.1175/1520-0493(2001)129<0784:TDCITT>2.0.CO;2.

Yano, J.-I., and M. W. Moncrieff, 2016: Numerical archetypal parameterization for mesoscale convective systems. *J. Atmos. Sci.*, **73**, 2585–2602, doi:10.1175/JAS-D-15-0207.1.

Yano, J.-I., and R. Plant, 2012: Finite departure from convective quasi-equilibrium: Periodic cycle and discharge–recharge mechanism. *Q. J. Roy. Meteorol. Soc.*, **138**, 626–637, doi:https://doi.org/10.1002/qj.957.

Zhang, G. J., and N. A. McFarlane, 1995: Sensitivity of climate simulations to the parameterization of cumulus convection in the Canadian climate centre general circulation model. *Atmos. - Ocean*, **33**, 407–446, doi:10.1080/07055900.1995.9649539.

Zhang, Y., and Coauthors, 2008: On the diurnal cycle of deep convection, high-level cloud, and upper troposphere water vapor in the Multiscale Modeling Framework. *J. Geophys. Res. Atmos.*, **113**, 1–19, doi:10.1029/2008JD009905.

Appendix

"The unexamined life is not worth living."
— Socrates

Additional plots are presented in this section for the sake of completeness.

Figure 31 and Figure 32 show probability and memory functions for the UM CoMorph 4 km simulation, evaluated for different spatial areas A, different times t_0 after triggering, and different values of rain thresholds. MONC memory functions for A = 4 x 4 km^2 are also shown for comparison. Figure 33 and Figure 34 present the same plots for the CoMorph 10 km simulation, Figure 35 and Figure 36 do so for the CoMorph 50 km simulation, and Figure 37 for the 6A 10 km simulation.

Figures 38 to 40 show large-scale (>20 km) spatial thermodynamic anomalies (anomalies in potential temperature θ and water vapour q_v with respect to the domain mean) along the horizontal and vertical dimensions for CoMorph 4, 10, and 50 km simulations.

Figure 41 and Figure 42 show probability and memory functions for the CoMorph 4 km - Case 2 and Case 3 simulations, evaluated for different spatial areas A, different times t_0 after triggering, and different values of rain thresholds. Figure 43 and Figure 44 show large-scale spatial thermodynamic fluctuations for the CoMorph 4 km Case 2 and Case 3 simulations respectively.

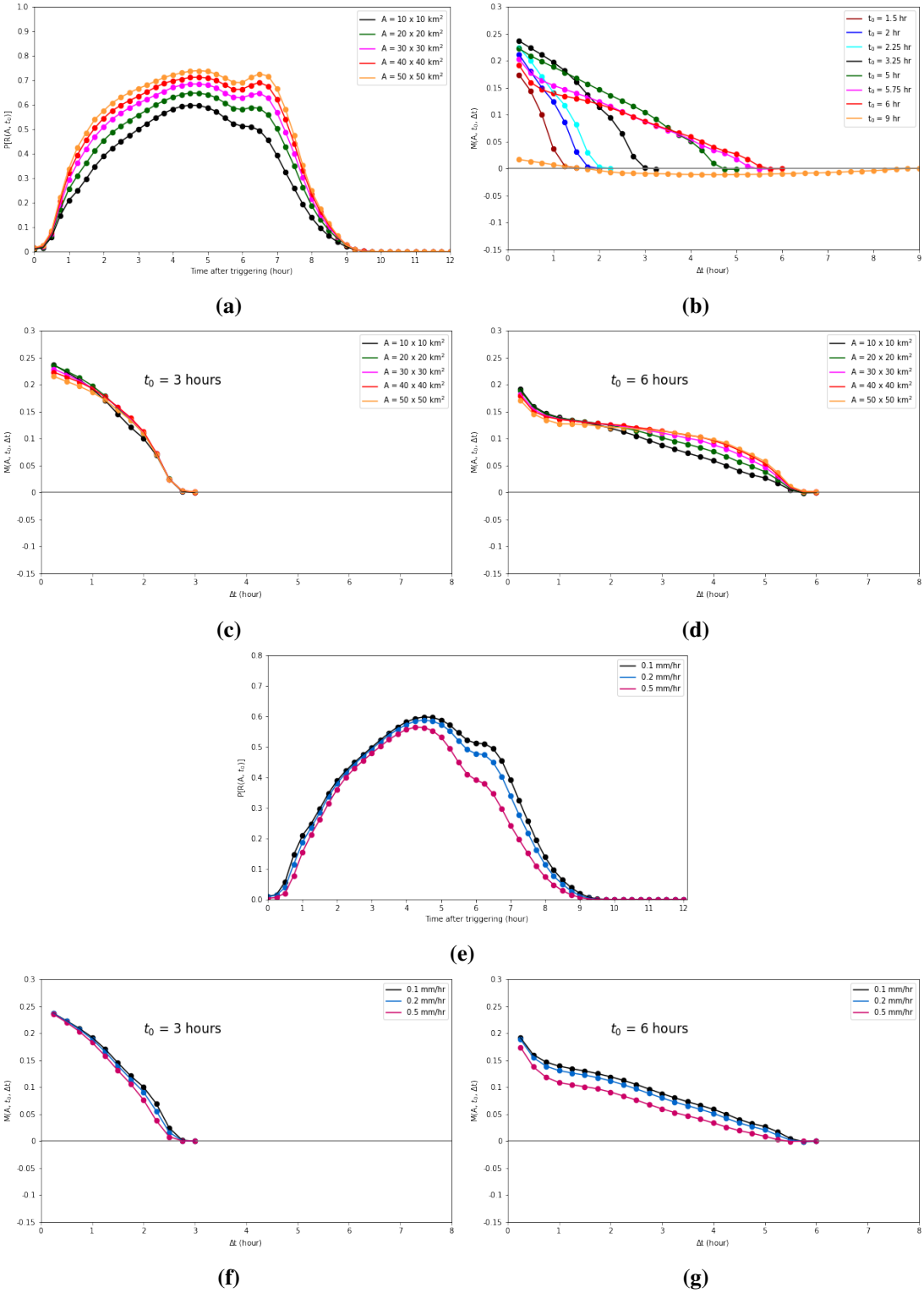

Figure 31: a. Probabilities of finding rain (P[R(A, t_0)]) for different areas A = 4x4 km^2, 8x8 km^2, 16x16 km^2, 24x24 km^2 and 48x48 km^2 in the UM CoMorph 4 km simulations. The time axis is shifted such that time equals zero corresponds to the time of triggering. b. Memory functions (**M**(A, t_0, Δt)) for A = 4x4 km^2 for different times t_0 = 1.5, 2, 2.25, 3.25, 5, 6, and 9 hours after triggering. Memory functions for different areas are shown for (c.) t_0 = 3 hours and (d.) 6 hours after triggering. e. Probabilities of finding rain (P[R(A, t_0)]) for A = 10x10 km^2 for different rain thresholds of 0.1, 0.2 and 0.5 mm hr^{-1} in the UM CoMorph 4 km simulations. Memory functions (**M**(A, t_0, Δt)) for A = 10x10 km^2 for different rain thresholds for (f.) t_0 = 3 and (g.) 6 hours after triggering.

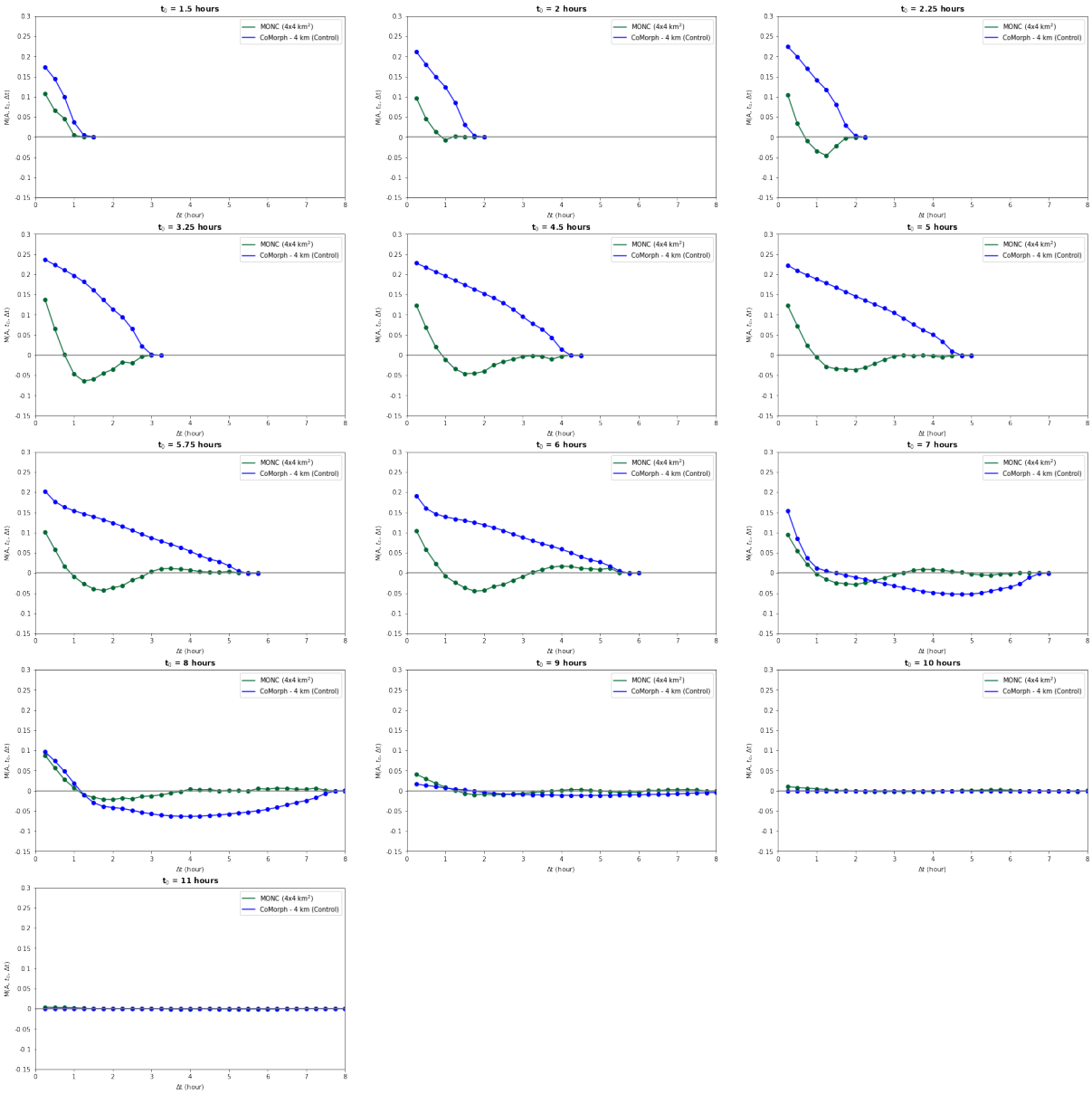

Figure 32: Memory functions (**M**(A, t_0, Δt)) for the UM CoMorph simulation with 4 km resolution are shown (in blue) for different times t_0 = 1.2, 2, 2.25, 3.25, 4.5, 5, 5.75, 6, 7, 8, 9, 10 and 11 hours after triggering. MONC memory functions for spatial area A = 4x4 km^2 are also shown (in green) for comparison.

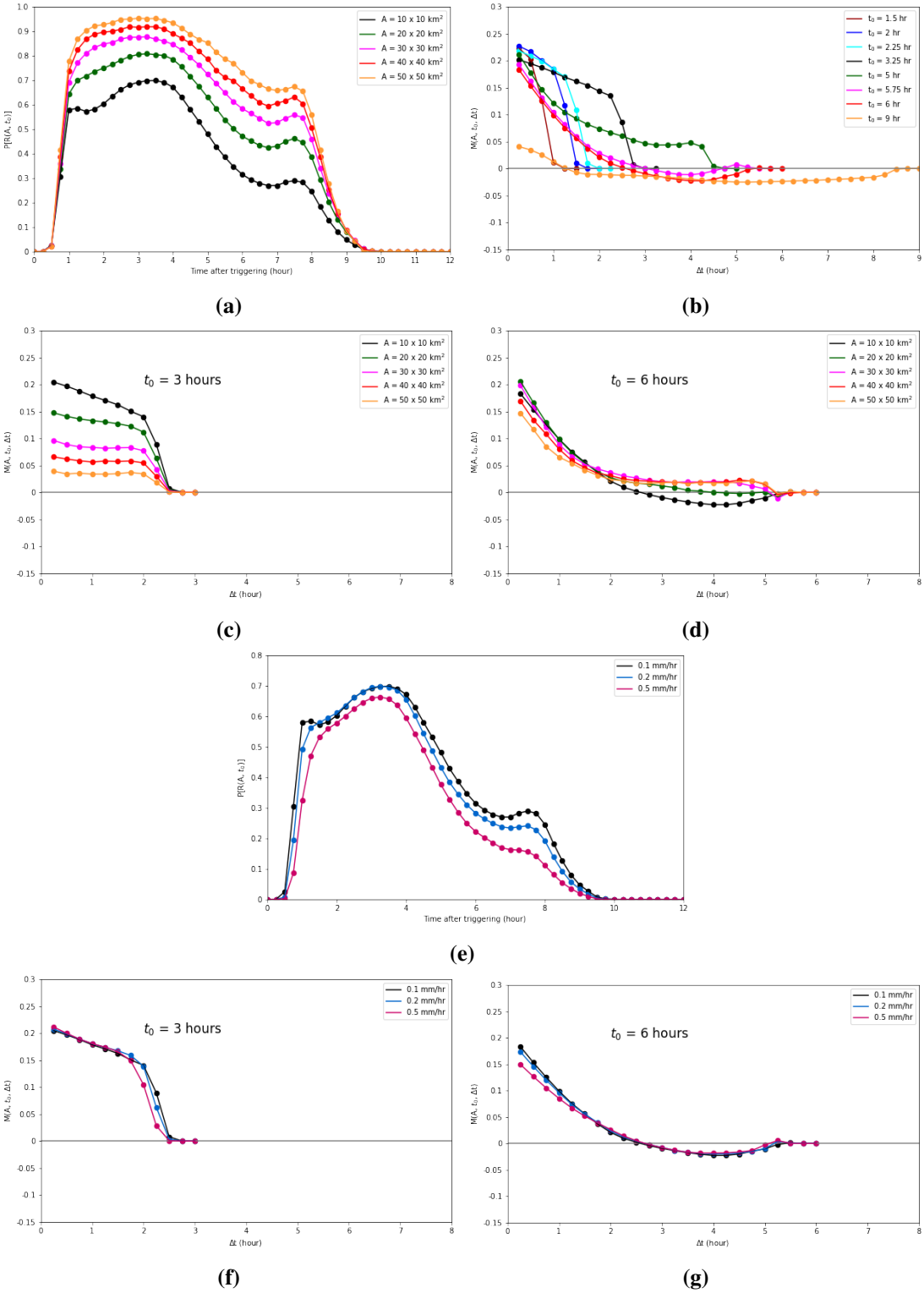

Figure 33: a. Probabilities of finding rain (P[R(A, t_0)]) for different areas A = 10x10 km^2, 20x20 km^2, 30x30 km^2, 40x40 km^2 and 50x50 km^2 in the UM CoMorph 10 km simulations. The time axis is shifted such that time equals zero corresponds to the time of triggering. b. Memory functions (**M**(A, t_0, Δt)) for A = 10x10 km^2 for different times t_0 = 1.5, 2, 2.25, 3.25, 5, 6, and 9 hours after triggering. Memory functions for different areas are shown for (c.) t_0 = 3 hours and (d.) 6 hours after triggering. e. Probabilities of finding rain (P[R(A, t_0)]) for A = 10x10 km^2 for different rain thresholds of 0.1, 0.2 and 0.5 mm hr^{-1} in the UM CoMorph 10 km simulations. Memory functions (**M**(A, t_0, Δt)) for A = 10x10 km^2 for different rain thresholds for (f.) t_0 = 3 and (g.) 6 hours after triggering.

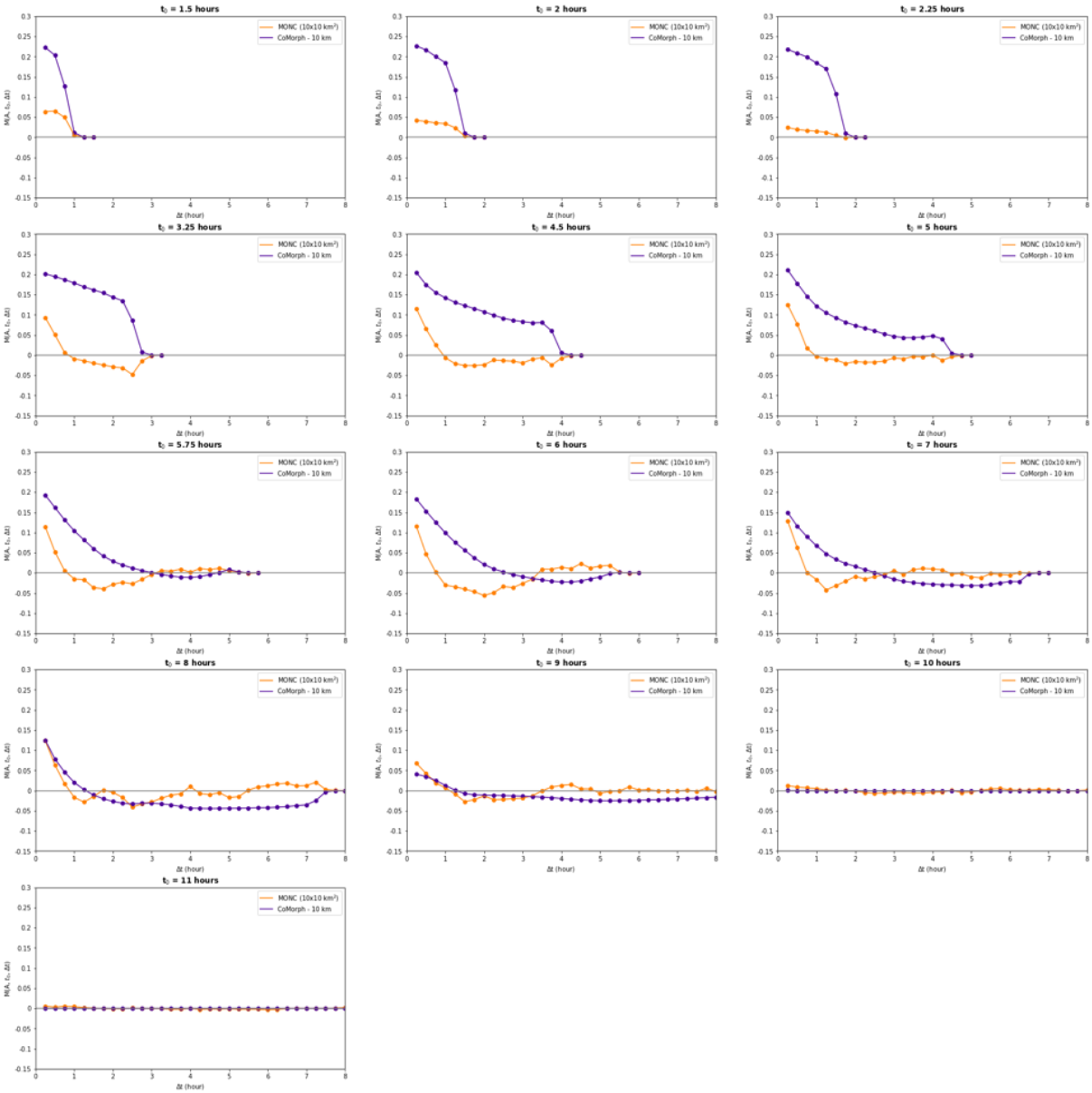

Figure 34: Memory functions (**M**(A, t_0, Δt)) for the UM CoMorph simulation with 10 km resolution are shown (in purple) for different times t_0 = 1.2, 2, 2.25, 3.25, 4.5, 5, 5.75, 6, 7, 8, 9, 10 and 11 hours after triggering. MONC memory functions for spatial area A = 10x10 km^2 are also shown (in orange) for comparison.

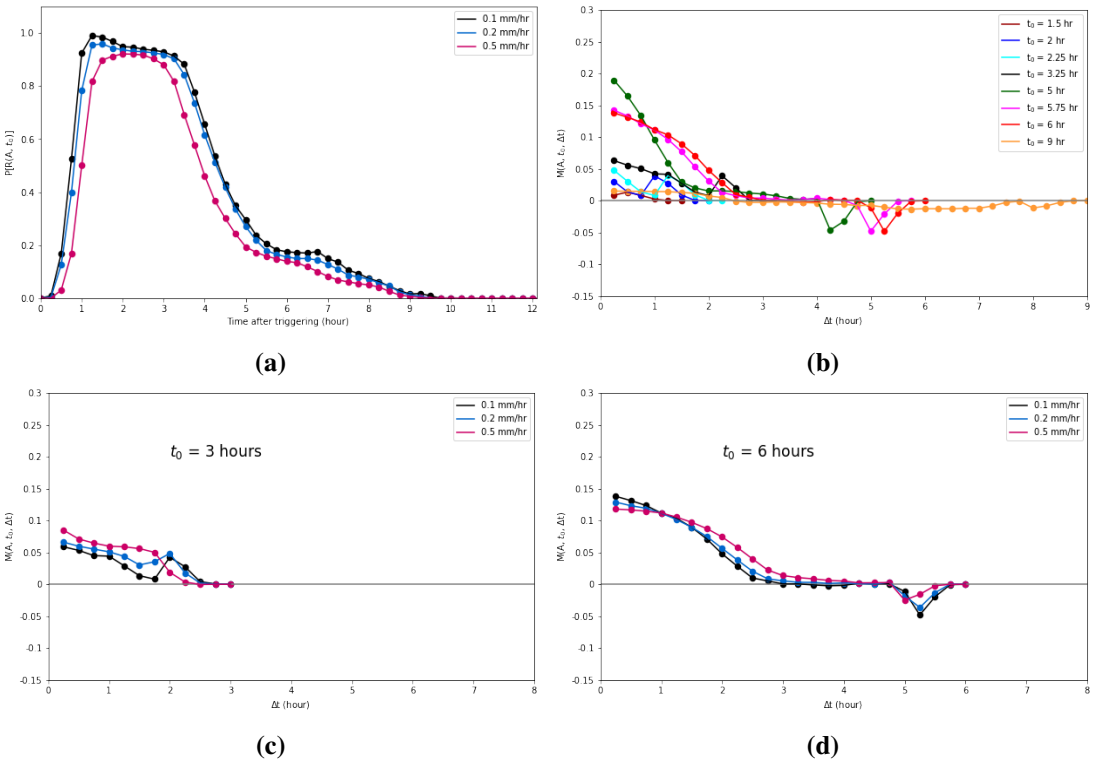

Figure 35: a. Probabilities of finding rain (P[R(A, t_0)]) for for A = 50x50 km^2 for different rain thresholds of 0.1, 0.2 and 0.5 mm hr^{-1} in the UM CoMorph 50 km simulations. The time axis is shifted such that time equals zero corresponds to the time of triggering. b. Memory functions (**M**(A, t_0, Δt)) for A = 50x50 km^2 for different times t_0 = 1.5, 2, 2.25, 3.25, 5, 6, and 9 hours after triggering. Memory functions (**M**(A, t_0, Δt)) for A = 50x50 km^2 for different rain thresholds are shown for (c.) t_0 = 3 and (d.) 6 hours after triggering.

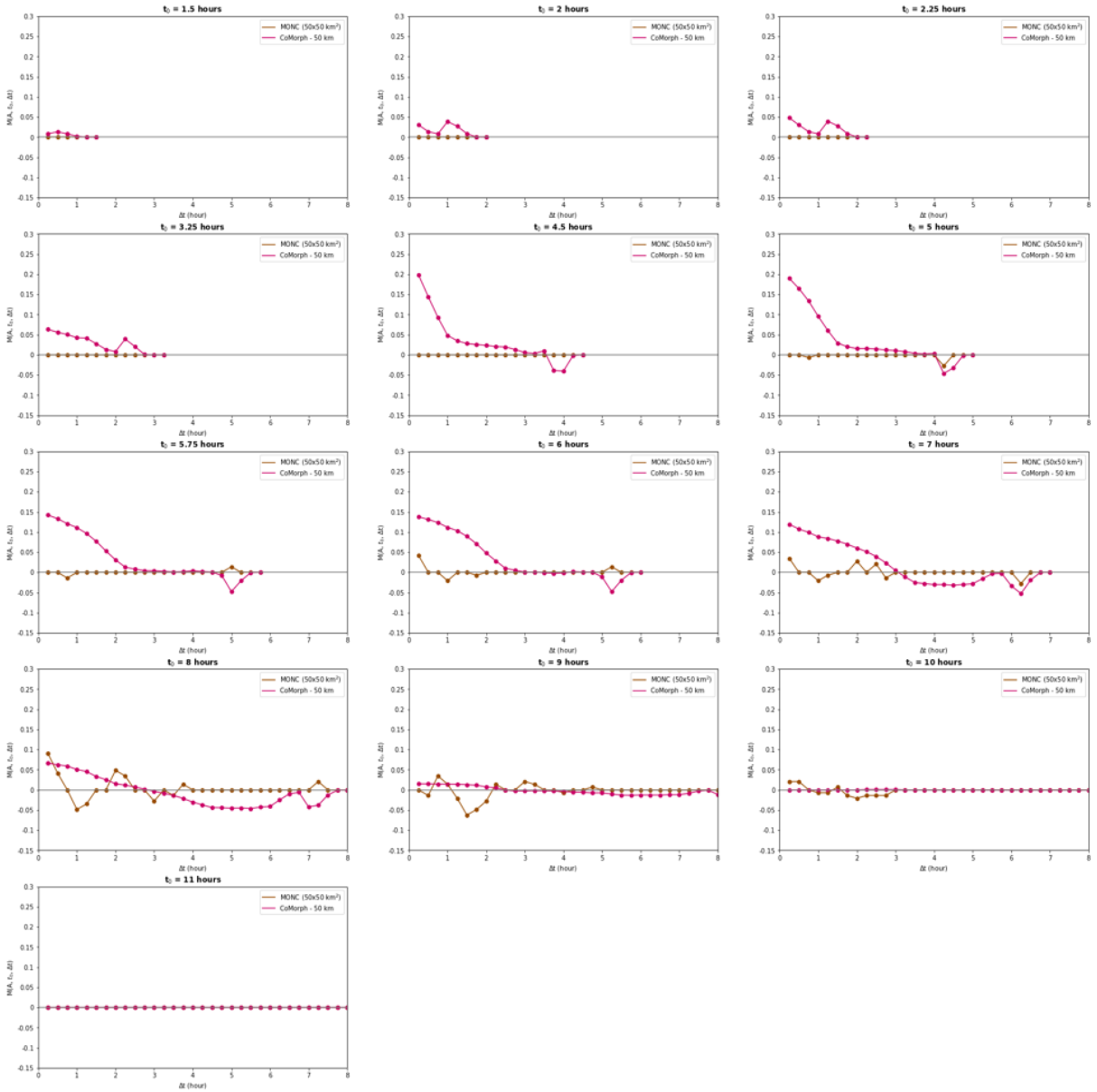

Figure 36: Memory functions (**M**(A, t_0, Δt)) for the UM CoMorph simulation with 50 km resolution are shown (in pink) for different times t_0 = 1.2, 2, 2.25, 3.25, 4.5, 5, 5.75, 6, 7, 8, 9, 10 and 11 hours after triggering. MONC memory functions for spatial area A = 50x50 km^2 are also shown (in brown) for comparison.

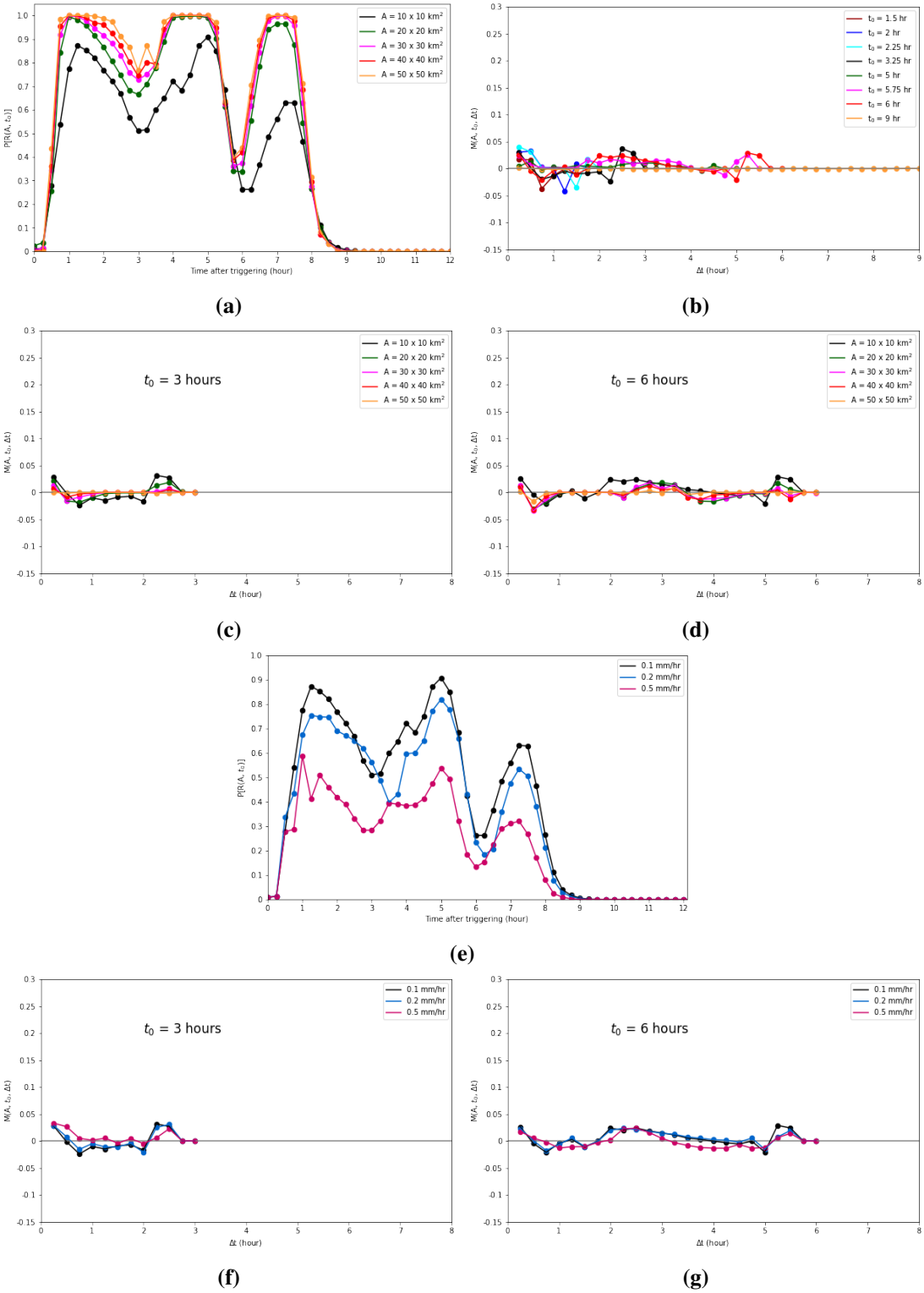

Figure 37: a. Probabilities of finding rain (P[R(A, t_0)]) for different areas A = 10x10 km^2, 20x20 km^2, 30x30 km^2, 40x40 km^2 and 50x50 km^2 in the UM 6A simulations. The time axis is shifted such that time equals zero corresponds to the time of triggering. b. Memory functions (**M**(A, t_0, Δt)) for A = 10x10 km^2 for different times t_0 = 1.5, 2, 2.25, 3.25, 5, 6, and 9 hours after triggering. Memory functions for different areas are shown for (c.) t_0 = 3 hours and (d.) 6 hours after triggering. e. Probabilities of finding rain (P[R(A, t_0)]) for A = 10x10 km^2 for different rain thresholds of 0.1, 0.2 and 0.5 mm hr^{-1} in the UM 6A simulations. Memory functions (**M**(A, t_0, Δt)) for A = 10x10 km^2 for different rain thresholds for (f.) t_0 = 3 and (g.) 6 hours after triggering.

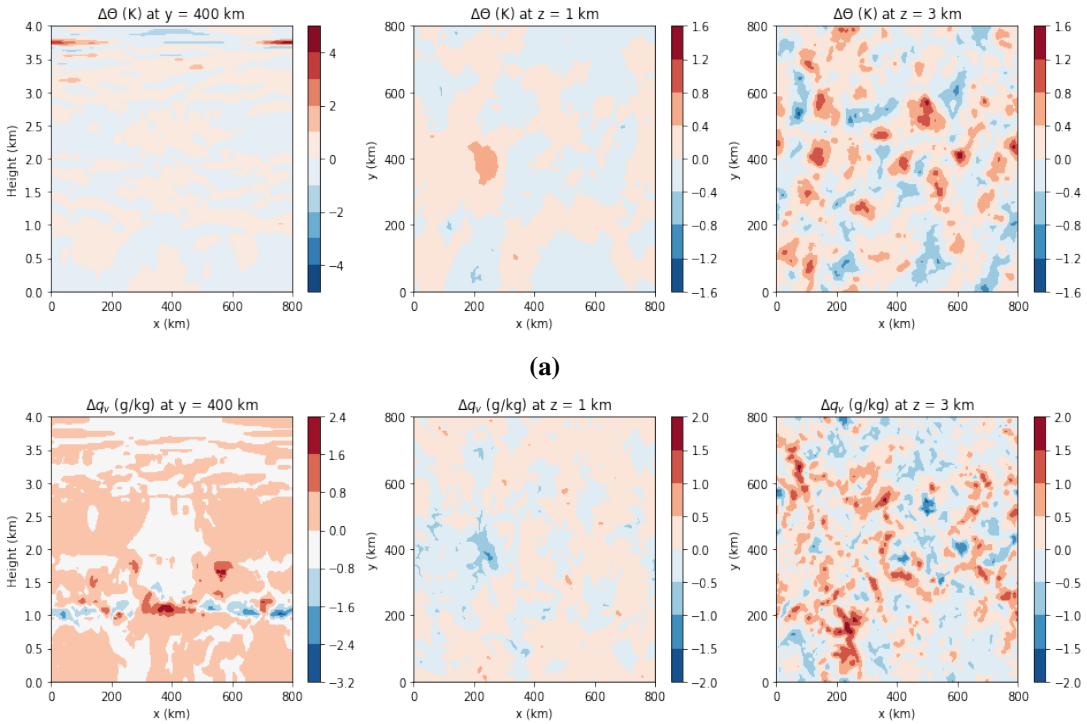

Figure 38: a. Vertical cross section at $y = 400$ km (left) and horizontal cross sections at heights of $z = 1$ km (centre) and $z = 3$ km (right) of potential temperature anomalies with respect to the domain mean at the end of the first (or sixth, as in Figure 7) diurnal cycle in the CoMorph 4 km simulation. b. Vertical cross section at $y = 400$ km (left) and horizontal cross sections at heights of $z = 1$ km (centre) and $z = 3$ km (right) of water vapour anomalies with respect to the domain mean at the end of the first diurnal cycle in the CoMorph 4 km simulation. Note that the contour intervals differ from those in Figure 19 for MONC, but remain consistent across all UM simulations.

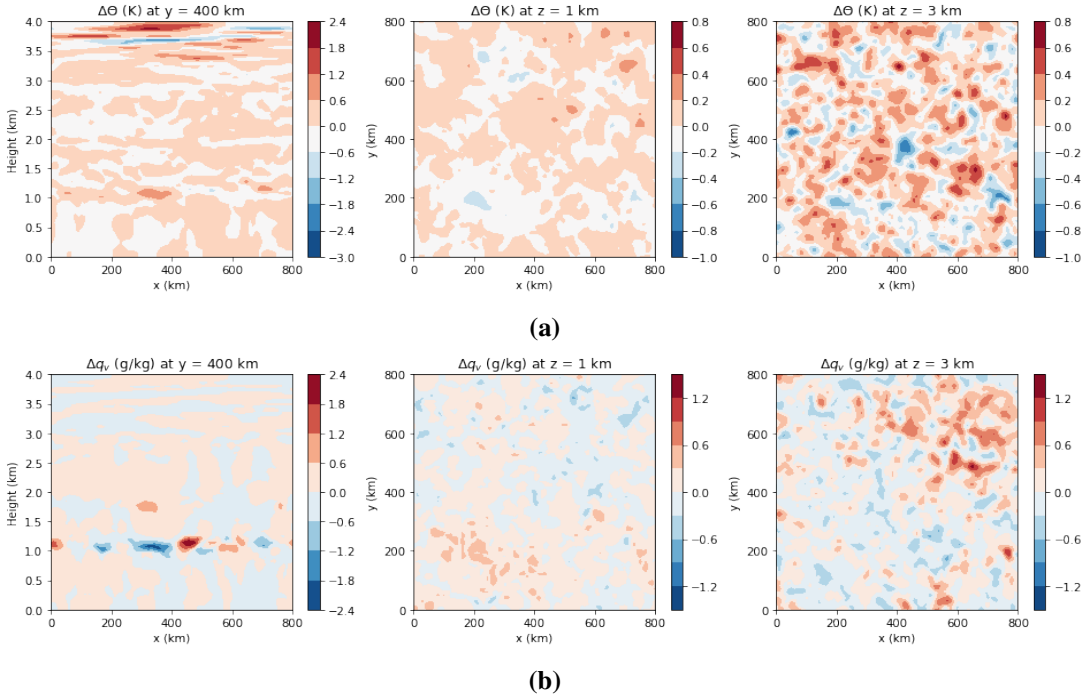

Figure 39: Same as in Figure 38 but for the CoMorph 10 km simulation.

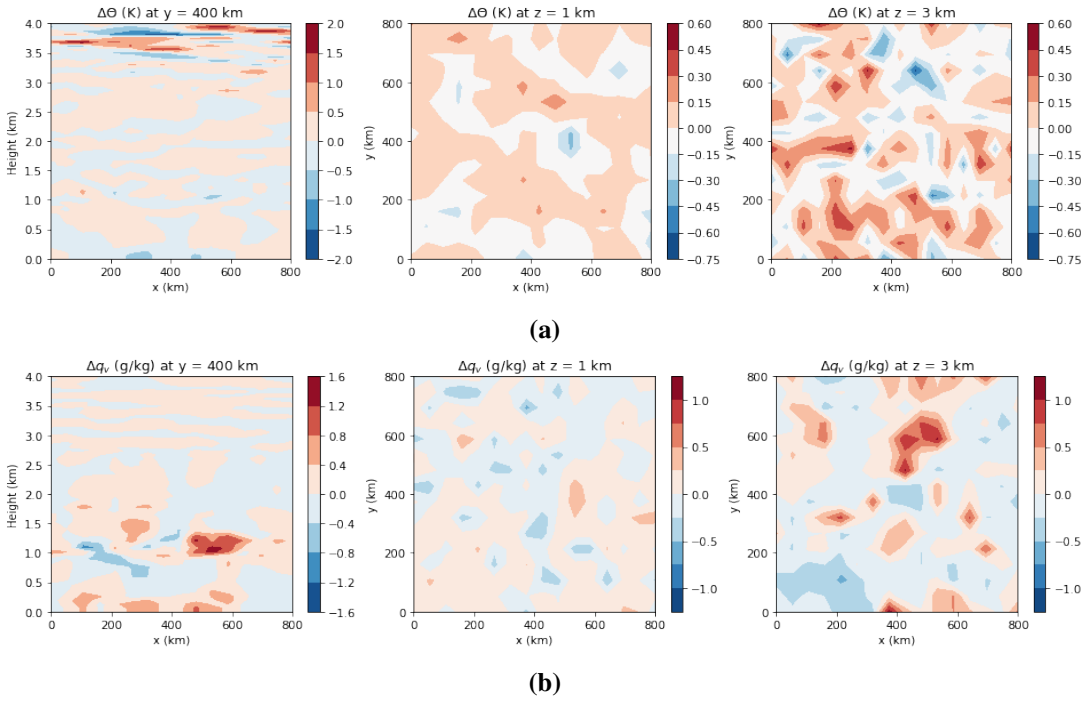

Figure 40: Same as in Figure 38 but for the CoMorph 50 km simulation.

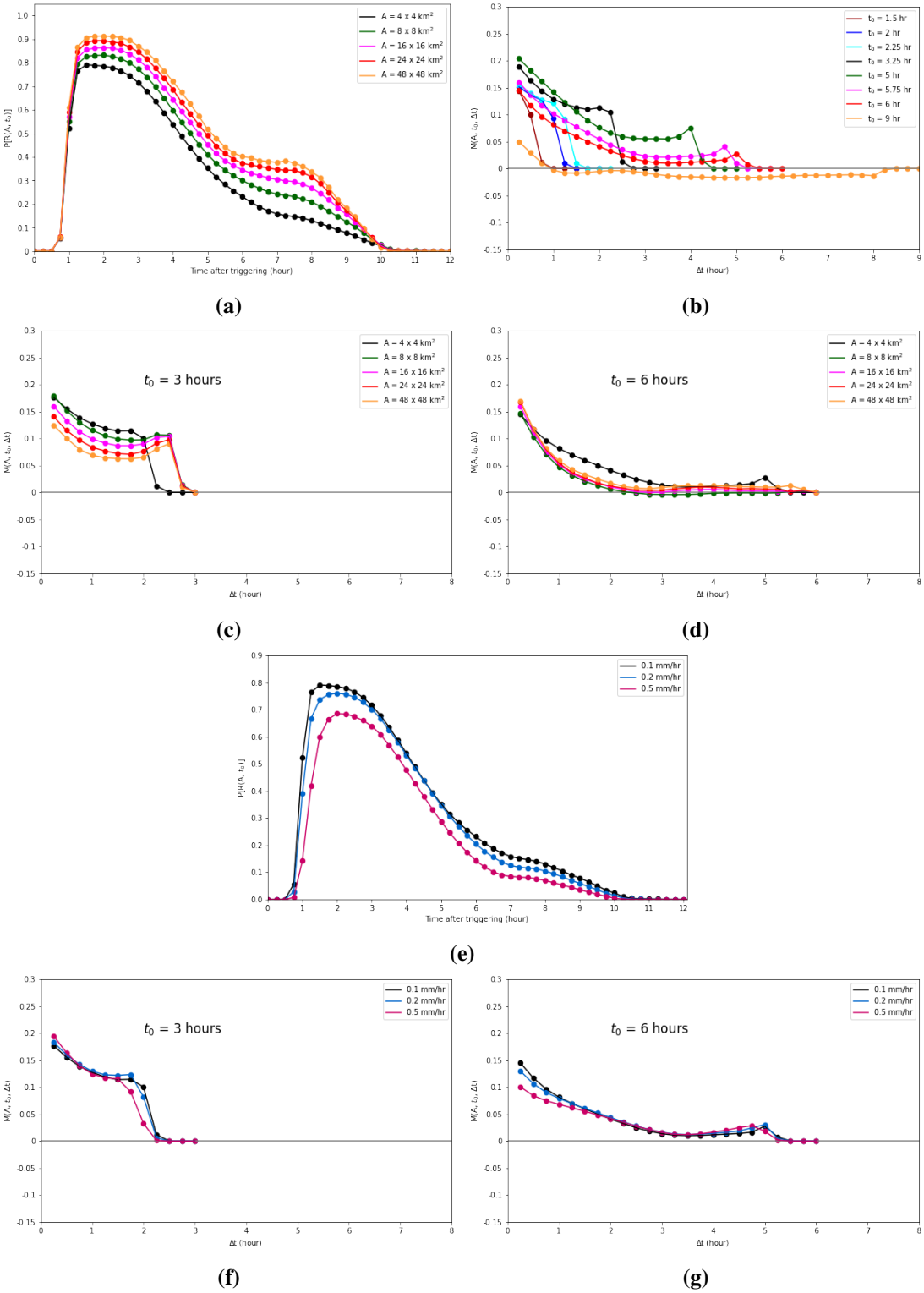

Figure 41: a. Probabilities of finding rain (P[R(A, t_0)]) for different areas A = 4x4 km^2, 8x8 km^2, 16x16 km^2, 24x24 km^2 and 48x48 km^2 in the UM CoMorph 4 km - Case 2 simulations. The time axis is shifted such that time equals zero corresponds to the time of triggering. b. Memory functions (**M**(A, t_0, Δt)) for A = 4x4 km^2 for different times t_0 = 1.5, 2, 2.25, 3.25, 5, 6, and 9 hours after triggering. Memory functions for different areas are shown for (c.) t_0 = 3 hours and (d.) 6 hours after triggering. e. Probabilities of finding rain (P[R(A, t_0)]) for A = 4x4 km^2 for different rain thresholds of 0.1, 0.2 and 0.5 mm hr^{-1} in the UM 6A simulations. Memory functions (**M**(A, t_0, Δt)) for A = 10x10 km^2 for different rain thresholds for (f.) t_0 = 3 and (g.) 6 hours after triggering.

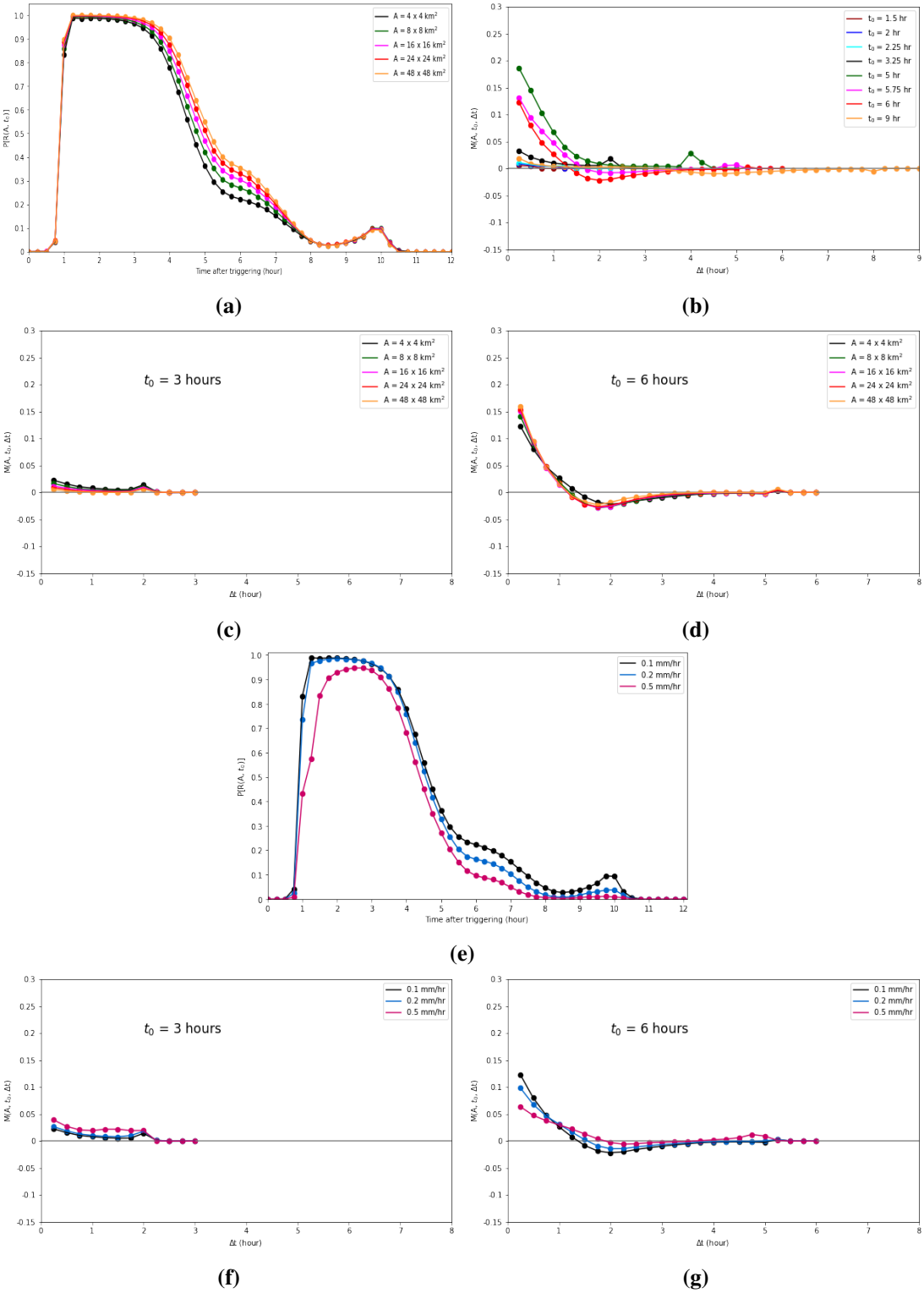

Figure 42: a. Probabilities of finding rain (P[R(A, t_0)]) for different areas A = 4x4 km^2, 8x8 km^2, 16x16 km^2, 24x24 km^2 and 48x48 km^2 in the UM CoMorph 4 km - Case 3 simulations. The time axis is shifted such that time equals zero corresponds to the time of triggering. b. Memory functions (**M**(A, t_0, Δt)) for A = 4x4 km^2 for different times t_0 = 1.5, 2, 2.25, 3.25, 5, 6, and 9 hours after triggering. Memory functions for different areas are shown for (c.) t_0 = 3 hours and (d.) 6 hours after triggering. e. Probabilities of finding rain (P[R(A, t_0)]) for A = 4x4 km^2 for different rain thresholds of 0.1, 0.2 and 0.5 mm hr^{-1} in the UM 6A simulations. Memory functions (**M**(A, t_0, Δt)) for A = 10x10 km^2 for different rain thresholds for (f.) t_0 = 3 and (g.) 6 hours after triggering.

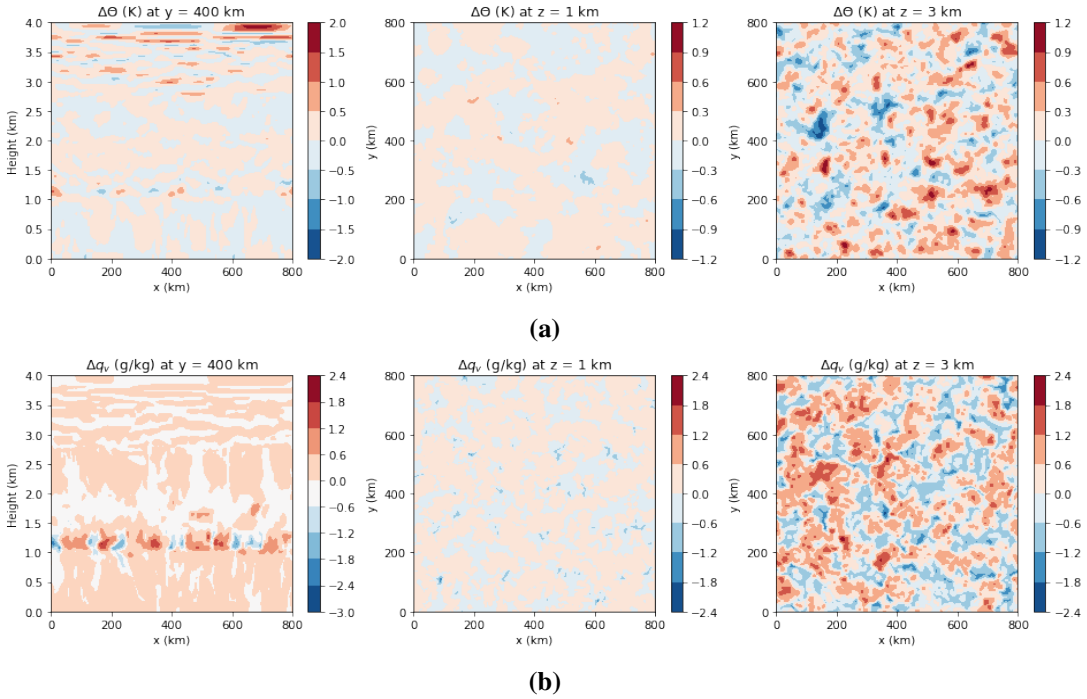

Figure 43: Same as in Figure 38 but for the CoMorph 4 km Case 2 simulation.

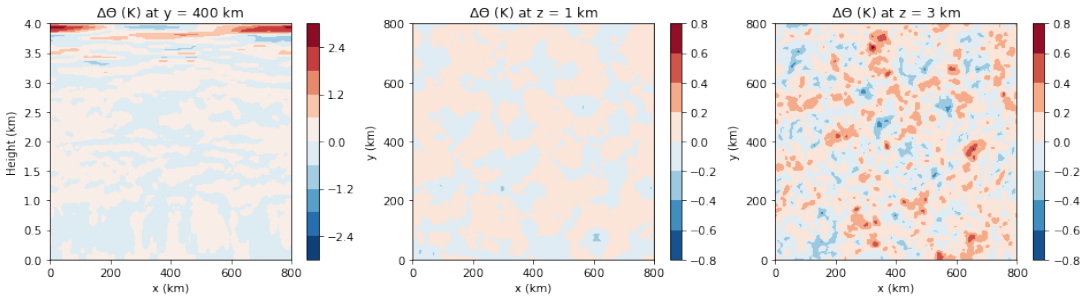

(a)

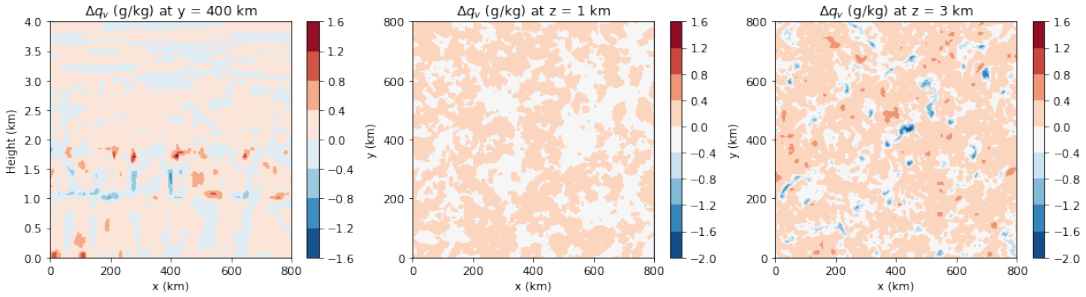

(b)

Figure 44: Same as in Figure 38 but for the CoMorph 4 km Case 3 simulation.